MODELLING OF TWO-PHASE FLOW WITH SURFACE ACTIVE PARTICLES

Der Fakultät Mathematik und Naturwissenschaften
der Technischen Universität Dresden

zur

Erlangung des akademischen Grades
Dr. rer. nat.
eingereichte

Dissertation

von

Dipl. Math. Sebastian Aland

geboren am
1. März 1983 in Lübben/Spreewald

Die Dissertation wurde in der Zeit von 01/2009 bis 05/2012
am Institut für wissenschaftliches Rechnen angefertigt.

Contents

Kurzfassung

Kolloidpartikel die von zwei nicht mischbaren Fluiden benetzt werden, tendieren dazu sich an der fluiden Grenzfläche aufzuhalten um die Oberflächenspannung zu minimieren. Bei genügender Anzahl solcher Kolloide werden diese zusammengedrückt und lassen die fluide Grenzfläche erstarren. Das gesamte System aus Fluiden und Kolloiden bildet dann eine spezielle Emulsion mit interessanten Eigenschaften. In dieser Arbeit wird ein kontinuum Model für solche Systeme entwickelt, basierend auf den Prinzipien der Massenerhaltung und der themodynamischen Konsistenz. Dabei wird die makroskopische Zwei-Phasen-Strömung durch eine Navier-Stokes Cahn-Hilliard Gleichung modelliert und die mikroskopischen Partikel an der fluiden Grenzfläche durch einen Phase-Field-Crystal Ansatz beschrieben. Zur Evaluation des verwendeten Strömungsmodells wird ein Test verschiedener Navier-Stokes Cahn-Hilliard Modelle anhand eines bekannten Benchmark Szenarios durchgeführt. Die Ergebnisse werden mit denen von anderen Methoden zur Simulation von Zwei-Phasen-Strömungen verglichen. Desweiteren wird eine neue Methode zur Simulation von Zwei-Phasen-Strömungen in komplexen Gebieten vorgestellt. Dabei wird die komplexe Geometrie implizit durch eine Phasenfeldvariable beschrieben, welche die charakteristische Funktion des Gebietes approximiert. Die Strömungsgleichungen werden dementsprechend so umformuliert, dass sie in einem größeren und einfacheren Gebiet gelten, wobei die Randbedingungen implizit durch zusätzliche Quellterme eingebracht werden. Zur Einarbeitung der Oberflächenkolloide in das Strömungsmodell wird schließlich die Variation der freien Energie des Gesamtsystems betrachtet. Dabei wird die Energie der Partikel durch die Phase-Field-Crystal Energie approximiert und die Energie der Oberfläche durch die Ginzburg-Landau Energie. Eine Variation der Gesamtenergie liefert dann die Phase-Field-Crystal Gleichung und die Navier-Stokes Cahn-Hilliard Gleichungen mit zusätzlichen elastischen Spannunngen. Zur Validierung des Ansatzes wird auch eine sharp interface Version der Gleichungen hergeleitet und mit der zuvor hergeleiteten diffuse interface Version abgeglichen. Die Diskretisierung der erhaltenen Gleichungen erfolgt durch Finiten Elemente in Kombination mit einem semi-impliziten Euler Verfahren. Durch numerische Simulationen wird die Anwendbarkeit des Modells gezeigt und bestätigt, dass die oberflächenaktiven Kolloide die fluide Grenzfläche hinreichend steif machen können um externen Kräften entgegenzuwirken und das gesamte System zu stabilisieren.

Abstract

Colloid particles that are partially wetted by two immiscible fluids can become confined to fluid-fluid interfaces. At sufficiently high volume fractions, the colloids may jam and the interface may crystallize. The fluids together with the interfacial colloids compose an emulsion with interesting new properties and offer an important route to new soft materials. Based on the principles of mass conservation and thermodynamic consistency, we develop a continuum model for such systems which combines a Cahn-Hilliard-Navier-Stokes model for the macroscopic two-phase fluid system with a surface Phase-Field-Crystal model for the microscopic colloidal particles along the interface. We begin with validating the used flow model by testing different diffuse interface models on a benchmark configuration for a two-dimensional rising bubble and compare the results with reference solutions obtained by other two-phase flow models. Furthermore, we present a new method for simulating two-phase flows in complex geometries, taking into account contact lines separating immiscible incompressible components. In this approach, the complex geometry is described implicitly by introducing a new phase-field variable, which is a smooth approximation of the characteristic function of the complex domain. The fluid and component concentration equations are reformulated and solved in larger regular domain with the boundary conditions being implicitly modeled using source terms. Finally, we derive the thermodynamically consistent diffuse interface model for two-phase flow with interfacial particles by taking into account the surface energy and the energy associated with surface colloids from the surface PFC model. The resulting governing equations are the phase field crystal equations and Navier-Stokes Cahn-Hilliard equations with an additional elastic stress. To validate our approach, we derive a sharp interface model and show agreement with the diffuse interface model. We demonstrate the feasibility of the model and present numerical simulations that confirm the ability of the colloids to make the interface sufficiently rigid to resist external forces and to stabilize interfaces for long times.

Chapter 1

Introduction

1.1 Objectives and motivation

Particle-stabilized emulsions are widely used in many fields of our daily life such as the food, cosmetic and pharmaceutical industries. They are used to deliver drug compounds, fragrances or flavours. An emulsion is a mixture of two or more liquids that are normally immiscible. The segregation of the fluid phases is prevented by an additional emulsifier which, in case of particle-stabilized emulsions, is typically a layer of colloid particles adsorbed at the fluid-fluid interface. This leads to a complicated system of fluids and interfacial solids, accounting for viscous, inertial and elastic interactions. To gain further insight into the mechanical properties of these particle-stabilized emulsions is the motivation behind this work.

Morphologically, one can distinguish between two different kinds of particle-stabilized emulsions: Pickering emulsions and so-called 'bijels' (bicontinuous interfacially jammed emulsion gels). In Pickering emulsions [Pic07] small droplets of one fluid (the dispersed phase) are dispersed in a surrounding fluid (the continuous phase), see e.g. Fig. 1.1. Bijels on the other hand consist of interpenetrating, continuous domains of two immiscible fluids. Both, bijels and Pickering emulsions, are stabilized by a jammed layer of colloidal particles at the fluid-fluid interface. Stability in the context of emulsions means that the particle layer counteracts the surface tension and thus prevents the fluid structure from coarsening. From a modelling point of view Pickering emulsions and bijels can be treated similarly, and in fact, the ideas we develop in this thesis are applicable for both systems. However, due to their practical relevance and their more interesting mechanical

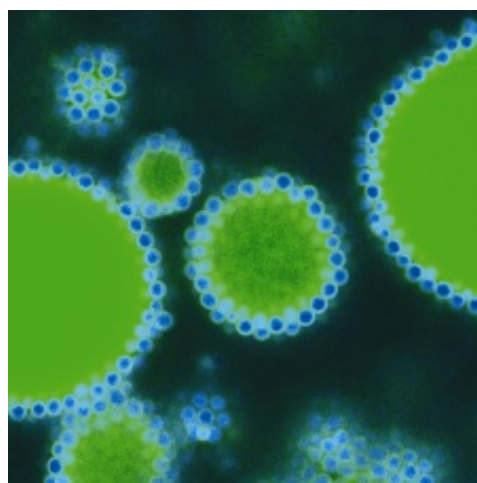**Figure 1.1:** An oil in water emulsion stabilized by particles through the Pickering effect. Multi-wavelength confocal microscopy allows identification of the microstructure. In this case the particles (blue) stabilize the interface of oil droplets (green) in water. Credit: Dr Job Thijssen*.

*from *http://www.ph.ed.ac.uk/industry/expertise/edinburgh-complex-fluid-partnership/formulation/emulsification*
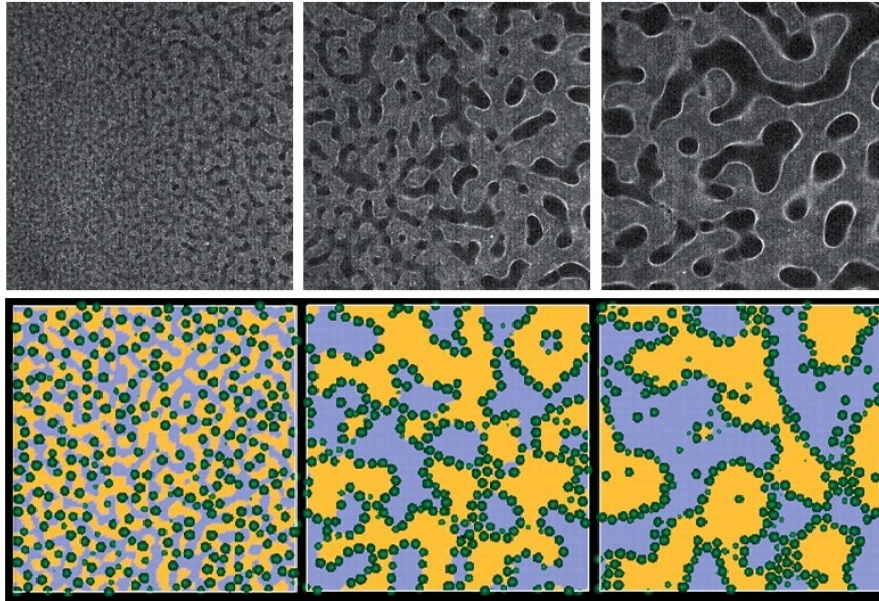
Figure 1.2: The separation via spinodal decomposition of two immiscible liquids with colloidal particles. **Top:** Time series of fluorescence confocal microscopy images from [HWS$^+$07]. Particles appear white, whereas liquids appear dark **Bottom:** Lattice-Boltzmann simulation from [SAP$^+$05]. The two fluids are colored yellow and blue, colloidal particles are green.

properties we will focus on bijels in the following.

Bijels were initially proposed on the basis of computer simulations [SAP$^+$05] and have subsequently been confirmed experimentally [HWS$^+$07]. For a review on both theoretical and experimental approaches we refer the reader to [CC08]. The basic ideas behind the formation of bijels are: (i) generation of a bicontinuous structure by spinodal decomposition or intense mixing; (ii) adsorption of colloidal particles at interfaces; (iii) jamming of interface colloids either by a reduction in surface area of interfaces or by sufficiently high volume fractions of interfacial colloids. If the layer of colloidal particles at the interface truly solidifies a three-dimensional solid gel with finite elastic modulus and yield stress is formed. Such an amorphous structure with fluid bicontinuity and yield stress forms a novel class of materials. However, the stability of these materials is still under debate. It is not known whether the system is stable for long-times, and what the mechanisms that ensure stability are. For example, it remains an open question whether attraction between the colloids is essential for stability, or if repulsive particle interactions can lead to stable configurations as well.

1.2   State of the art

Using computer simulations to understand the dynamic properties of bijels is a promising approach. As mentioned above, bijels were first discovered using numerical simulations by Stratford et al.[SAP$^+$05] for equal volume fractions of the two fluid components, see Fig. 1.2. Later simulations were performed by Kim et al. [KSAC08] to determine the effect of varying volume fraction. These authors used a lattice Boltzmann method (LBM) with colloids undergoing Brownian motion. The wide range of spatiotemporal scales makes this problem very difficult to solve. The spatial scales that need to be resolved range from the inter-colloid forces in the jammed layer on the interface to the mesoscopic bicontinuous domain structures that characterize the bijel. The time scales range from those associated

with the Brownian motion of the colloids to the macroscopic arrest of the structure, which can last up to several months [HWS$^+$07]. In the LBM, resolving this range of time scales is particularly problematic since the simulation time is limited by the Brownian diffusion time making it difficult to perform long-time simulations.

Despite of these limitations, the Lattice Boltzmann method is currently state of the art in simulating bijels and is used by most authors dealing with this topic [Lad94a, Lad94b, LV01, JS09, JH11]. Another approach based on Dissipative Particle Dynamics (DPD) was used in [HL07] where the authors confirmed the results of Stratford et al. and predicted that bijels are thermodynamically metastable with smaller colloids being more easily desorbed which destabilizes the structure. In the DPD approach, colloids are modeled by arranging DPD particles on a sphere and connecting them by rigid bonds taking care that fluid particles cannot penetrate. This limits the size of the colloids and the range of spatial scales that can be simulated. Alternatively, the Navier-Stokes equations can be used to describe the fluids on the large time scales of interest for investigations on stability. However, inclusion of colloidal particles into such an approach leads to limitations on the size of the system. A first attempt in this direction is given in [MW11]. The approach involves a diffuse-interface description of the fluid phases, in addition to a collection of solid particles. However, this approach requires the resolution of the short particle-particle interaction time scales.

1.3   Overview of this thesis

In this thesis, we develop an alternative modeling approach, which combines the atomistic processes along the interface with the continuum processes in the bulk phases, that has the potential to simulate large domains for long times. In particular, we develop a continuum model that combines diffuse-interface (phase-field) modeling for multiphase flow (see Sec. 2.6.2) with an adapted phase field crystal (PFC) model (see Sec. 2.7) to study colloid jamming at interfaces. We start in Sec. 2 by giving an overview of tools and methods that will be used. In particular we introduce the phase field method, the diffuse interface model for two-phase flows, the PFC model and methods for bulk-surface coupling. We next assess the accuracy of diffuse interface models for two phase flows in Sec. 3. In particular we present the very recent results of the author's paper [AV11], where the first benchmark study of different diffuse interface models is conducted and results are compared with those of other well-established numerical methods. Then, in Sec. 4 we derive a new diffuse domain version of the Navier-Stokes Cahn-Hilliard equations, which make it easy to solve two-phase flow problems in arbitrary, moving domains. This will be used later to simulate the interaction of a bijel with a rigid body. Note, that the content of Sec. 4 has also been published by the author in [ALV10]. Finally, in Sec. 5 we arrive at the core part of this thesis, the simulation of particle-stabilized emulsions. Following three of the author's papers [ALV11, ALV12, AV12] we develop a continuum model using the preparatory work of the previous sections. In particular, a surface PFC model that accounts for the interactions of the colloid particles with the bulk fluids is developed. Additionally, a model for attachment of colloids to the interface is derived, and a concentration equation for a colloidal density in one fluid phase is used with attachment/detachment boundary conditions along the fluid-fluid interface. These surface and bulk equations are reformulated using the diffuse interface and diffuse domain approaches introduced

in Refs.[RV06, LLRV09, TLL$^+$09] for solving partial differential equations on surfaces and complex domains and coupling surface and bulk problems. The governing equations, and extra stresses, are derived using an energy variation approach accounting for surface energy, modeled by a Cahn-Hilliard-type energy[CH58], and the energy associated with surface colloids from the surface PFC model.

Chapter 2

Mathematical Background

2.1 Variational derivatives and gradient flow

In this thesis we make use of the concept of variational (or functional) derivatives, which is part of to the calculus of variations. This field is used in mathematical physics and deals with the extrema of functionals. To characterize an extremum it is, like in finite dimensional calculus, necessary to define a derivative. We will give a short introduction on the calculation of variational derivatives. A more detailed overview can be found in [Cow05].

We consider a Hilbert-space H with the L^2 inner product and a mapping $E : H \to \mathbb{R}$. Let us start with well-known case when H is finite-dimensional. Then, the derivative of E at some $v \in H$ in direction $h \in H$ is defined by:

$$\frac{dE[v]}{dv}(h) := \lim_{\epsilon \to 0} \frac{1}{\epsilon} \left(E[v + \epsilon h] - E[v] \right),$$

if this limit exists. Note, that $\frac{dE[v]}{dv}(\cdot)$ is a mapping which is linear in its argument, and therefore $\frac{dE[v]}{dv}$ is an element of the dual space H^*. Consequently, the directional derivative can be expressed as a scalar product

$$\frac{dE[v]}{dv}(h) = \left(\frac{dE[v]}{dv}, h \right) \qquad \forall h \in H$$

where $\frac{dE[v]}{dv}$ is a vector in H and is called the gradient of E. Next, let us consider the infinite-dimensional setting where H is a space of functions and consequently E is a functional. In the scope of this thesis we consider physical energy functionals and will often refer to E as an energy. Analogously

to the above we define the directional derivative

$$\frac{\delta E[v]}{\delta v}(h) := \lim_{\epsilon \to 0} \frac{1}{\epsilon} \left(E[v + \epsilon h] - E[v] \right)$$

$$= \frac{d}{d\epsilon} E[v + \epsilon h]_{|\epsilon=0}$$

Again $\frac{\delta E[v]}{\delta v}(h)$ is a mapping linear in h. Using Riesz' representation theorem we can also express $\frac{\delta E[v]}{\delta v} \in H^*$ by a function $u \in H$ related to $\frac{\delta E[v]}{\delta v}$ by

$$(u, h) = \frac{\delta E[v]}{\delta v}(h) \qquad\qquad \forall h \in H$$

where $(\cdot, \cdot)$ is the L^2 inner product in H. Like in the finite-dimensional case, u is called the gradient of E with respect to v. Note that, if H admits different inner products, the choice of the inner product influences the representation of u. In this thesis, we will only consider the L^2 inner product, and therefore we will equivalently write $\frac{\delta E[v]}{\delta v}$ instead of u, and call this the variational derivative.

A very common special case is when v is a physical quantity which may depend on time. Then, one can use the functional time derivative, here denoted by an overdot, to calculate $\frac{\delta E[v]}{\delta v}$. It holds

$$\dot{E}[v(t)] = \lim_{\epsilon \to 0} \frac{1}{\epsilon} \left(E[v(t + \epsilon)] - E[v(t)] \right)$$

$$= \lim_{\epsilon \to 0} \frac{1}{\epsilon} \left(E[v(t) + \epsilon \dot{v} + \mathcal{O}(\epsilon^2)] - E[v(t)] \right)$$

$$= \lim_{\epsilon \to 0} \frac{1}{\epsilon} \left(E[v(t) + \epsilon \dot{v}] - E[v(t)] \right)$$

$$= \left(\frac{\delta E[v]}{\delta v}, \dot{v} \right). \tag{2.1}$$

Consequently, to calculate the variational derivative of E it is sufficient to calculate its time derivative in form of an inner product of $\dot{v}$, for arbitrary $\dot{v}$.

From Eq. (2.1) one can immediately conclude energy minimizing time evolutions of v. For example, $\dot{E} \leq 0$ can be assured by taking $\dot{v} = -\frac{\delta E[v]}{\delta v}$, which is also known as L^2 gradient flow or by taking $\dot{v} = \Delta \frac{\delta E[v]}{\delta v}$, the so-called H^{-1} gradient flow.

2.2 Phase fields and surface energy

In this thesis we consider problems involving moving (or free) boundaries. Here, the boundary is given by the interface between two different fluids. The first question when modelling such problems is how to mathematically represent the interface and the bulk regions, respectively. In the literature, there is a variety of different methods available. When simple geometries are involved, the interface may be represented by a simple structure like the graph of a function. For more complex settings the interface can be tracked by marker particles, which is still very efficient and fast. However topological changes of the interface are difficult to handle, particularly in 3D. To deal with such changes, so-called interface capturing methods are advantageous. The most important interface capturing methods are

- tracking of the bulk characteristic function by a volume of fluid (VOF) method

- the level-set method, where a level-set of an indicator function defines the interface

- the phase field method.

In this thesis we choose the phase field method which features facile implementation and the possibility to easily incorporate additional surface or bulk equations.

A phase field is an auxiliary function (or field) to model interfacial problems. It takes distinct values in each of the fluid phases (e.g. 0 and 1) with a smooth transition in between around the interface. Hence, the interface is diffuse having a finite width and an intermediate level set of the phase field (e.g. 0.5) may be used to get a discrete interface location. Phase field methods were originally developed to describe solid-liquid phase transitions and have since seen an enormous growth in use, see [Emm08] for a review. Fig. 2.1 shows an example of a phase field.
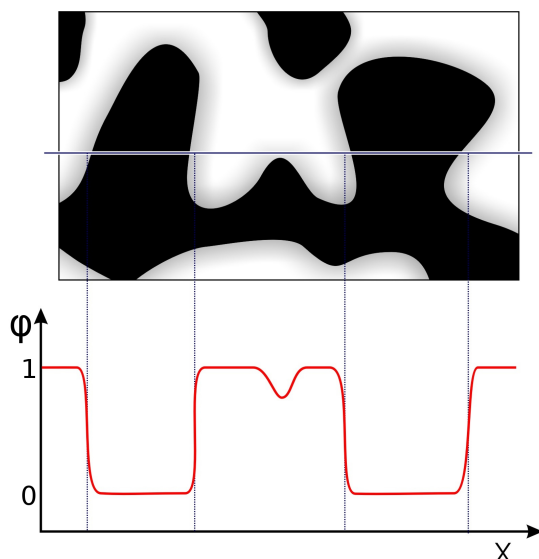
Figure 2.1: Schematic of a phase field from www.wikipedia.org. Top: phase field colored black at $\varphi = 0$ and white at $\varphi = 1$, Bottom: Cut through the phase field showing the smooth but rapid transitions.

Phase fields can be constructed by physical arguments if one has an expression for the free energy of the system. A typical choice for the energy associated to a fluid-fluid interface is the Ginzburg-Landau energy given by:

$$E_\sigma = \int_\Omega \frac{1}{\epsilon} B(\psi) + \frac{\epsilon}{2} |\nabla \psi|^2. \tag{2.2}$$

Here Ω is the domain under consideration, ψ is the phase field, ϵ the interface thickness and B a double-well potential having local minima in those values of ψ which represent the bulk phases. If ψ is either 0 or 1 in the two bulk phases, one may take $B(\psi) = \psi^2(1 - \psi)^2$ for example. The double-well potential B is also called the bulk free energy and penalizes any mixing of the phases, while the second term in (2.2) accounts for the fact that gradients in the concentration field ψ are energetically unfavorable. Note that in the following we will also refer to E_σ as surface energy or Cahn-Hilliard energy.

Minimizing (2.2) requires the variational derivative of E_σ to vanish:

$$\frac{\delta E_\sigma}{\delta \psi} = \frac{1}{\epsilon} \frac{\partial B(\psi)}{\partial \psi} - \epsilon \Delta \psi = 0. \tag{2.3}$$

An equilibrium state is reached when Eq. (2.3) is satisfied. To get a better insight of how ψ looks in this case we will consider a simple 1D example: a single phase transition in $x = 0$ on the domain $\mathbb{R}$. Let us assume the boundary conditions

$$\psi(-\infty) = 0, \quad \psi(0) = 0.5, \quad \psi(\infty) = 1 \tag{2.4}$$

and that the double-well potential is given by $B = k\psi^2(1 - \psi)^2$ with a constant k. A solution to (2.3) can be obtained by multiplying Eq. (2.3) with ψ' and integrating from $-\infty$ to x. We obtain

$$\int_{-\infty}^{x} \frac{1}{\epsilon} \frac{\partial B(\psi)}{\partial \psi} \psi' \, dx = \int_{-\infty}^{x} \epsilon \psi'' \psi' \, dx \tag{2.5}$$

which is equivalent to

$$\int_{-\infty}^{x} \frac{1}{\epsilon} (B(\psi))' \, dx = \int_{-\infty}^{x} \frac{\epsilon}{2} ((\psi')^2)' \, dx \tag{2.6}$$

Using that $B(\psi(-\infty)) = 0$ and assuming that $\psi'(-\infty) = 0$ yields

$$\frac{1}{\epsilon} B(\psi) = \frac{\epsilon}{2} (\psi')^2. \tag{2.7}$$

This equation is also known as equipartition of energy, since it means that in the equilibrium state both terms in the surface energy E_σ give equal contributions. Eq. (2.7) can also be written as ordinary differential equation,

$$\psi' = \frac{\sqrt{2B(\psi)}}{\epsilon} = \frac{\sqrt{2k}}{\epsilon} \psi(1 - \psi) \tag{2.8}$$

whose solution with respect to (2.4) is

$$\psi_0 = \frac{1}{2} + \frac{1}{2} \tanh\left(\frac{\sqrt{k/2}}{\epsilon} x \right) \tag{2.9}$$

Such a hyperbolic tangent profile is typical for phase fields. The interface region can be defined as a narrow band around the discrete interface location, e.g. where $\psi \in [0.05, 0.95]$. From Eq. (2.9) on can see that the thickness of this interface region is proportional to ϵ. Also in higher dimensions the equilibrium shape of the phase field has the same structure as given in Eq. (2.9) with x replaced by the signed distance to the interface [EGK08].

Next, we are interested in the correct scaling of the surface energy in the equilibrium. Using (2.7) we calculate the energy associated with a single phase transition in 1D and denote it with k_σ

$$k_\sigma = E_\sigma[\psi_0] = \int_{-\infty}^{\infty} \epsilon|\nabla\psi|^2 dx \tag{2.10}$$

$$= \int_0^1 \epsilon|\psi'|d\psi \tag{2.11}$$

$$= \int_0^1 \sqrt{2B(\psi)}d\psi \tag{2.12}$$

$$= \frac{\sqrt{k}}{3\sqrt{2}} \tag{2.13}$$

Note, that this scaling only depends on the chosen double well B. In particular k_σ is independent of ϵ and when ϵ tends to zero, the corresponding equilibrium surface energy density becomes more and more confined to the interface and consequently approximates $k_\sigma\delta_\Gamma$, where δ_Γ is the Dirac surface delta function. To be more precise, we conclude the following approximations from (2.13) and (2.7):

- $\frac{1}{\epsilon}B(\psi) + \frac{\epsilon}{2}|\nabla\psi|^2 \xrightarrow{\epsilon\to 0} k_\sigma\delta_\Gamma$ (2.14)

- $|\nabla\psi|^2 \xrightarrow{\epsilon\to 0} \frac{1}{\epsilon}k_\sigma\delta_\Gamma$ (2.15)

- $B(\psi) \xrightarrow{\epsilon\to 0} \frac{\epsilon}{2}k_\sigma\delta_\Gamma$ (2.16)

Note, that these approximations are also valid in 2D and 3D, which can be shown using matched asymptotic expansion (see e.g. [Peg89], [EGK08]). Another common case is to represent the bulk phases by $\psi \approx -1$ and $\psi \approx +1$ using the bulk free energy $B = k(1-\psi^2)^2$. In this case the hyperbolic tangent profile of ψ is given by $\psi_0 = \tanh\left(\frac{\sqrt{2k}}{\epsilon}x\right)$ which yields the scaling factor $k_\sigma = \frac{4\sqrt{2k}}{3}$.

2.3 Analysis on surfaces

Let Γ denote the evolving surface, which we model mathematically as a smooth oriented hyper-surface in $\mathbb{R}^{d+1}$. We further assume that Γ is embedded in a domain $\Omega \subseteq \mathbb{R}^{d+1}$, where the set Ω will be the domain on which we define our equations. The surface normal $\mathbf{n}(x)$ to Γ in $x \in \Gamma$ is given through a differentiable function $\mathbf{n}$ defined in a neighborhood of Γ. The mean curvature κ of the surface is defined by

$$\kappa(x) = \sum_{i=1}^{d} \kappa_i(x), \tag{2.17}$$

where κ_i denotes the i-th principle curvature of Γ. If the surface normal is known, κ may be calculated by

$$\kappa = \nabla \cdot \mathbf{n}|_\Gamma, \tag{2.18}$$

see e.g. [DDE05]. Note, that here κ is positive when $\mathbf{n}$ is the outer normal to a spherical surface.

2.3.1 Surface operators and partial integration

For a differentiable function u defined in a neighborhood of Γ, the surface gradient of u is given through

$$\nabla_\Gamma u = P_\Gamma \nabla u, \tag{2.19}$$

where $P_\Gamma = I - \mathbf{n} \otimes \mathbf{n}$ is the orthogonal projection of a vector in $\mathbb{R}^{d+1}$ onto the tangent plane to Γ. For a differentiable vector field $\mathbf{u}$ the surface divergence is given by

$$\nabla_\Gamma \cdot \mathbf{u} = P_\Gamma : \nabla \mathbf{u} = \sum_{i=1}^{d+1} \sum_{j=1}^{d+1} P_{ij} \frac{\partial \mathbf{u}_i}{\partial x_j}. \tag{2.20}$$

Assuming that the normal vector is extended constant in the normal direction, $\mathbf{n} \cdot \nabla \mathbf{n} = 0$, and using that $\nabla \mathbf{n} \cdot \mathbf{n} = \frac{1}{2} \nabla (\mathbf{n} \cdot \mathbf{n}) = 0$ yields the useful identities

$$\nabla_\Gamma \cdot \mathbf{u} = \nabla \cdot \mathbf{u} - \mathbf{n} \cdot \nabla \mathbf{u} \cdot \mathbf{n} \tag{2.21}$$
$$= \nabla \cdot (P\mathbf{u}) + \kappa \mathbf{u} \cdot \mathbf{n} \tag{2.22}$$

The surface Laplacian is then defined by

$$\Delta_\Gamma u = \nabla_\Gamma \cdot \nabla_\Gamma u. \tag{2.23}$$

Furthermore, we will use Green's formula for integration by parts on surfaces

$$\int_\Gamma \nabla_\Gamma \cdot \mathbf{u} \eta dA = \int_{\partial \Gamma} \mathbf{u} \cdot m_\Gamma \eta ds - \int_\Gamma \nabla_\Gamma \eta \cdot \mathbf{u} dA, \tag{2.24}$$

where m_Γ is the outward normal to $\partial \Gamma$. If Γ is a surface without boundary, $\partial \Gamma = \emptyset$, or $\eta_{|\partial\Gamma} = 0$ this simplifies to

$$\int_\Gamma \nabla_\Gamma \cdot \mathbf{u} \eta dA = - \int_\Gamma \nabla_\Gamma \eta \cdot \mathbf{u} dA, \tag{2.25}$$

For a differentiable vector field X on Ω, the formula for integration by parts reads

$$\int_\Omega \nabla \cdot X \eta dx = \int_{\partial \Omega} X \cdot m_\Omega \eta dA - \int_\Omega \nabla \eta \cdot X dx, \tag{2.26}$$

with m_Ω being the outward normal to $\partial \Omega$. If $\eta \in C_0^\infty(\Omega)$ or $X \cdot m_\Omega = 0$ this simplifies to

$$\int_\Omega \nabla \cdot X \eta dx = - \int_\Omega \nabla \eta \cdot X dx. \tag{2.27}$$

2.3.2 Phase field approximations

When a phase field is used to represent the interface as discussed in Sec. 2.2 the surface normal, directed to the fluid with the higher value of ψ, can be written as

$$\tilde{\mathbf{n}} = \frac{\nabla \psi}{|\nabla \psi|}. \tag{2.28}$$

Consequently, a phase field approximation of the mean curvature is given by

$$\tilde{\kappa} = \nabla \cdot \frac{\nabla \psi}{|\nabla \psi|}, \tag{2.29}$$

Here, $\tilde{\kappa}$ is positive for a sphere of the fluid with the lower value of ψ. However, in phase field methods it is more common to use the following relation for the curvature

$$\left(\frac{1}{\epsilon} B'(\psi) - \epsilon \Delta \psi \right) \nabla \psi \xrightarrow{\epsilon \to 0} - k_\sigma \kappa \delta_\Gamma \mathbf{n}, \tag{2.30}$$

where the scaling factor k_σ defined in Sec. 2.2 depends on the chosen double well potential. Furthermore, the surface gradient in a phase field context is given by

$$\tilde{\nabla}_\Gamma u = \tilde{P}_\Gamma \nabla u = \left(I - \frac{\nabla \psi}{|\nabla \psi|} \otimes \frac{\nabla \psi}{|\nabla \psi|} \right) \nabla u, \tag{2.31}$$

and the surface divergence can be written as

$$\tilde{\nabla}_\Gamma \cdot \mathbf{u} = \frac{1}{\tilde{\delta}_\Gamma} \nabla \cdot \left(\tilde{\delta}_\Gamma \mathbf{u} \right), \tag{2.32}$$

where $\tilde{\delta}_\Gamma$ denotes a diffuse interface approximation of the surface delta function δ_Γ, e.g. one of the approximations given in Eqs. (2.14)-(2.16). It follows that the surface Laplacian can be expressed as [ALM+12]

$$\tilde{\Delta}_\Gamma u = \frac{1}{\tilde{\delta}_\Gamma} \nabla \cdot \left(\tilde{\delta}_\Gamma \tilde{P}_\Gamma \nabla u \right). \tag{2.33}$$

Note that the projection $\tilde{P}_\Gamma$ in Eq. (2.33) can be dropped if one can assume u to be constant in the normal direction. With the above definitions and after dropping all boundary terms, the integration by parts on a diffuse interface admits the form:

$$\int_\Omega \tilde{\delta}_\Gamma \tilde{\Delta}_\Gamma u \, \eta \, dx = - \int_\Omega \tilde{\delta}_\Gamma \tilde{\nabla}_\Gamma u \cdot \tilde{\nabla}_\Gamma \eta \, dx = \int_\Omega \tilde{\delta}_\Gamma u \, \tilde{\Delta}_\Gamma \eta \, dx, \tag{2.34}$$

which agrees well with the sharp interface analogue (compare Eq. 2.25):

$$\int_\Gamma \Delta_\Gamma u\, \eta\, dA = -\int_\Gamma \nabla_\Gamma u \cdot \nabla_\Gamma \eta\, dA = \int_\Gamma u\, \Delta_\Gamma \eta\, dA. \tag{2.35}$$

2.4 Bulk-Surface concentration equations

We consider the evolution of a microscopic quantity (e.g. particles or a chemical species) in a given geometry, which may be a bulk region or a surface. Let us denote by C the concentration of this quantity in the bulk region Ω, whereas c denotes its concentration on the surface Γ. Based on the principle of mass conservation one can derive evolution equations for c and C, respectively. Next, we provide a derivation for the surface evolution of c.

2.4.1 Conservative surface evolution

First, let us assume that the surface quantity $c(x), x \in \Gamma$ is transported due to convection (with a prescribed velocity $\mathbf{u}$) and diffusion. Furthermore, we define a control volume γ to be a connected bounded subset of Γ which also moves with velocity $\mathbf{u}$. The conservation of mass property yields

$$\frac{d}{dt}\int_{\gamma(t)} c\, dA = -\int_{\partial\gamma(t)} q \cdot m\, ds + \int_{\gamma(t)} j\, dA, \tag{2.36}$$

with j being the flux from the bulk to the surface, q the flux along Γ through $\partial\gamma$ and m the unit normal to $\partial\gamma(t)$ lying in a tangent plane and pointing out of $\gamma(t)$. The LHS of Eq. (2.36) can be treated with a variant of Reynolds' transport theorem given by

$$\frac{d}{dt}\int_{\gamma(t)} c\, dA = \int_{\gamma(t)} \dot{c} + c\nabla_\Gamma \cdot \mathbf{u}\, dA, \tag{2.37}$$

where the overdot denotes the material derivative $\partial_t + \mathbf{u} \cdot \nabla$. For the second term of Eq. (2.36) we restrict ourselves to the case of a diffusive flux, $q := -D_f \nabla_\Gamma c$ with constant diffusion coefficient D_f and use Eq. (2.24) to obtain

$$-\int_{\partial\gamma(t)} q \cdot m\, ds = \int_{\gamma(t)} D_f \Delta_\Gamma c\, dA. \tag{2.38}$$

Inserting Eqs.(2.37) and (2.38) into Eq.(2.36) and requiring that all equations hold for arbitrary control volumes gives the surface transport equation

$$\dot{c} + c\nabla_\Gamma \cdot \mathbf{u} = D_f \Delta_\Gamma c + j \qquad\qquad \text{on } \Gamma. \tag{2.39}$$

Using the definition of the material derivative Eq. (2.39) can be written as

$$\partial_t c + \mathbf{u} \cdot \nabla c + c\nabla_\Gamma \cdot \mathbf{u} = D_f \Delta_\Gamma c + j \qquad\qquad \text{on } \Gamma, \tag{2.40}$$

which requires that c is smoothly extended in a small neighborhood of Γ to be well-defined. Eq. (2.40) is equivalent to

$$\partial_t c + \nabla_\Gamma \cdot (\mathbf{u}c) + V\mathbf{n} \cdot \nabla c = D_f \Delta_\Gamma c + j \qquad \text{on } \Gamma, \qquad (2.41)$$

where $V = \mathbf{u} \cdot n$ is the normal velocity. In many practical cases one can assume c to be constant in the normal direction which allows the simplifications

$$\partial_t c + \nabla_\Gamma \cdot (\mathbf{u}c) = D_f \Delta_\Gamma c + j \qquad \text{on } \Gamma, \qquad (2.42)$$

or

$$\partial_t c + \nabla_\Gamma \cdot (P\mathbf{u}c) + cV\kappa = D_f \Delta_\Gamma c + j \qquad \text{on } \Gamma. \qquad (2.43)$$

2.4.2 Classical bulk-surface coupling

A bulk evolution equation for C can be derived analogously to the derivation of the surface evolution equation for c. Putting both together, we get the classical coupled bulk-surface equations:

$$\partial_t C + \nabla \cdot (\mathbf{u}C) = D_F \Delta C \qquad \text{on } \Omega \qquad (2.44)$$

$$\mathbf{n} \cdot \nabla C = j \qquad \text{on } \Gamma \qquad (2.45)$$

$$\partial_t c + \mathbf{u} \cdot \nabla c + c\nabla_\Gamma \cdot \mathbf{u} = D_f \Delta_\Gamma c + j \qquad \text{on } \Gamma \qquad (2.46)$$

where D_F is a diffusion coefficient. It remains to define the flux j which is done in the next section.

2.4.3 Adsorption kinetics

Adsorption is the adhesion of atoms or molecules of a surrounding fluid to a solid or liquid surface. In general, adsorption may be driven by weak van der Waals forces (physisorption), covalent bonding (chemisorption) or electrostatic attraction. Here, we will only consider physisorption which is the most common case. Fig. 2.2 shows a schematic. Physisorption is usually described through isotherms, that is, the equilibrium relation of molecules in the fluid phase above the surface and the corresponding adsorbed molecules which are bound to the surface at constant temperature.

The simplest isotherm, also known as Henry's law, assumes that the surface concentration of the solute is proportional to its bulk concentration above the surface (the partial pressure, if the bulk phase is a gas). This relation can be expressed by $c = HC$, where H is the so-called Henry constant. The applicability of Henry's law is very limited, in particular it is only suitable for very low surface concentrations.

A better model is due to Langmuir who was the first to develop an adsorption isotherm based on physical arguments. The model is very popular, and we will briefly address the main ideas here. Langmuir makes the following four assumptions:

1. The surface of the adsorbent is uniform, which makes all the adsorption sites equivalent.
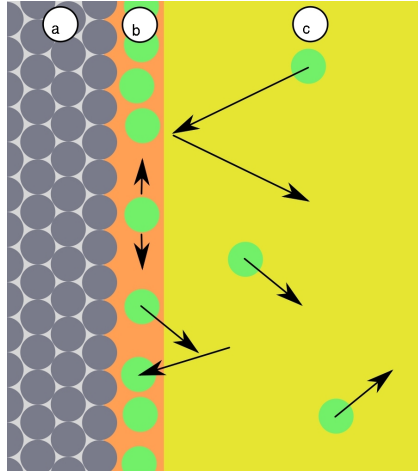
Figure 2.2: The process of physisorption. (a) adsorbent, (b) adsorbate, (c) fluid phase. Image from *www.wikipedia.org*.

2. There is no interaction between adsorbed molecules.

3. All adsorption occurs through the same mechanism.

4. The adsorbed molecules form only a monolayer

Based on these and using statistical physics it is relatively easy to get to the Langmuir kinetic equation for a stationary interface:

$$\partial_t c = j, \tag{2.47}$$
$$j := k_a C(1 - c/c^\infty) - k_d c \tag{2.48}$$

where the constants k_a and k_d define the adsorption and desorption speed, respectively and the saturation constant c^∞ defines the maximum interface concentration.

Langmuir was mainly looking at the equilibrium state of surface concentration, that is, when $\partial_t c = 0$. In this case attachment and detachment balance each other out and one gets Langmuir's isotherm

$$c = c^\infty \frac{C}{k + C} \qquad\qquad \text{with } k = \frac{c^\infty k_d}{k_a} \tag{2.49}$$

In reality Langmuir's assumptions are seldom all true. In particular, the fourth condition is often not fulfilled as frequently more molecules will adsorb to the monolayer. However, despite its limitations, Langmuir's isotherm is often the first choice for many practical applications.

2.4.4 Surfactant dependent surface tension

In general, interfacial particles change the properties of the interface and can have an impact on the fluid dynamics of the system. The most important effect of this kind is the change of surface tension caused by surfactant particles. In this section we will briefly develop a relation between surfactant concentration and surface tension following the ideas of Langmuir.
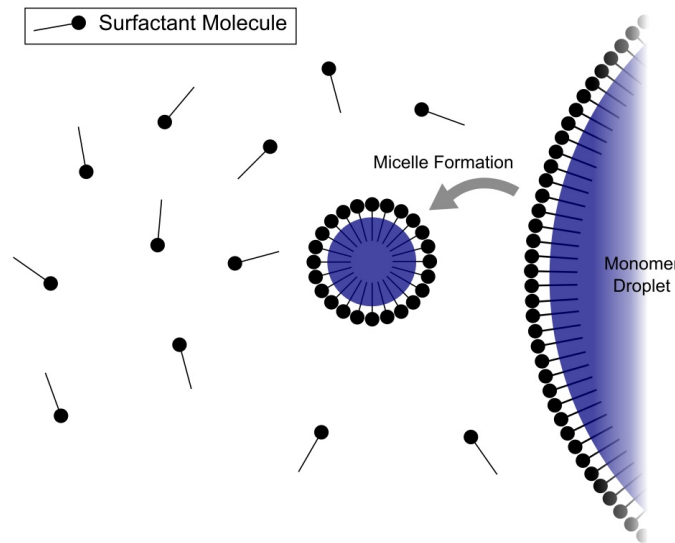
Figure 2.3: Schematic of an oil droplet in water completely covered with surfactant particles with hydrophilic head and hydrophobic tail. Remaining surfactant particles can form micelles. Based on an image from *www.wikipedia.org*.

Let us denote the interfacial and bulk surfactant concentration by c and C, respectively and the surface tension by σ. A relation between C and σ is given by Gibbs adsorption equation, also known as Gibbs isotherm. Assuming constant temperature and $c >> C$, which holds for most surfactants, Gibbs isotherm is given by

$$\frac{d\sigma}{d\ln C} = -RTc \tag{2.50}$$

with gas constant R and temperature T. Using $d\ln C = C^{-1}dC$ and Eq. (2.49) yields

$$\frac{d\sigma}{dC} = -\frac{RTc^\infty}{k + C}. \tag{2.51}$$

Denoting the surface tension of a clean surface ($C = 0$) by σ_0, the solution of this differential equation can be calculated as

$$\sigma = \sigma_0 - RTc^\infty \ln(1 + C/k) \tag{2.52}$$
$$= \sigma_0 + RTc^\infty \ln(1 - c/c^\infty) \tag{2.53}$$

which is the Langmuir model of surfactant-dependent surface tension. This model is widely used in the literature. To incorporate additional physics, the model can be generalized, e.g. to the Frumkin isotherm

$$\sigma = \sigma_0 + RTc^\infty \ln(1 - c/c^\infty) - \alpha(c/c^\infty)^2 \tag{2.54}$$

where α is a measure for repulsive or attractive interactions between adsorbed surfactant particles.

The models (2.53) and (2.54) lead to decrease in surface tension when the surfactant concentration increases. For high surfactant concentrations the equations may even result in an non-physical negative surface tension. In reality the decrease in surface tension significantly slows down when the surfactant concentration reaches a certain limit. This limit of concentration is called the critical micelle concentration (CMC), since at this point the surfactant molecules start to form aggregates, so-called micelles. From a modelling point of view it is reasonable to use Eqs. (2.53) and (2.54) only below the CMC and to keep a fixed surface tension above the CMC, e.g. by replacing c by $\min(c, CMC)$.

2.5 PDEs in complex geometries

Complex geometries can be found everywhere in our natural environment, in biological systems as well as in man-made objects. Within these geometric shapes, physical, chemical or biological processes may take place and may be mathematically modeled by partial differential equations. Using standard discretization methods to solve these problems requires a triangulation of the complicated domain, which is still a challenge in 3D. In particular, this holds when the domain evolves in time and a new triangulation is needed at each time step. To circumvent these problems various methods have been proposed. In most methods the complicated domain is embedded in a larger, simpler domain. While it is in general easy to extend the PDE to the larger domain, it is not clear how to incorporate the original boundary conditions. Among these methods are the fictitious domain method, composite finite element method, extended finite elements, immersed interface method and ghost fluid method. The drawback of all these methods is that they require nonstandard tools which are typically not available in standard finite element or finite difference software packages.

There are few other techniques to handle complex domains with standard discretizations. In this case the boundary conditions can be incorporated by Lagrange multipliers, the penalty method or using the diffuse domain approach [LLRV09], which we will follow here.

In the diffuse domain approach a phase field ψ is used to represent the characteristic function of the complex domain. The phase field enters the PDE and new source terms are introduced to approximate the boundary conditions. Although the approach is general, we begin by illustrating the method for a simple test problem. Let us consider an instationary heat equation in a complex domain $\Omega_1 \subset \Omega$ which may move over time and with Neumann boundary conditions:

$$\partial_t C + \nabla \cdot (\mathbf{u}C) - \Delta C = f \qquad \text{in } \Omega_1 \times [0, T] \qquad (2.55)$$

$$\mathbf{n} \cdot \nabla C = g \qquad \text{on } \partial\Omega_1 \times [0, T] \qquad (2.56)$$

$$C = C_0 \qquad \text{on } \Omega_1 \times 0 \qquad (2.57)$$

Note, that we have assumed $\mathbf{u} \cdot \mathbf{n} = V$, where V is the normal velocity of $\partial\Omega_1$. Let ξ be a test function with compact support in $\Omega \times (0, T)$. Note, that this implies that ξ vanishes at the boundary of Ω and at the start time 0 and end time T. This allows us to write the weak formulation of Eqs. (2.55),(2.56) as

$$\int_0^T \int_{\Omega_1} -C\partial_t\xi + \nabla\xi \cdot (\nabla C - \mathbf{u}C) - f\xi \, dx \, dt = \int_0^T \int_{\partial\Omega_1} g\xi \, dA \, dt \qquad (2.58)$$

where we have used that $\mathbf{u} \cdot \mathbf{n} = V$ and a weak form of $\partial_t C$ can be written as:

$$\int_0^T \int_{\Omega_1} \partial_t C \xi \, dx \, dt = \int_0^T \int_{\Omega_1} \partial_t (C\xi) - C \partial_t \xi \, dx \, dt \tag{2.59}$$

$$= \int_0^T \frac{d}{dt} \int_{\Omega_1} C\xi \, dx \, dt + \int_0^T \int_{\partial\Omega_1} C\xi V \, dA \, dt - \int_0^T \int_{\Omega_1} C\partial_t \xi \, dx \, dt$$
$$\tag{2.60}$$

$$= \int_0^T \int_{\partial\Omega_1} C\xi V \, dA \, dt - \int_0^T \int_{\Omega_1} C\partial_t \xi \, dx \, dt. \tag{2.61}$$

We can now use the characteristic function χ of Ω_1 and the surface delta function $\delta_{\partial\Omega_1}$ to extend Eq. (2.58) over whole Ω and get

$$\int_0^T \int_\Omega -\chi C \partial_t \xi + \chi \nabla \xi \cdot (\nabla C - \mathbf{u}C) - \chi f \xi \, dx \, dt = \int_0^T \int_\Omega \delta_{\partial\Omega_1} g\xi \, dx \, dt \tag{2.62}$$

Now, given a phase field ψ which is ≈ 1 in Ω_1 and ≈ 0 in $\Omega \backslash \Omega_1$ we can approximate the characteristic function ($\psi \approx \chi$) and the surface delta function (e.g. $|\nabla\psi| \approx \delta_{\partial\Omega_1}$), which leads to

$$\int_0^T \int_\Omega -\psi C \partial_t \xi + \psi \nabla \xi \cdot (\nabla C - \mathbf{u}C) - \psi f \xi \, dx \, dt = \int_0^T \int_\Omega |\nabla\psi| g\xi \, dx \, dt \tag{2.63}$$

Integrating by parts, and going back to the strong formulation gives

$$\partial_t (\psi C) + \nabla \cdot (\psi \mathbf{u}C) - \nabla \cdot (\psi \nabla C) - g|\nabla\psi| = \psi f \qquad \text{in } \Omega \tag{2.64}$$

Eq. (2.64) is now valid in whole Ω and can therefore be implemented with standard finite element or finite difference toolboxes. Using matched asymptotic expansion it can be shown that as the interface thickness ϵ tends to zero, Eq. (2.64) approximates the original Eqs. (2.55),(2.56), see [LLRV09].

The presented approach to reformulate equations in complex, evolving domains can also handle Dirichlet and Robin boundary conditions. It is also possible to treat more difficult equations. See, for example [ALM+12] where the approach has been used to solve the equations of linear elasticity. In chapter 4 the method is adapted to solve the Navier-Stokes and Cahn-Hilliard equations in moving domains.

A special case of the method is when the complex domain is a hypersurface. In this case the diffuse domain approach is replaced by the diffuse interface approach, proposed in [RV06]. Let us consider an interface transport equation on a hypersurface $\Gamma \subset \Omega$,

$$\partial_t c + \nabla_\Gamma \cdot (\mathbf{u}c) = D_c \Delta_\Gamma c + j \qquad \text{on } \Gamma \tag{2.65}$$

The diffuse interface method uses similar ideas as the above diffuse domain approach. Additionally it makes use of the fact that the surface gradients reduce to ordinary gradients when c is extended off Γ

constant in normal direction. The diffuse interface version of Eq. (2.65) can be formally written as

$$\partial_t(\delta_\Gamma c) + \nabla \cdot (\delta_\Gamma \mathbf{u} c) = D_c \nabla \cdot (\delta_\Gamma \nabla c) + \delta_\Gamma j \qquad \text{in } \Omega \qquad (2.66)$$

The constant extension of c in the direction normal to the interface is ensured by putting δ_Γ into the Laplacian of c. Now, any phase field approximation for δ_Γ can be used to solve the latter equation (see Sec. 2.2). Again, by means of matched asymptotic analysis, agreement with the original interface equation can be shown [RV06].

2.6 Diffuse Interface Models for Two-Phase Flow

2.6.1 Classical models

We consider isothermal, incompressible flow of two immiscible fluids. In the classical approach the interface between both fluids is usually considered as a free boundary that evolves in time. The movement of the interface is determined by a set of interfacial balance conditions. In the classical sharp interface model, the Navier-Stokes equations determine the evolution of the fluid velocities:

$$\rho_i \left(\frac{\partial \mathbf{u}_i}{\partial t} + \mathbf{u}_i \cdot \nabla \mathbf{u}_i \right) = -\nabla p_i + \nabla \cdot (\nu_i \mathbf{D}(\mathbf{u}_i)) + \mathbf{F}_i, \quad \text{in } \Omega_i \qquad (2.67)$$

$$\nabla \cdot \mathbf{u}_i = 0, \quad \text{in } \Omega_i \qquad (2.68)$$

where $\Omega_i \subset \mathbb{R}^2$ or $\Omega_i \subset \mathbb{R}^3$, for $i = 1, 2$ denote the two fluid domains and ρ_i, $\mathbf{u}_i$, p_i, ν_i, $\mathbf{F}_i$ are the density, velocity, pressure, viscosity and body force in domain Ω_i, respectively. Across the interface Γ separating the domains, the following jump conditions hold:

$$[\mathbf{u}]_\Gamma = \mathbf{0}, \quad [-p\mathbf{I} + \nu \mathbf{D}(\mathbf{u})]_\Gamma \cdot \mathbf{n} = -\sigma \kappa \mathbf{n} + \nabla_\Gamma \sigma, \qquad (2.69)$$

where $[f]_\Gamma = f_1 - f_2$ denotes the jump in f across Γ, $\mathbf{I}$ is the identity tensor, $\mathbf{D}(\mathbf{u}) = \left(\nabla \mathbf{u} + (\nabla \mathbf{u})^T \right)$, $\mathbf{n}$ is the normal vector to Γ pointing into Ω_2, σ is the surface tension and κ is the mean curvature of the interface (positive for a sphere of Ω_1). Let $\Omega = \Omega_1 \cup \Gamma \cup \Omega_2$. If the boundary of the fluid domain $\partial\Omega$ is solid, the no-slip condition is imposed. In the event that the interface Γ intersects a solid boundary, another boundary condition needs to be provided. For an interface in equilibrium, a contact angle condition (Young's law) may be posed

$$\cos\theta = \frac{\sigma_{2S} - \sigma_{1S}}{\sigma}, \qquad (2.70)$$

where θ is the (equilibrium) contact angle, σ_{iS} is the interfacial energy between the solid and component i. The contact angle characterizes the wettability of the surface with $\theta = 0$ denoting complete wetting. However, in the dynamical setting with the no-slip condition, the force needed to move a contact line is infinite making it necessary to regularize the system (e.g., [Dav02]). Numerous methods have been implemented to regularize the problem including introducing a slip velocity, microscopic interactions,

a precursor film or a diffuse interface (e.g., see [de 85, KC94, ODB97, Ber98, Jaq99]) Here, we follow the diffuse interface approach, which was originally developed to model solid-liquid phase transitions, see e.g. [AMW98, Emm08, SLS08].

2.6.2 Diffuse interface approximation

In diffuse interface models the interface is represented as a thin layer of finite thickness and an auxiliary phase field function, is used to indicate the phases, see Sec. 2.2. The phase field function varies smoothly between distinct values in both phases and the interface can be associated with an intermediate level set of the phase field function. Diffuse interface approaches for mixtures of two immiscible, incompressible fluids lead to the Navier-Stokes-Cahn-Hilliard equations and have been considered by several authors, see e.g. [Jaq99, Fen06, KW07]. We also refer the reader to [ZYF$^+$10] for recent 3D applications in Newtonian and viscoelastic flows. For constant surface tension the model reads:

$$\rho \left(\partial_t \mathbf{u} + (\mathbf{u} \cdot \nabla) \mathbf{u} \right) = -\nabla p + \nabla \cdot (\nu \mathbf{D}(\mathbf{u})) + \mathbf{F} + \mu \nabla \psi, \tag{2.71}$$

$$\nabla \cdot \mathbf{u} = 0, \tag{2.72}$$

$$\partial_t \psi + u \cdot \nabla \psi = \nabla \cdot (M(\psi) \nabla \mu), \tag{2.73}$$

$$\mu = \tilde{\sigma} \epsilon^{-1} B'(\psi) - \tilde{\sigma} \epsilon \Delta \psi, \tag{2.74}$$

in the domain Ω. Here $\mathbf{u}$, p, ψ and μ are the (mass-averaged) velocity, pressure, phase field variable and chemical potential, respectively. The function $B(\psi)$ is a double well potential. As also discussed in Sec. 2.2 a typical choice for B is $B(\psi) = 1/4(\psi^2 - 1)^2$ such that $\psi \approx 1$ in Ω_1 and $\psi \approx -1$ in Ω_2. The function $M(\psi)$ is a mobility. In practice, M is often either a constant or a double well potential similar to B. Furthermore ρ, ν and $\mathbf{F}$ are again the density, viscosity and body force. The parameter ϵ defines the interface thickness, $\tilde{\sigma}$ is a scaled surface tension, which is related to the physical surface tension σ by $\sigma = k_\sigma \tilde{\sigma}$ to match the diffuse interface surface energy $\tilde{\sigma} \int_\Omega \frac{1}{\epsilon} B(\psi) + \frac{\epsilon}{2} |\nabla \psi|^2$ to the physical surface energy $\int_\Gamma \sigma$. As we have seen in Sec. 2.2 the scaling factor k_σ is dependent on B and for the above choice of B we get $\tilde{\sigma} = \sigma \frac{3}{2\sqrt{2}}$.

In general for the diffuse interface fluid method, it is desirable to keep M small such that one primarily gets advection. At the same time the mobility needs to be big enough to ensure that the interface profile stays accurately modeled and the interface thickness is approximately constant. Asymptotic analysis shows that this can be achieved by taking $M = O(\epsilon)$. In this case the diffuse interface model converges to Eq. (2.71) - (2.74) with $\rho_1 = \rho_2 = \rho$ and $\nu_1 = \nu_2 = \nu$ if the width of the interfacial layer ϵ tends to zero. Gurtin et al. [GPV96] showed thermodynamic consistency of this model.

Furthermore $\nu = \nu(\psi)$ and $\mathbf{F} = \mathbf{F}(\psi)$ are interpolations of the viscosity and body force, e.g. $\nu(\psi) = \nu_1(1 + \psi)/2 + \nu_2(1 - \psi)/2$. Various extensions of this model have been proposed to account for variable densities. In chapter 3 we will present the most common models of this kind and compare them in a benchmark study.

Finally, assuming that $\partial\Omega$ is a solid boundary, the conditions at $\partial\Omega$ may be posed as

$$\mathbf{u} \;\; = \;\; \mathbf{0}, \quad \text{(no slip)} \tag{2.75}$$

$$\mathbf{n}\cdot\nabla\mu \;\; = \;\; 0, \quad \text{(no flux)} \tag{2.76}$$

$$\mathbf{n}\cdot\nabla\psi \;\; = \;\; \frac{1}{\epsilon\sqrt{2}}\cos(\theta)(1-\psi^2), \quad \text{(contact angle)} \tag{2.77}$$

$\mathbf{n}$ is the outward normal to Ω. Further, as in Eq. (2.70), θ is the equilibrium contact angle. Eq. (2.77) naturally arises by incorporating a wall free energy in the diffuse interface formulation, see [Jaq99, VA06, GPSW07, DQA09] for details. Note, that the equipartition of energy implies that $\frac{1}{\epsilon\sqrt{2}}(1-\psi^2) = |\nabla\psi|$ and therefore Eq. (2.77) yields the correct contact angle condition, which is $\mathbf{n}\cdot\frac{\nabla\psi}{|\nabla\psi|} = \cos(\theta)$.

2.7 The Phase-Field-Crystal (PFC) model

The scope of this thesis is to investigate the influence of particles on a binary fluid mixture. This poses the question of how to simulate particles in a way that is suitable for a coupling to flow equations. The most common approach to model bulk particle dynamics is probably Molecular Dynamics (MD) simulation, where trajectories of molecules and atoms are determined by solving Newton's equations of motion and where forces between the particles are defined by molecular mechanics force fields. However the coupling to flow equations is hardly feasible since MD simulations operate on atomic time scales (of the order of pico seconds). An alternative way to model particle interactions are Lattice Boltzmann methods and approximations to dynamic density functional theory (DDFT), which is our model of choice here.

DDFT is a time-dependent extension of classical (equilibrium) density functional theory and describes the time evolution of the density of interacting Brownian particles through an integro-differential equation (e.g., see Refs.[MT99, AM04]). Classical density functional theory has been previously used for determining equilibria in one dimension of mixtures of amphiphillic particles (e.g., see Refs.[NLS00, CO02]) and for modeling colloidal fluids (e.g. see Refs.[MT99, Arc09]). In the DDFT, the dynamic integro-differential equations for the particle density can be derived from Newton's equations of motion with and without inertial effects. In recent work, van Teeffelen et al. [vTBVL09] derived a local higher order partial differential equation for the colloid particle density by approximating the integro-differential equation of the DDFT model. The resulting partial differential equation is the so-called phase-field-crystal (PFC) model, which was previously introduced by Elder et al.[EKHG02, EPB$^+$07] in the context of crystal growth. As the model resolves each particle as a density peak, it requires sub-particle resolution. However, the model operates on diffusive time scales which enables the approach to resolve the long term behavior of the system. The PFC model has been used to describe various solid state phenomena, see for example Refs.[PDA$^+$07, PE10]. In very recent work, Backofen et al.[BWV10] modified the PFC model to describe crystallography on fixed, curved surfaces which is related to the ordering of colloids on fluid-fluid interfaces.

The central idea of the PFC model is to consider the nondimensional time averaged colloidal density $\varrho := (\varrho_{crys} - \bar\varrho_{crys})/\bar\varrho_{crys}$ where ϱ_{crys} is the time-averaged colloid density and $\bar\varrho_{crys}$ a reference

density, for example, the density of the system in the liquid state. In this way the thermal vibrations that the particles exert in MD models are averaged out (see schematic below).
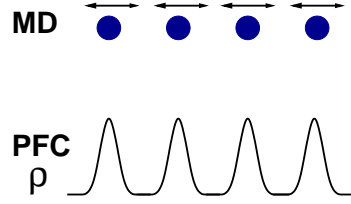
The evolution of ϱ can be described by the conserved dynamics arising from a Swift-Hohenberg (SH)-like energy [SH77]: $\frac{d\varrho}{dt} = \nabla \cdot \left(M\nabla \frac{\delta E_{SH}}{\delta \varrho} \right)$, where M is a mobility, $\frac{\delta E_{SH}}{\delta \varrho}$ denotes the variational derivative of the SH-like energy E_{SH} with respect to ϱ. E_{SH} is given by

$$E_{SH} = k_B T \int f_{SH}(\varrho) \, dx, \tag{2.78}$$

where k_B is the Boltzmann constant, T the temperature and the SH energy density f_{SH} is given by

$$f_{SH}(\varrho) = \frac{\varrho^2}{2}\left(a + \tilde{\beta}q_0^4\right) + \frac{g}{4}\varrho^4 - \tilde{\beta}q_0^2|\nabla\varrho|^2 + \frac{\tilde{\beta}}{2}(\Delta\varrho)^2. \tag{2.79}$$

The quantities a, $\tilde{\beta}$, q_0, and g are system specific parameters. The first three can be determined from matching the liquid structure factor for the colloidal system with q_0^{-1} setting the crystal lattice spacing, and a and $\tilde{\beta}$ being determined by a polynomial approximation to the liquid structure factor. The remaining parameter g can be determined by fixing the amplitude of density waves in the crystal state. See Refs. [EPB+07, WK07, vTBVL09, BWV10], for example, where the connections between the PFC model and the classical Dynamic Density Functional Theory (DDFT) are also discussed.

Next, let us nondimensionalize (2.78) where nondimensional quantities will be denoted by tildes. Choosing the characteristic space scale $1/q_0$ we define the nondimensional length scale $\tilde{\mathbf{x}} = \mathbf{x}q_0$ and the undercooling parameter $r = a/(\tilde{\beta}q_0^4)$. The nondimensional SH energy will be denoted by $E_{PFC} = E_{SH}/(k_B T \tilde{\beta}^2 q_0^5/g)$. Taking $\rho = \sqrt{\frac{g}{\beta q_0^4}}\varrho$ (e.g. see also Ref.[WV09]) yields

$$E_{PFC} = \int \frac{\rho^4}{4} + \frac{\rho^2}{2}(1+r) - |\tilde{\nabla}\rho|^2 + \frac{1}{2}\left(\tilde{\Delta}\rho\right)^2 d\tilde{x}. \tag{2.80}$$

This form of the energy is also known as the Phase Field Crystal (PFC) energy. The name Phase Field Crystal was given to it by Elder and Grant [EG04] who derived E_{PFC} from phenomenological considerations to model crystal growth. They postulated that the energy of a crystal system is minimized when the distance between neighboring particles is the crystal lattice spacing. This implies that ρ in equilibrium must be a periodic function. Elder and Grant then constructed the simplest free energy which is minimized by periodic states of ρ. Starting with a Ginzburg-Landau energy (2.2) they invert the sign of the gradient term to make spatial gradients in ρ favorable. To avoid infinite gradients in ρ, a next-order gradient term is included, which leads to the PFC energy E_{PFC}.

As mentioned earlier, the PFC model is concerned with the conserved dynamics arising from minimization of this energy:

$$\frac{d\rho}{dt} = \nabla \cdot \left(M \nabla \frac{\delta E_{PFC}}{\delta \rho} \right). \tag{2.81}$$

In 1D the equilibrium solution of (2.81) can be a constant (i.e. periodic in zero dimensions) or a one-dimensional periodic function. In 2D the latter corresponds to a striped phase and additionally the energy is minimized by two-dimensional periodic functions, i.e. triangular/hexagonal distributions of particles. Which one of these three solutions occurs depends on the temperature parameter r and the average particle density $\bar{\rho}$ and can be determined from the phase diagram (Fig. 2.4).

The 1D periodic equilibrium solution of (2.81) can be approximated by $\rho = A \sin(2\pi x/q) + \bar{\rho}$, the so-called one-mode approximation, with constants A and q. Inserting into (2.80) and scaling by q gives the energy per unit length

$$\frac{E_{PFC}}{q} := \frac{1}{q} \int_0^q \frac{\rho^4}{4} + \frac{\rho^2}{2}(1+r) - |\tilde{\nabla}\rho|^2 + \frac{1}{2}\left(\tilde{\Delta}\rho\right)^2 d\tilde{x} \tag{2.82}$$

$$= -2A^2\pi^2 \left(-\frac{2\pi^2}{q^4} + \frac{1}{q^2} \right) + \frac{1}{q} \int_0^q \frac{\rho^4}{4} + \frac{\rho^2}{2}(1+r) \tag{2.83}$$

Expanding q up to second order around the equilibrium particle distance 2π gives

$$\frac{E_{PFC}}{q} \approx -\frac{A^2}{4} + \frac{A^2}{4\pi^2}(q - 2\pi)^2 + \frac{1}{q} \int_0^q \frac{\rho^4}{4} + \frac{\rho^2}{2}(1+r) \tag{2.84}$$

Neglecting the integral term this means that the energy per unit length increases when q deviates from its equilibrium, which is basically Hooke's law $[E = E_0 + k(q - q_0)^2]$. In this sense the PFC model intrinsically includes elastic interactions of the particles.
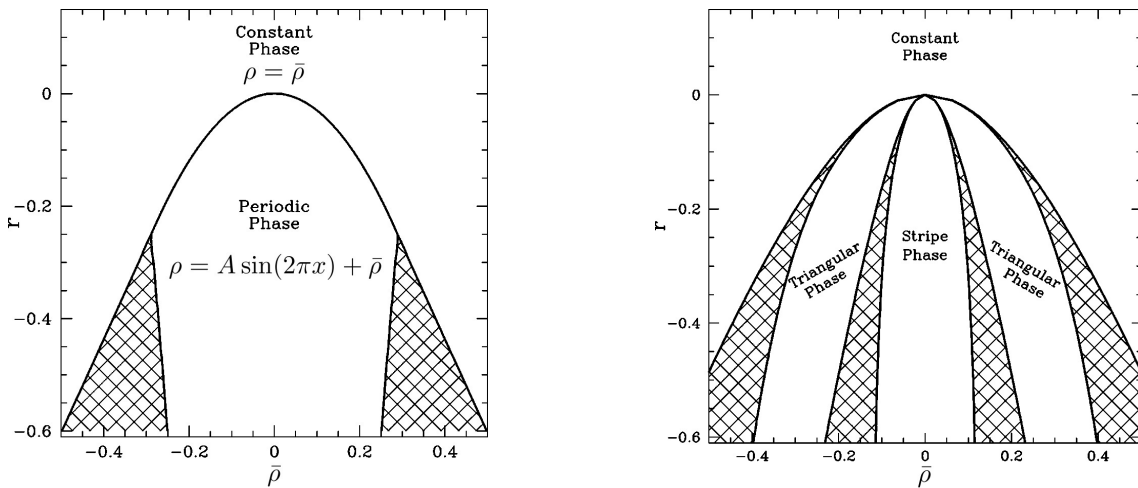

Figure 2.4: Phase diagram of the one mode approximation in 1D (left) and 2D (right). The hatched regions correspond to regions of liquid/crystal coexistence. Images from [EG04].

Chapter 3

Benchmark computations of diffuse interface models for variable density

In [HTK$^+$09] a numerical benchmark configuration was proposed for two-dimensional bubble dynamics. Two benchmark test cases were considered, both concern the evolution of a single bubble rising in a liquid column while undergoing shape deformations. The first case considers a small density and viscosity ratio, for which the bubble undergoes only moderate shape deformations, and the second case considers a bubble with a very low density compared to the surrounding fluid, which leads to large deformations and topological changes. Different numerical approaches have been quantitatively compared, among them are Eulerian level set finite element methods as well as an arbitrary Lagrangian-Eulerian moving grid approach. Diffuse interface approximations for two-phase flow problems have not been considered to date. In this chapter we will test finite element discretizations of different diffuse interface models for two-phase flow problems on both benchmark test cases. The outline of this chapter is as follows. In Sec. 3.1 we will review diffuse interface models for two-phase flow with variable densities. The numerical treatment of these models is described in Sec. 3.2. Sec. 3.3 presents the test cases and compares the results of the different models with the reference solutions from [HTK$^+$09]. Conclusions are drawn in Sec. 3.4.

3.1 Diffuse interface models for variable density

Diffuse interface approximations have been successfully used to describe two-phase flow problems with constant density in both phases for various applications. The standard model dates back to Hohenberg and Halperin [HH77] and was introduced in detail in Sec. 2.6.2. However, this model is only valid for equal densities of both fluids. To treat problems with small density ratios, a common practice is to use a Boussinesq approximation where an external gravitational force is added to model the effect of a density difference. The resulting model remains thermodynamically consistent. The approach however is not valid for large density ratios. Lowengrub and Truskinovsky [LT98] derived a thermodynamically consistent extension to the model of Hohenberg and Halperin, which allows also for large differences

in densities. However the velocity field is no longer divergence free and the coupling between the Navier-Stokes equation and the evolution equation of the phase-field function becomes much stronger, which makes numerical computation harder. Alternative generalizations for different densities have been discussed by Boyer [Boy02], Ding et al. [DSS07], Shen and Yang [SY10] and most recently by Abels et al. [AGG10]. In all approaches the velocity remains divergence free, thermodynamic consistency however could only be shown for the models proposed in [SY10, AGG10].

The model used in [DSS07, SY10] uses Eqs. (2.71) - (2.74) but with variable density and viscosity given by $\rho(\psi) = \rho_1(\psi + 1)/2 + \rho_2(\psi - 1)/2$ and $\nu(\psi) = \nu_1(\psi + 1)/2 + \nu_2(\psi - 1)/2$, respectively. We refer to Sec. 2.6.2 for a definition of the variables and parameters. The model reads:

model 1

$$\rho(\psi)\left(\partial_t \mathbf{u} + (\mathbf{u} \cdot \nabla)\mathbf{u}\right) = -\nabla p + \nabla \cdot (\nu(\psi)\mathbf{D}(\mathbf{u})) + \mathbf{F} + \mu\nabla\psi, \tag{3.1}$$

$$\nabla \cdot \mathbf{u} = 0, \tag{3.2}$$

$$\partial_t \psi + \mathbf{u} \cdot \nabla\psi = \nabla \cdot (M(\psi)\nabla\mu), \tag{3.3}$$

$$\mu = \tilde{\sigma}\epsilon^{-1}B'(\psi) - \tilde{\sigma}\epsilon\Delta\psi. \tag{3.4}$$

Following Guermond and Quartapelle [GQ00] an energy estimate of the model could be shown by introducing the new variable $r = \sqrt{\rho}$, see [SY10]. Boyer [Boy02] follows a different approach. The starting point for the derivation are the equations of linear momentum of each fluid. The model reads:

model 2

$$\rho(\psi)\left(\partial_t \mathbf{u} + (\mathbf{u} \cdot \nabla)\mathbf{u}\right) = -\nabla p + \nabla \cdot (\nu(\psi)\mathbf{D}(\mathbf{u})) + \mathbf{F} + \mu\nabla\psi \tag{3.5}$$
$$+ (\rho_2 - \rho_1)\frac{1 - \psi^2}{4}\nabla\frac{\mu}{\rho(\psi)},$$

$$\nabla \cdot \mathbf{u} = 0, \tag{3.6}$$

$$\partial_t \psi + \mathbf{u} \cdot \nabla\psi = \nabla \cdot \left(\frac{M(\psi)}{\rho(\psi)}\nabla\frac{\mu}{\rho(\psi)}\right), \tag{3.7}$$

$$\mu = \tilde{\sigma}\epsilon^{-1}B'(\psi) - \tilde{\sigma}\epsilon\Delta\psi, \tag{3.8}$$

As far as we know neither global nor local energy inequalities are known for this model. Abels et al. [AGG10] consider the following thermodynamically consistent model:

model 3

$$\partial_t(\rho(\psi)\mathbf{u}) + \nabla \cdot (\rho(\psi)\mathbf{u} \otimes \mathbf{u}) = -\nabla p + \nabla \cdot (\nu(\psi)\mathbf{D}(\mathbf{u})) + \mathbf{F} + \mu\nabla\psi \tag{3.9}$$
$$- \nabla \cdot \left(\mathbf{u} \otimes \frac{\rho_1 - \rho_2}{2}M(\psi)\nabla\mu\right),$$

$$\nabla \cdot \mathbf{u} = 0, \tag{3.10}$$

$$\partial_t \psi + \mathbf{u} \cdot \nabla\psi = \nabla \cdot (M(\psi)\nabla\mu), \tag{3.11}$$

$$\mu = \tilde{\sigma}\epsilon^{-1}B'(\psi) - \tilde{\sigma}\epsilon\Delta\psi, \tag{3.12}$$

for which convergence to the classical two-phase flow equations was shown using a formal matched asymptotic analysis for $\epsilon \to 0$.

3.2 Finite element discretization

For the numerical solution of the three models we adapt existing algorithms for the Navier-Stokes-Cahn-Hilliard equation, e.g. [VA06, DQA09]. Let T_h be a triangulation of the domain Ω and let $J_\tau = \{t_m\}_{m=0}^{NTS}$ be a quasi-uniform partition of $[0, T]$ of mesh size $\tau := \frac{T}{NTS}$. Here, NTS stands for the number of time steps. Of course, adaptive time steps may also be used. We define the discrete time derivative $d_t v^m := (v^m - v^{m-1})/\tau$, where the upper index denotes the time step number. Furthermore, for a non-negative integer r, let $P_r(K)$ denote the space of polynomials of degree less than or equal to r on a triangle or tetrahedron $K \in T_h$. We introduce the finite element spaces

$$
\begin{aligned}
M_h &= \{q \in L_0^2(\Omega) | q_{|K} \in P_{r_q}(K)\}, \\
V_h &= \{v \in C^0(\bar{\Omega}) \cap H_0^1(\Omega) | v_{|K} \in P_{r_v}(K)\}, \\
Y_h &= \{\eta \in C^0(\bar{\Omega}) | \eta_{|K} \in P_{r_\psi}(K)\}
\end{aligned}
$$

and denote by $\mathbf{V}_h = (V_h)^d$ the space of vector test functions in dimension d.

The Cahn-Hilliard and Navier-Stokes systems are solved separately in an operator splitting manner. For both systems we use an implicit Euler time stepping algorithm. Higher order algorithms for the individual systems are applicable as well (see e.g. [TSLV10]).

3.2.1 Cahn-Hilliard system

At every time step we first solve the Cahn-Hilliard equations and then solve the Navier-Stokes system. The finite element approximation of the convective Cahn-Hilliard equation reads: Find $(\psi^m, \mu^m) \in Y_h \times Y_h$ such that for all $(\eta, \xi) \in Y_h \times Y_h$

model 1

$$
\begin{aligned}
(d_t\psi^m, \eta) + (\mathbf{u}^{m-1} \cdot \nabla\psi^m, \eta) + (M(\psi^{m-1})\nabla\mu^m, \nabla\psi) &= 0, \quad (3.13) \\
(\mu^m, \xi) - \tilde{\sigma}\epsilon(\nabla\psi^m, \nabla\xi) - \tilde{\sigma}\epsilon^{-1}(B'(\psi^m), \xi) &= 0, \quad (3.14)
\end{aligned}
$$

model 2

$$
\begin{aligned}
(d_t\psi^m, \eta) + (\mathbf{u}^{m-1} \cdot \nabla\psi^m, \eta) + (\frac{M(\psi^{m-1})}{\rho^{m-1}}\nabla\mu^m, \nabla\psi) &= 0, \quad (3.15) \\
(\rho^{m-1}\mu^m, \xi) - \tilde{\sigma}\epsilon(\nabla\psi^m, \nabla\xi) - \tilde{\sigma}\epsilon^{-1}(B'(\psi^m), \xi) &= 0. \quad (3.16)
\end{aligned}
$$

model 3

$$(d_t\psi^m,\eta) + (\mathbf{u}^{m-1}\cdot\nabla\psi^m,\eta) + (M(\psi^{m-1})\nabla\mu^m,\nabla\psi) = 0, \qquad (3.17)$$

$$(\mu^m,\xi) - \tilde{\sigma}\epsilon(\nabla\psi^m,\nabla\xi) - \tilde{\sigma}\epsilon^{-1}(B'(\psi^m),\xi) = 0, \qquad (3.18)$$

where (f,g) denotes the $L^2(\Omega)$ inner product. As double well potential here we use $B(\psi) = \frac{1}{4}(\psi^2 - 1)^2$ which results in the scaled surface tension $\tilde{\sigma} = \sigma\frac{3}{2\sqrt{2}}$ (see Secs. 2.2, 2.6.2). We set the mobility to $M(\psi) = \gamma B(\psi)$, where γ is a constant mobility coefficent. To obtain a linear system we linearize the derivative of the double well potential $B'(\psi^m)$ by a Taylor expansion of order one:

$$B'(\psi^m) \approx (\psi^{m-1})^3 - \psi^{m-1} + (3(\psi^{m-1})^2 - 1)(\psi^m - \psi^{m-1}).$$

3.2.2 Navier-Stokes system

After the Cahn-Hilliard system has been solved we can define the variable density and viscosity by $\rho^m = \rho_1(\psi^m + 1)/2 + \rho_2(\psi^m - 1)/2$ and $\nu^m = \nu_1(\psi^m + 1)/2 + \nu_2(\psi^m - 1)/2$, respectively. Since gravity is the only body force, we set $\mathbf{F} = \rho\mathbf{g}$ where $\mathbf{g}$ denotes the gravitational vector field. Now, the finite element approximation for the Navier-Stokes equations is as follows. Find $(\mathbf{u}^m, p^m) \in \mathbf{V}_h \times M_h$ such that for all $(\mathbf{v}, q) \in \mathbf{V}_h \times M_h$

model 1

$$(\rho^m d_t\mathbf{u}^m,\mathbf{v}) + (\nu^m\mathbf{D}(\mathbf{u}^m),\nabla\mathbf{v}) + (\rho^m(\mathbf{u}^{m-1}\cdot\nabla)\mathbf{u}^m,\mathbf{v}) - (p^m,\nabla\cdot\mathbf{v})$$
$$= (\rho^m\mathbf{g} + \mu^m\nabla\psi^m,\mathbf{v}), \qquad (3.19)$$
$$(\nabla\cdot\mathbf{u}^m,q) = 0, \qquad (3.20)$$

model 2

$$(\rho^m d_t\mathbf{u}^m,\mathbf{v}) + (\nu^m\mathbf{D}(\mathbf{u}^m),\nabla\mathbf{v}) + (\rho^m(\mathbf{u}^{m-1}\cdot\nabla)\mathbf{u}^m,\mathbf{v}) - (p^m,\nabla\cdot\mathbf{v})$$
$$= (\rho^m\mathbf{g} + \rho^m\mu^m\nabla\psi^m + (\rho_2 - \rho_1)\frac{1 - (\psi^m)^2}{4}\nabla\mu,\mathbf{v}) \qquad (3.21)$$
$$(\nabla\cdot\mathbf{u}^m,q) = 0, \qquad (3.22)$$

model 3

$$(d_t(\rho\mathbf{u})^m,\mathbf{v}) + (\nu^m\mathbf{D}(\mathbf{u}^m),\nabla\mathbf{v}) - (\rho^m\mathbf{u}^{m-1}\otimes\mathbf{u}^m,\nabla\mathbf{v}) - (\rho^m\mathbf{g} + \mu^m\nabla\psi^m,\mathbf{v})$$
$$= (p^m,\nabla\cdot\mathbf{v}) + \left(\mathbf{u}^m\otimes\frac{\rho_1 - \rho_2}{2}M(\psi^m)\nabla\mu^m,\nabla\mathbf{v}\right) \qquad (3.23)$$
$$(\nabla\cdot\mathbf{u}^m,q) = 0. \qquad (3.24)$$

3.2.3 Numerical treatment

The adaptive finite element toolbox AMDiS [VV07] is used for discretization. We use a standard Taylor-Hood element for the Navier-Stokes equation with polynomial degree two for $\mathbf{u}$ and one for p. The elements discretizing the concentration ψ and chemical potential μ were chosen with polynomial degree two, although one could take elements of any polynomial degree. We used equal polynomial order for $\mathbf{u}$ and ψ to simplify the quantitative evaluation of the results using the open-source data analysis software ParaView (www.paraview.org). The linearized system was solved using the direct unsymmetric multifrontal method (UMFPACK, [Dav04]).

Adaptive meshes are indispensable for providing a high spatial resolution along the fluid-fluid interface described implicitly by ψ. To compare our results appropriately we used a fixed resolution along the interface to control the grid sizes. While the domain away from the interface is refined with an equidistant mesh of grid size h, we used a finer grid at the interface with grid size $h_{int} = 1/8h$, in all our simulations. The resulting meshes are similar to meshes generated using an L^2-like error indicator based on a jump residual (e.g., [Ver96, VV07]). Note, that rigorous error estimates in h and ϵ only exist for simpler problems like the Allen-Cahn equation (see [FW05]).

3.3 Definition of the test and results

3.3.1 Test setup

The test setup is extensively described in [HTK$^+$09]. The domain $\Omega = [0,1] \times [0,2]$ is filled with fluid 1 ($\psi \approx 1$) except for a circular bubble which consists of fluid 2 ($\psi \approx -1$). The initial bubble has a radius of 0.25 with its center at $(0.5, 0.5)$. The parameters of the outer fluid are $\rho_1 = 1000$, $\mu_1 = 10$. In the inner fluid $\rho_2 = 100$, $\mu_2 = 1$ for test case 1 and $\rho_2 = 1$ and $\mu_2 = 0.1$ for test case 2. The gravitational force is given by $\mathbf{g} = (0, 0.98)$. The surface tension is $\sigma = 24.5$ for test case 1 and $\sigma = 1.96$ for test case 2. As boundary conditions we take the no-slip condition $\mathbf{u} = 0$ at the top and bottom boundaries in a rectangular domain, as well as the free-slip condition $\mathbf{u} \cdot \mathbf{n} = \mathbf{t} \cdot \mathbf{D}(\mathbf{u}) \cdot \mathbf{n} = 0$, with the tangent vector $\mathbf{t}$, on the vertical walls.

Since the density of the bubble is smaller than the density of the surrounding fluid ($\rho_2 < \rho_1$) the bubble rises. The evolution of the bubble is tracked for 3 time units during which the defined benchmark quantities are measured.

3.3.2 Benchmark quantities and error quantification

For a rigorous estimation of the accuracy of the simulation we used the same quantities as in [HTK$^+$09]. The measured quantities are:

- center of mass

$$y_c = \frac{\int_{\psi<0} y \, dx}{\int_{\psi<0} 1 \, dx}$$

with y the vertical coordinate $(x, y) := \mathbf{x}$,

- circularity

$$c = \frac{\text{perimeter of area-equivalent circle}}{\text{perimeter of bubble}} = \frac{2\sqrt{\int_{\psi<0} \pi dx}}{P_b}$$

with the perimeter P_b, which is obtained by integration over a 'contour' filter in ParaView.

- rise velocity

$$V_c = \frac{\int_{\psi<0} v \, dx}{\int_{\psi<0} 1 \, dx}$$

where v is the second (vertical) component of the velocity $\mathbf{u}$.

All defined quantities are time dependent. A relative error can be defined to measure their temporal evolution. We use the error norms:

$$||e||_1 = \frac{\sum_{t=1}^{NTS} |q_{t,ref} - q_t|}{\sum_{t=1}^{NTS} |q_{t,ref}|}, \quad ||e||_2 = \left(\frac{\sum_{t=1}^{NTS} |q_{t,ref} - q_t|^2}{\sum_{t=1}^{NTS} |q_{t,ref}|^2} \right)^{1/2}, \quad ||e||_\infty = \frac{\max_t |q_{t,ref} - q_t|}{\max_t |q_{t,ref}|}$$

where q_t is the temporal evolution of quantity q. We take the data of group 3 from [HTK$^+$09] on the finest grid as reference solution $q_{t,ref}$. Spline interpolation is used to match the time steps of the reference solution with our solution. Using the so defined errors, a rate of convergence (ROC) can be computed.

The numerical parameters used are shown in Tab. 3.1. The mobility coefficient γ is an additional numerical parameter which is not present in the sharp interface model. The value is chosen as small as possible according to the numerical performance. Since the coupling between Navier-Stokes and Cahn-Hilliard equation is done explicitly, the CFL condition $\tau \lesssim h^{\frac{3}{2}}$ needs to be satisfied. However, In this work we assume that the time step size is sufficiently small that τ can be refined proportional to h. Furthermore ϵ is chosen proportional to h which keeps the number of elements along the interface fixed. Here, we have around 3 elements along the interface. As we use quadratic basis functions this resolution is assumed to be sufficient since it is common to use 4-6 degrees of freedom along the interface.

3.3.3 Results for test case 1

The bubble, being initially circular, first stretches horizontally and develops a dimple at the bottom before it reaches a stable ellipsoidal shape. As in [HTK$^+$09] we tabulate the total number of degrees of freedom (NDOF), the total number of time steps (NTS) and the overall computing time in seconds

(CPU), see Tab. 3.2. Since the implementation of the three models only differs in some terms, the measured CPU times are almost equal for all models.

Fig. 3.1 shows the bubble shapes at the final time ($t = 3$). The bubble shapes clearly differ for different values of ϵ but converge so that there is no obvious difference for the finest values $\epsilon = 0.01$ and $\epsilon = 0.005$. The bubble shapes for model 2 look unlike to those of models 1 and 3 but seem to converge to the same shape as the other models do. No significant differences can be seen between the models 1 and 3.
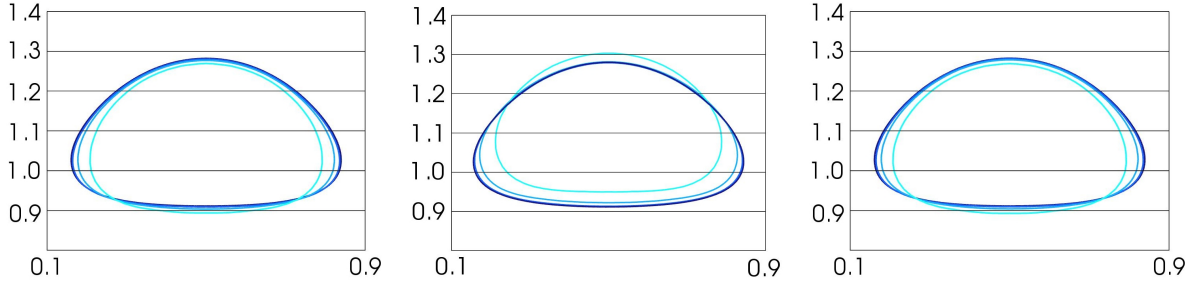

Figure 3.1: Bubble shapes at time $t = 3$ for $\epsilon = 0.04$ (light blue), $\epsilon = 0.02$ (blue), $\epsilon = 0.01$ (dark blue), $\epsilon = 0.005$ (black) for model 1 - 3 (from left to right). Color online.

It is clearly not sufficient to only look at the bubble shapes, therefore we use the previously defined benchmark quantities. We compare the solutions of the three different models and plot the minimum circularity, maximum rise velocity and final center of mass for all models versus the reference solution from [HTK$^+$09] in Fig. 3.2. All three models seem to approach the reference solution for decreasing ϵ. The differences between the models 1 and 3 are very small and vanish as ϵ decreases. Model 2 deviates from the other two.
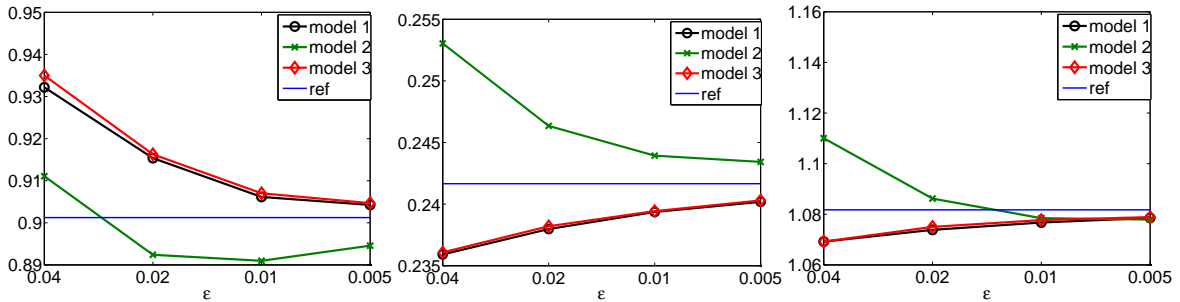
Figure 3.2: Minimum circularity, maximum rise velocity and final center of mass (from left to right) for test case 1 and model 1 - 3 in comparison to the reference solution. Color online.

h_{int}	ϵ	τ	$\gamma_{1,3}$	γ_2
1/16	0.040	0.008	0.000040	40.0
1/32	0.020	0.004	0.000020	20.0
1/64	0.010	0.002	0.000010	10.0
1/128	0.005	0.001	0.000005	5.0

Table 3.1: Used numerical parameters for all computations: grid resolution h_{int}, diffuse interface width ϵ and time step size τ. The mobility coefficient $\gamma_{1,3}$ used for model 1 and 3 is different to γ_2 used for model 2 due to the different definitions of the Cahn-Hilliard diffusion.

ϵ	NDOF[1]	NTS[1]	CPU[1]
0.040	2900	375	140
0.020	6400	750	600
0.010	14800	1500	3240
0.005	39800	3000	18240

Table 3.2: Simulation statistics and timings for model 1. The total number of degrees of freedom (NDOF), the total number of time steps (NTS) and the overall computing time in seconds (CPU). The values for model 2 and 3 differ only slightly.

More detailed results of the three models can be found in the appendix A. Tabs. A.1 - A.3 show the quantitative comparison with the benchmark values for all three models. The circularity, center of mass and rise velocity versus time for all models are plotted in figs. A.1 - A.3. To increase the readability we omit the coarsest grid results ($\epsilon = 0.04$) here. In general, one can see that each quantity approaches the reference value from [HTK$^+$09] as ϵ decreases. The plots for model 1 and 3 are indistinguishable whereas model 2 exhibits slightly different time evolutions of all quantities.

The relative error norms for the circularity, center of mass, and rise velocity are shown in Tabs. A.4 - A.6 together with the estimated relative order of convergence (ROC). To calculate the ROC we use the reference solution from [HTK$^+$09]. The ROC is in all error norms around 1 for models 1 and 3. For model 2 we obtain negative orders of convergence at some points. This indicates that this model does not (or not yet) converge to the reference solution. However the relative errors are comparable to those of models 1 and 3. Note that in [HTK$^+$09] the convergence has been calculated assuming the solution on the finest grid as exact solution. Hence, we additionally use this approach in this work. For each model we assume its finest grid solution to be the exact solution and show errors and orders of convergence in Tab. A.7. We only display the $|| \cdot ||_1$ norm but the results are very similar in the other two norms. The ROC is in all error norms between 1 and 2, for model 2 even above 2.

3.3.4 Results for test case 2

In test case 2 the decrease in surface tension causes the bubble to develop a more non-convex shape and thin filaments, which eventually break off. This is a much harder problem and as with [HTK$^+$09], agreement between the numerical approaches could not be achieved. It remains unclear if break off really should occur for these settings. The results in [HTK$^+$09] show that the size of the filaments might become very small (e.g. 0.01). In such cases one can expect phase field methods to encounter problems, since the filament size can be close to the interface thickness ϵ.

We again compare bubble shapes at final time for different values of ϵ, see fig 3.3. For $\epsilon = 0.04$ there are visible differences between the three models. In contrast to the results in [HTK$^+$09] none of our models exhibits break off. Splitting did not even occur in tests with smaller ϵ and higher grid resolution ($\epsilon = 0.0005$, $h_{int} = 1/1024$). However, one can see that in all models the filaments become thinner for smaller ϵ. Therefore it is possible that break off does occur for $\epsilon \rightarrow 0$.

For smaller ϵ there is good agreement with the reference solution, prior to break off, in terms of bubble shape. The number of degrees of freedom (NDOF) and CPU time are comparable to test case 1, see Fig.3.2.
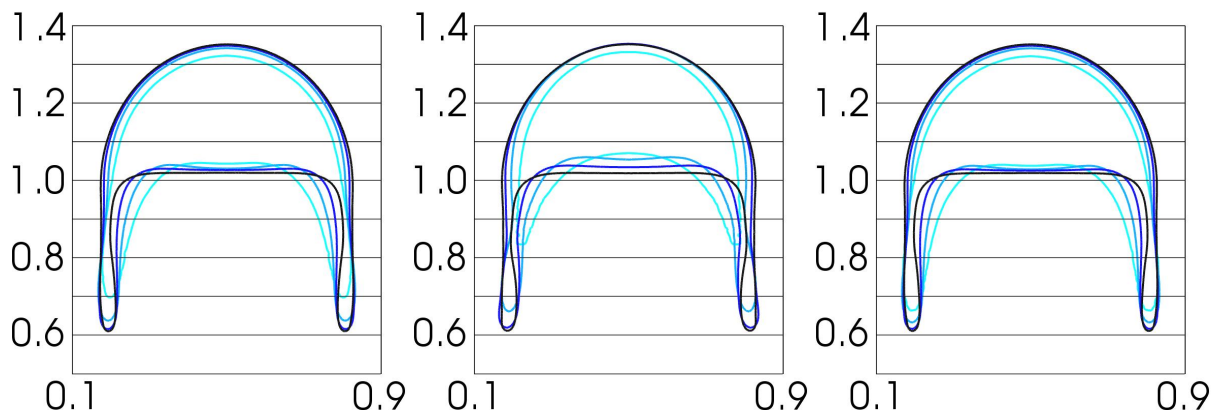
Figure 3.3: Bubble shapes for test case 2 at time $t = 3$ for $\epsilon = 0.04$ (light blue), $\epsilon = 0.02$ (blue), $\epsilon = 0.01$ (dark blue), $\epsilon = 0.005$ (black) for model 1 - 3 (from left to right). Color online.

We give the values of the benchmark quantities in Tabs. A.8-A.10. Due to the absence of break off behavior in our simulations and the lack of agreement within the reference solution for later times, we have restricted the comparison to the time interval $[0, 2]$. We plot the minimum circularity, maximum rise velocity and final center of mass for all models versus the reference solution from [HTK$^+$09] in Fig. 3.4. Again, the differences between the models 1 and 3 are very small for the circularity and center of mass. However, for the maximum rise velocity we observe quite high deviations, in particular for bigger values of ϵ. Although model 2 behaves differently to models 1 and 3, it is closer to the reference solution than the other two models for all benchmark quantities. It is not clear if all three models really approach the reference solution for decreasing ϵ.
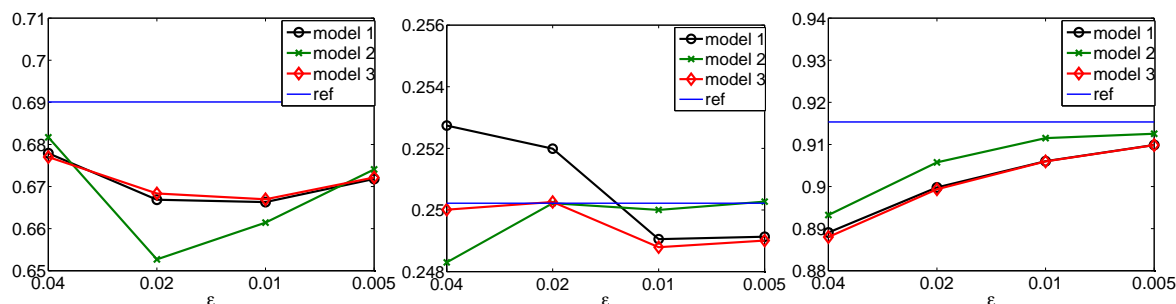
Figure 3.4: Minimum circularity, maximum rise velocity and final center of mass (from left to right) for test case 2 and model 1 - 3 in comparison to the reference solution. Color online.

More detailed results of the three models can be found in the appendix. The circularity, center of mass and rise velocity versus time are plotted in figs. A.4-A.6. All quantities appear to converge for each model. However, even for the finest grid ($\epsilon = 0.005$) differences remain visible. We conclude that the resolution is still not fine enough to get sufficiently close to the reference solution. The plots for models 1 and 3 are almost indistinguishable whereas model 2 exhibits different time evolutions of all quantities.

The relative error norms for the circularity, center of mass, and rise velocity are shown in Tabs. A.11 - A.13 together with the estimated relative order of convergence (ROC). To calculate the errors we use the reference solution from [HTK$^+$09]. The ROC for the models 1 and 3 is in general less than 1, which is clearly less than in test case 1. For model 2 we again obtain negative orders of convergence

for the circularity for bigger ϵ which indicates that this model does not yet converge to the reference solution. However the relative errors are comparable to those of models 1 and 3. Again, to make a fair comparison to the orders of convergence given in [HTK$^+$09] we assume the solution on the finest grid to be the exact solution. Errors and orders of convergence are shown in Tab. A.14. We display only the $||\cdot||_1$ norm but the results are very similar for the other two norms. The observed ROC is more or less 1, which is significantly less than in test case 1.

3.4 Summary

Diffuse interface models for two-phase flow have gained a lot of attention recently, since they can easily handle moving contact lines and topological transitions without any need for reinitialisation or convection stabilization. Various diffuse interface models have been proposed to deal with different densities and viscosities in both fluid phases. Three of them, namely the models of Boyer [Boy02], Ding et al. [DSS07] and Abels et al. [AGG10] are compared in this work by applying them to the benchmark problem proposed in Hysing et al. [HTK$^+$09]. To our knowledge this is the first benchmark comparison done for this type of models and the first comparison of these diffuse interface models with one another.

The benchmark is divided into two test cases which both concern the evolution of a single bubble rising in a liquid column. We find that all three models agree well with the results from [HTK$^+$09] if the bubble undergoes only moderate shape deformations (test case 1). The time-averaged errors are higher but the estimated order of convergence towards the finest grid solution is approximately 2 and therefore comparable to the results of Hysing et al. We see first order convergence towards the reference solution of [HTK$^+$09]. The second test case is far more challenging and it is not clear if the diffuse interface models converge to the same benchmark values as those presented in [HTK$^+$09]. Contrary to the results of [HTK$^+$09], no break off occurred in our simulations. However, our calculations indicate first order convergence towards the finest grid solution and lower order of convergence with respect to the reference solution. In both test cases the differences between the calculated benchmark values of the models of Ding et al. [DSS07] and Abels et al. [AGG10] are small and decrease as the interface thickness tends to zero. We conclude that diffuse interface methods in combination with adaptive mesh refinement are comparable with level set approaches in terms of accuracy and computational effort..

Chapter 4

Two-phase flow in complex geometries: A diffuse domain approach

4.1 Introduction

Many applications of multiphase flows in engineering and the physical and biological sciences involve complex flow geometries, interfacial physics and the motion of contact lines separating immiscible components at solid boundaries. These are highly challenging problems for numerical simulation. For example, special treatment of the contact line is needed to regularize the stress singularity. Further, standard methods require the discretization of the complicated domain, which rules out coarse-scale discretizations and efficient multi-level solutions. In addition the automatic generation of proper three-dimensional meshes for complex geometries remains a challenge. Moreover, in many applications the complex geometry might even evolve in time which would require a new discretization at each time step.

Because of the importance of solving multiphase flows in complex geometries, a variety of different numerical techniques have been developed. In the fictitious domain approach (e.g., see [GPH+01, YTPFT02, GPP06, YS07, PPGJ09]), the complex geometry is embedded in a larger, simpler domain, the discretization is performed in this larger domain and Lagrange multipliers are used to enforce the correct boundary conditions at solid/fluid interfaces. Other approaches in this direction enlarge the set of test functions to account for the boundary conditions. Examples include the extended finite element method (e.g., [DBO00, MB96, ODZ98]), the immersed interface method (e.g., [GLL08, LLW03]). Other approaches include boundary integral methods (e.g., [May84, Kro99, BYZ03]) which explicitly incorporate the boundary conditions in the reformulated equations, front-tracking (e.g., [TBE+01, ART02, ART04, MK06]) and Eulerian-Lagrangian methods (e.g., [UKSTST97, HPZ01, UMRK01, USS09]) which utilize a separate Lagrangian mesh to track the complex boundary and either smear the boundary conditions across several mesh points, or explicitly enforce the boundary conditions on the Lagrangian mesh which cuts across the Eulerian mesh using body forces or modified discretizations. Other methods along these lines include level-set, immersed interface, ghost-fluid and cut-cell

methods (e.g., [ZMOW98, Bal04, KAK03, TF03, GS05, Chu06, XW06, COER07, GICM07, Lin07, GA08, MDB⁺07, DSR06, BGS08, SGV09, dZGW⁺09]). Most of this work does not deal directly with multiple-phase contact lines as the classical equations have a stress singularity (e.g., [Dav02]). To remove the singularity, various regularizations have introduced including the use of a slip velocity, microscopic interactions, a precursor film or a diffuse interface (e.g., see [de 85, KC94, ODB97, Ber98, Jaq99]). Current implementations primarily use body-fitted meshes.

All methods, discussed thus far, require nonstandard tools and are therefore typically not available in standard finite element or finite difference software packages. The complex geometry is either given explicitly through a surface triangulation or implicitly as a level set function. Building on previous work [KLR03, LR05, FCKR05, BOPGF06, BOPG06], [LLRV09] used a phase-field function to represent the complex domain and developed a diffuse domain method for solving partial differential equations (PDEs) in complex, stationary or moving geometries with Dirichlet, Neumann and Robin boundary conditions, see Sec. 2.5. In this approach the complex geometry was embedded into a larger regular domain and a phase-field function was used to smoothly approximate the characteristic function of the original domain. Accordingly, the sharp boundary of the original domain was replaced by a narrow diffuse interface layer. The original PDE was reformulated on the larger, regular domain with additional source terms that approximate the boundary conditions. The reformulated PDE was shown to converge to the original PDE and boundary conditions as the width of the diffuse interface layer tends to zero. The diffuse domain approach does not require any modification of standard finite element or finite difference software and thus offers a simple way to solve general equations in complex geometries. The diffuse domain approach has recently been extended to account for coupling among PDEs defined in a bulk domain and on a surface and was used to investigate the evolution of multiphase flows with soluble surfactants [TLL⁺09, TSLV10]. Here, we apply this approach to simulate two-phase flows in complex geometries taking into account contact lines separating immiscible components.

In particular, we combine the diffuse domain approach for solving PDEs in complex geometries with the diffuse-interface (phase-field) method for simulating multiphase flows. The new diffuse-domain method for multiphase flows is straightforward to implement using either finite difference or finite element discretizations; we follow the latter here. The method differs from previous implementations of diffuse interface (phase-field) methods for interactions among multiphase flows and simple-shaped solid structures (e.g. [Jaq99, GPSW07, VA06, DQA09, ZYF⁺10]), in that the geometry and boundary conditions are described implicitly. Accordingly, the fluid and component concentration equations are reformulated and solved in a larger regular domain with the boundary conditions being modeled using source terms rather than being implemented directly at the boundary of a body-fitted mesh as in the references above.

We present numerical examples demonstrating the effectiveness of the diffuse domain method for simulating multiphase flows in complex geometries. We simulate multiphase flow in a driven cavity on an extended domain and find very good agreement with results obtained by solving the equations and boundary conditions in the original domain. We then consider successively more complex geometries and simulate a droplet sliding down a rippled ramp in 2D and 3D, a droplet flowing through a Y-junction in a microfluidic network and finally chaotic mixing in a droplet flowing through a winding, serpentine channel. The latter example actually incorporates two different diffuse domains: one

describes the evolving droplet where mixing occurs while the other describes the channel.

The outline of the chapter is as follows. In section 4.2 we present diffuse domain formulation of the multiphase flow model. In section 4.3, the discretizations of the equations are presented. In section 4.4, the numerical results are given. Finally, in section 4.5, conclusions are drawn and future research directions are discussed.

4.2   Diffuse domain Navier-Stokes Cahn-Hilliard model

We now reformulate the NSCH system (2.71)-(2.77) using the diffuse domain method [LLRV09] in a larger, regular domain $\tilde{\Omega}$ which contains Ω. Since we also consider moving domains, we have to allow the interface to move with a certain velocity $\mathbf{g}$ which results in replacing the no-slip boundary condition (2.75) by $\mathbf{u} = \mathbf{g}$ at $\partial\Omega$.

A phase field function ϕ is introduced to approximate the characteristic function of the domain Ω: $\phi \approx 1$ in Ω and $\phi \approx 0$ in $\tilde{\Omega}/\Omega$ and the solid boundary Γ, which may be time dependent, is described implicitly through ϕ, e.g., $\Gamma(t) = \{\mathbf{x}|\phi(\mathbf{x},t) = 1/2\}$. For example, we may take $\phi(\mathbf{x},t) = 0.5(1 - \tanh(3r(\mathbf{x},t)/\epsilon_\phi))$ where $r(\mathbf{x},t)$ is the signed distance from a point $\mathbf{x}$ to Γ and ϵ_ϕ is the thickness of the solid boundary transition layer. Here, we take $\epsilon_\phi = \epsilon$ unless otherwise stated. Alternatively, ϕ may be determined as the solution of an advective Cahn-Hilliard equation [TLL$^+$09].

Following the general formulation given in [LLRV09], the NSCH system may be rewritten to implicitly embed the boundary conditions in the equations to yield the diffuse domain NSCH system (DDNSCH)

$$\partial_t(\phi\mathbf{u}) + \nabla \cdot (\phi\mathbf{u}\mathbf{u}^T) = -\phi\nabla p + \nabla \cdot (\nu\phi\mathbf{D}) + \frac{\tilde{\sigma}}{\epsilon}\phi\mu\nabla\psi + \phi\mathbf{F} + BC_u, \tag{4.1}$$

$$\nabla \cdot (\phi\mathbf{u}) = \mathbf{g} \cdot \nabla\phi, \tag{4.2}$$

$$\partial_t(\phi\psi) + \nabla \cdot (\phi\psi\mathbf{u}) = \nabla \cdot (\phi M(\psi)\nabla\mu) + BC_\mu, \tag{4.3}$$

$$\phi\mu = \phi B'(\psi) - \epsilon^2\nabla \cdot (\phi\nabla\psi) + BC_\psi, \tag{4.4}$$

in $\tilde{\Omega}$, with boundary conditions $\mathbf{u} = 0$, $\mathbf{n} \cdot \nabla\psi = \mathbf{n} \cdot \nabla\mu = 0$ on $\partial\tilde{\Omega}$; the system is not sensitive to the boundary conditions imposed on $\partial\tilde{\Omega}$. We have additionally assumed that the solid boundary velocity $\mathbf{g}$ may extended off Γ. As double well potential we use here $B(\psi) = 1/4(\psi^2 - 1)^2$ which results in the scaled surface tension $\tilde{\sigma} = \sigma\frac{3}{2\sqrt{2}}$ (see sections 2.2, 2.6.2). For the mobility we chose $M = \gamma B$ with a constant mobility factor γ. The terms BC_u, BC_μ and BC_ψ impose the internal boundary conditions on the implicitly defined solid boundary. Different formulations of the internal boundary conditions are provided by [LLRV09]. We use

$$BC_u = -\frac{\beta}{\epsilon_\phi^3}(1 - \phi)(\mathbf{u} - \mathbf{g}), \tag{4.5}$$

where β is a scaling factor, to enforce the usual no slip condition $\mathbf{u} = 0$,

$$BC_\psi = -\frac{\epsilon}{\sqrt{2}}\cos(\theta)(1 - \psi^2)|\nabla\phi| \tag{4.6}$$

to enforce the wetting condition $\mathbf{n} \cdot \nabla \psi = \frac{1}{\epsilon\sqrt{2}} \cos(\theta)(1 - \psi^2)$, and

$$BC_\mu = 0. \tag{4.7}$$

In [LLRV09] $\beta = 1$, but in fact other choices are possible ranging from $\beta \sim 1$ to ϵ_ϕ, as can be seen from the asymptotic analysis in [LLRV09]. We have implemented other boundary approximations from [LLRV09] for BC_u and BC_ψ and found that other choices yield similar results. Interestingly, we found that if one uses $\phi\nabla \cdot (\nu\mathbf{D})$ instead of $\nabla \cdot (\nu\phi\mathbf{D})$ for the viscous term, the results are again similar. However, using $\nabla(\phi p)$ instead of $\phi\nabla p$ does not work.

We also remark that the form of BC_ψ given above assumes that the boundary condition $h := \mathbf{n} \cdot \nabla \psi$ is extended off Γ as a constant in the normal direction [LLRV09]. Since $h = \frac{1}{\epsilon\sqrt{2}} \cos(\theta)(1 - \psi^2)$, it is not clear that this is indeed the case because the interface layer in ψ may signficantly overlap the boundary layer around Γ, described by a rapid transition in ϕ. However, numerical tests suggest that this form of BC_ψ works well. Indeed, if one assumes that the presence of the interface layer in ψ does not affect the (inner) asymptotic expansions in the boundary layer around Γ, e.g. $\epsilon_\phi << \epsilon$, then one may conclude that ψ is constant in the transition layer across Γ, which is sufficient to show convergence to the original boundary condition on Γ [LLRV09].

If we assume that ϕ is advected by the velocity $\mathbf{u}$

$$\partial_t \phi + \mathbf{u} \cdot \nabla \phi = 0, \tag{4.8}$$

noting that $\mathbf{u}|_\Gamma = \mathbf{g}$, then Eqs. (4.1) and (4.3) may be simplified to

$$\phi\left(\partial_t\mathbf{u} + \mathbf{u} \cdot \nabla\mathbf{u}\right) = -\phi\nabla p + \nabla \cdot (\nu\phi\mathbf{D}) + \frac{\tilde{\sigma}}{\epsilon}\phi\mu\nabla\psi + \phi\mathbf{F} + BC_u. \tag{4.9}$$

$$\phi\left(\partial_t\psi + \mathbf{u} \cdot \nabla\psi\right) = \nabla \cdot (\phi M(\psi)\nabla\mu) + BC_\mu. \tag{4.10}$$

These simplifications should not be used if ϕ satisfies the advective Cahn-Hilliard equation.

We next provide a brief explanation for the form of Eq. (4.2). To begin, write the weak form of $\nabla \cdot \mathbf{u} = 0$ in Ω as

$$\int_\Omega \mathbf{u} \cdot \nabla\eta \, d\mathbf{x} = \int_\Gamma \eta\mathbf{g} \cdot \mathbf{n} \, dS, \tag{4.11}$$

where η is an appropriate test function and $\mathbf{n}$ is the outward normal to Ω. Let χ be the characteristic function of Ω (i.e. $\chi(\mathbf{x}, t) = 1$ if $\mathbf{x} \in \Omega$ and $\chi = 0$ otherwise). Then, we can extend Eq. (4.11) to $\tilde{\Omega}$ by

$$\int_{\tilde{\Omega}} \chi\mathbf{u} \cdot \nabla\eta \, d\mathbf{x} = \int_{\tilde{\Omega}} \eta\mathbf{g} \cdot \mathbf{n}|\nabla\chi| \, d\mathbf{x}, \tag{4.12}$$

where we have used that $|\nabla\chi| = \delta_\Gamma$ the surface delta function. Integrating the left hand side of Eq.

(4.12) by parts we get

$$\int_{\tilde{\Omega}} \eta\left(-\nabla \cdot (\chi \mathbf{u}) - \mathbf{g} \cdot \mathbf{n} |\nabla \chi|\right) \, d\mathbf{x} = 0, \tag{4.13}$$

since the boundary terms vanish on $\partial \tilde{\Omega}$ due to χ. Taking $\chi \approx \phi$, $\mathbf{n} = -\nabla\phi/|\nabla\phi|$ and asking that the above holds for arbitrary η gives Eq. (4.2).

The DDNSCH system thus consists of Eqs. (4.1) or (4.9), (4.2), (4.3) or (4.10), and (4.4). The advantage of this system is that it is posed on a regular domain and can be solved by any standard approach. The sharp interface limit $\epsilon \to 0$ is an interesting question because of the underlying singularity in the sharp interface model (in the absence of a slip velocity or other regularizing terms). If the interface does not intersect solid boundaries, then the classical sharp interface equations (2.67)-(2.69) are obtained (e.g., [LT98]). If the sharp interface intersects the solid boundary, then the question is still open. Our numerical results are inconclusive in this case as we find that the rate of convergence in ϵ decreases as $\epsilon \to 0$.

4.3 Finite element discretization

For the numerical solution of the DDNSCH system we use the same discretization techniques in space and time as in the previous chapter (see section 3.2). For both systems we use an implicit Euler time stepping algorithm. At every time step we first solve the Navier-Stokes system and then solve the Cahn-Hilliard equations. If ϕ needs to be evolved, then ϕ is updated before $\mathbf{u}$ and ψ.

4.3.1 Diffuse domain Navier-Stokes system

The finite element approximation for the diffuse domain Navier-Stokes equations (in simplified form) is as follows. Find $(\mathbf{u}^m, p^m) \in \mathbf{V}_h \times M_h$ such that for all $(\mathbf{v}, q) \in \mathbf{V}_h \times M_h$

$$(\phi^m d_t \mathbf{u}^m, \mathbf{v}) + (\nu^{m-1} \phi^m \mathbf{D}^m, \nabla \mathbf{v}) \quad + \quad (\phi^m (\mathbf{u}^{m-1} \cdot \nabla)\mathbf{u}^m, \mathbf{v}) - (\phi^m p^m, \nabla \cdot \mathbf{v})$$

$$-(\nabla \phi^m p^m, \mathbf{v}) - (BC_{u^m}, \mathbf{v}) \quad = \quad (\phi^m \mathbf{F} + \frac{\tilde{\sigma}}{\epsilon} \phi^m \mu^{m-1} \nabla \psi^{m-1}, \mathbf{v}), \tag{4.14}$$

$$(\nabla \cdot (\phi^m \mathbf{u}^m), q) \quad = \quad (\nabla \phi^m \cdot \mathbf{g}^m, q), \tag{4.15}$$

where (f, g) denotes the $L^2(\tilde{\Omega})$ inner product. Also note that the term $\phi \nabla p$ has been replaced by $\nabla(\phi p) - p \nabla \phi$. This approach has two benefits. First, it does not involve any derivatives of p. Second, combined with the incompressibility condition in Eq. (4.2), this choice maintains the saddle point structure of the original Navier-Stokes system. This was found to be essential for the solvability of the discrete system. To show the saddle point structure, in 2D for simplicity, we denote the ansatz functions by v_i and q_i, respectively, and write the resulting 2D system as

$$\begin{bmatrix} A & 0 & C_x \\ 0 & A & C_y \\ B_x & B_y & 0 \end{bmatrix} \begin{bmatrix} u_x^m \\ u_y^m \\ p^m \end{bmatrix} = \begin{bmatrix} b_x \\ b_y \\ 0 \end{bmatrix}, \tag{4.16}$$

where

$$(A)_{ij} = \int_{\tilde{\Omega}} \phi^m \left(\frac{1}{\tau} v_j v_i + \nu \nabla v_j \nabla v_i + \left(\mathbf{u}^{m-1} \cdot \nabla v_j \right) v_i \right) + \frac{\beta}{\epsilon_\phi^3} (1 - \phi^m) v_j v_i \, d\mathbf{x}$$

$$(C_x)_{ij} = - \int_{\tilde{\Omega}} \phi^m \frac{\partial v_i}{\partial x} q_j + \frac{\partial \phi^m}{\partial x} v_i q_j \, d\mathbf{x},$$

$$(B_x)_{ij} = \int_{\tilde{\Omega}} \phi^m \frac{\partial v_j}{\partial x} q_i + \frac{\partial \phi^m}{\partial x} v_j q_i \, d\mathbf{x}$$

$$(b_x)_i = \int_{\tilde{\Omega}} \phi^m \left(f_x + \frac{\tilde{\sigma}}{\epsilon} \mu^{m-1} \frac{\partial \psi^{m-1}}{\partial x} \right) \cdot v_i + \frac{\beta}{\epsilon_\phi^3} (1 - \phi^m) g_x v_i \, d\mathbf{x},$$

with $(u_x^m, u_y^m) := \mathbf{u}^m$, $(f_x, f_y) := \mathbf{F}$, $(g_x, g_y) := \mathbf{g}$. The terms B_y, C_y and b_y are defined analogously. Hence one can see that the condition $[B_x \quad B_y] = -[C_x \quad C_y]^T$, which is satisfied for the original Navier-Stokes equations, is still fulfilled in the diffuse domain formulation.

4.3.2   Diffuse domain Cahn-Hilliard system

In the case of a stationary domain ($\phi^m = \phi$), the finite element approximation for the convective diffuse domain Cahn-Hilliard equations (in simplified form) is as follows. Find $(\psi^m, \mu^m) \in Y_h \times Y_h$ such that for all $(\eta, \xi) \in Y_h \times Y_h$

$$(\phi d_t \psi^m, \eta) + (\phi \mathbf{u}^m \cdot \nabla \psi^m, \eta) - (\phi M(\psi^{m-1}) \nabla \mu^m, \nabla \psi) = 0, \qquad (4.17)$$

$$(\phi \mu^m, \xi) + \epsilon^2 (\phi \nabla \psi^m, \nabla \xi) - (\phi B'(\psi^m), \xi) - (BC_{\psi^m}, \xi) = 0. \qquad (4.18)$$

The second term of Eq. (4.17) can be rewritten using integration by parts and Eq. (4.2) to give

$$
\begin{aligned}
(\phi \mathbf{u}^m \cdot \nabla \psi^m, \eta) &= (\nabla \cdot (\phi \mathbf{u}^m \psi^m), \eta) - (\psi^m \nabla \cdot (\phi \mathbf{u}^m), \eta) \\
&= \int_{\partial \tilde{\Omega}} \eta \phi \psi^m \mathbf{u}^m \cdot \mathbf{n} \, d\Gamma - (\phi \mathbf{u}^m \psi^m, \nabla \eta) - (\nabla \cdot (\phi \mathbf{u}^m), \psi^m \eta) \\
&= -(\phi \mathbf{u}^m \psi^m, \nabla \eta).
\end{aligned}
$$

In this form we obtain volume conservation of ψ^m on Ω which follows by setting $\eta = 1$: $\int_{\tilde{\Omega}} \phi \psi^m \, d\mathbf{x} =$ const. Furthermore, we linearize the derivative of the double well potential $B'(\psi^m)$ by a Taylor expansion of order one:

$$B'(\psi^m) \approx (\psi^{m-1})^3 - \psi^{m-1} + (3(\psi^{m-1})^2 - 1)(\psi^m - \psi^{m-1})$$

to obtain a linear system but keeping the non-linearity (semi)-implicit. To obtain conservation when the domain is moving, the original form of the phase field equation (4.3) should be used and Eq. (4.17) should be replaced with

$$(d_t(\phi^m \psi^m), \eta) - (\phi^m \mathbf{u}^m \nabla \psi^m, \nabla \eta) - (\phi^m M(\psi^{m-1}) \nabla \mu^m, \nabla \eta) = 0, \qquad (4.19)$$

from which conservation, $\int_{\tilde{\Omega}} \phi^m \psi^m \, d\mathbf{x} = \text{const}$, clearly follows.

4.3.3 Numerical treatment

The adaptive finite element toolbox AMDiS [VV07] is used for discretization. In 2D the polynomial degree was chosen to be two for u and one for p, ψ and μ. The linearized system was solved using the direct unsymmetric multifrontal method (UMFPACK, [Dav04]).

In 3D, the linear systems become too large and a different approach is needed. We also use linear basis functions for $\mathbf{u}$ and a simple projection method to solve the Navier-Stokes equations. In this first order method proposed in [Cho68] momentum and incompressibility equation are solved successively. The scheme is given by

$$
\begin{aligned}
\phi^m \frac{\mathbf{u}^* - \mathbf{u}^{m-1}}{\tau} &- \nabla \cdot (\phi^m \nu^{m-1} \mathbf{D}^*) \\
+\phi^m \mathbf{u}^{m-1} \cdot \nabla \mathbf{u}^* - BC_{\mathbf{u}^*} &= \phi^m \mathbf{f} + \frac{\tilde{\sigma}}{\epsilon} \phi^m \mu^{m-1} \nabla \psi^{m-1} \quad (4.20) \\
\tau \nabla \cdot (\phi^m \nabla p^*) &= \nabla \cdot (\phi^m \mathbf{u}^*) - \nabla \phi^m \cdot \mathbf{g} \quad (4.21) \\
\mathbf{u}^m &:= \mathbf{u}^* - \tau \nabla p^*. \quad (4.22)
\end{aligned}
$$

In Eq. (4.20), $\mathbf{D}^* = \nabla \mathbf{u}^* + \nabla \mathbf{u}^{*T}$. We use BiCGStab(ell) to solve Eq. (4.20) and the Cahn-Hilliard system and a CG method to solve Eq. (4.21). To ensure the well-posedness of the equations for all calculations, ϕ is replaced by $\phi + \delta$, see [RV06, LLRV09] for details. Here, we use $\delta = 10^{-6}$.

4.3.4 Adaptivity

Adaptive meshes are indispensable for providing a high spatial resolution along the internal boundary Γ, described implicitly by ϕ, and the fluid-fluid interfaces described implicitly by ψ. For local mesh adaptation, we use a L^2-like error indicator based on a jump residual (e.g., [Ver96, VV07]) for ϕ and ψ to maintain approximately 5 grid points across the transition layers. Although we did not find it necessary to do here, additional mesh refinement can be used to increase local resolution of the flow field (e.g., velocity gradients, etc.).

4.4 Numerical examples

4.4.1 Driven cavity flow

First, we simulate flow in a driven cavity to compare the results of the DDNSCH system on an extended domain with the NSCH model on the physical domain. Parameters are as in [Boy02], the viscosity is $\nu = 0.002$, the mobility coefficient is $\gamma = 0.001$, the surface tension is $\tilde{\sigma} = 0$, the contact angle is $\theta = 90^o$ and the interface thickness is $\epsilon_\phi = \epsilon = 0.01$. The scaling factor is $\beta = \nu$. We solve the NSCH equations (2.71)-(2.74) on the physical domain $\Omega = [0, 1.0]^2$, with boundary conditions (2.75)-(2.77), and compare the results with the DDNSCH equations (4.1)-(4.4) on the enlarged domain

$\tilde{\Omega} = [-0.25, 1.25]^2$. At the upper boundary the velocity in horizontal direction is imposed to be

$$u_x(x, y) = \begin{cases} \max(0, 1.0 - 4.0(x - 0.5)^2) & y \geq 1.0 - \epsilon \\ 0 & y < 1.0 - \epsilon. \end{cases}$$

All remaining boundary velocities are set to be zero.

Figure 4.1 shows the phase-field function ψ for the initial condition (flat interface) and at time $t = 15$ obtained from the NSCH system (left) and the DDNSCH system (right) with a box indicating the location of the physical domain Ω. There is good quantitative agreement between the models. Next we investigate the $\epsilon_\phi \to 0$ limit, holding $\epsilon = 0.01$ fixed. In Figure 4.2 we present the difference $||\psi(T)_{DD} - \psi(T)_{phys\ domain}||_{L^2}$ as a function of ϵ_ϕ for different choices of β. All choices of β generally show the error decreasing as a function of ϵ_ϕ, for ϵ_ϕ sufficiently small, but that the best results are obtained taking $\beta \sim \epsilon_\phi$.
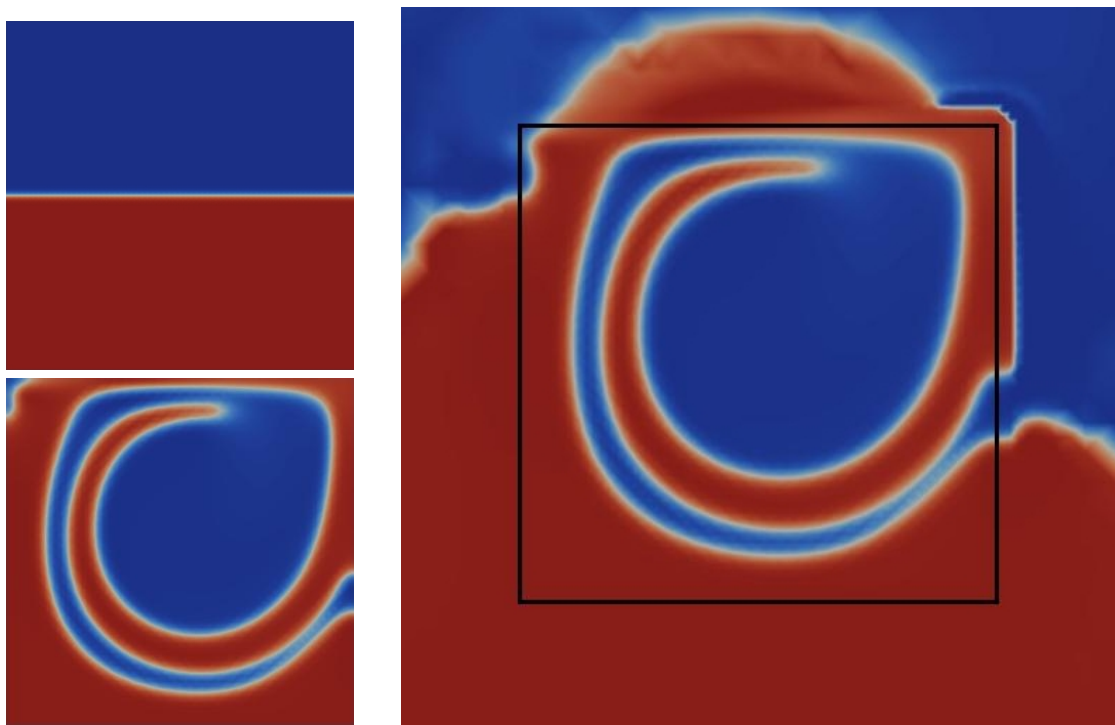

Figure 4.1: Flow in a driven cavity. Initial condition (top left) and solution on the physical domain (bottom left) and a diffuse domain (right). The black rectangle marks the position of the physical boundary modeled by $\phi = 1/2$. Color online.

4.4.2 Y-shaped channel

We next consider a drop flowing through a Y-shaped channel. See Figure 4.3, the channel has inlet diameter 0.5. The outlet branches have a smaller diameter 0.354. At the inflow boundary (left), we prescribe a parabolic velocity profile. The maximum velocity is 4.0. An analogous profile, oriented in the $(1, 1)$ and $(1, -1)$ directions for the upper and lower branches, is specified for the two outflow conditions at the two branches.
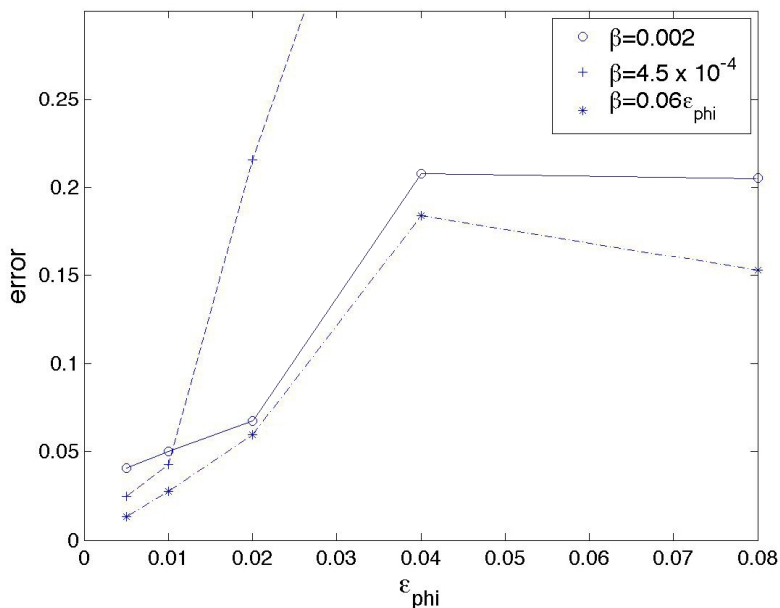
Figure 4.2: L^2 error for different values of boundary layer thickness ϵ_ϕ between the NSCH solution in the physical domain and the DDNSCH solution in the extended domain for the flow in a driven cavity from Figure 4.1, with $\epsilon = 0.01$ fixed.

We place the droplet of diameter 0.36 with center slightly below the middle of the channel. On the walls of the channel, we impose the non-wetting boundary condition $\theta = 180^o$. The channel is embedded in an extended domain $\tilde{\Omega} = [0,1]^2$. The region $\phi < 0.5$ is colored black. The viscosity is $\nu = 0.1$, the surface tension is $\tilde{\sigma} = 1.0$, the mobility is $\gamma = 20.0$ and the interface thickness is $\epsilon_\phi = \epsilon = 0.01$.

Figure 4.3 shows the flow field and the movement of the droplet. As the droplet flows through the channel, it is deformed by the Y-junction and elongates to fit through the lower branch. Figure 4.4 shows the same simulation but with a contact angle $\theta = 90^o$. The droplet now adheres to the wall at the Y-junction and splits into two, roughly hemispherical parts that then exit each branch of the channel. Increasing the surface tension $\tilde{\sigma} = 10.0$, still keeping the contact angle $\theta = 90^o$, changes the evolution as seen in Figure 4.5. Now after adhering to the wall, the droplet remains intact and exits the channel through the lower branch.

4.4.3 Sliding droplets

We next consider a droplet sliding down a structured surface first in 2D and then in 3D. Such a geometry is appropriate for applications in micro- and nano- fluidics. Here, the droplet slides down a rippled ramp whose profile is given by the 30° rotation of the graph (x,y), with $y(x) = (1.4 + 0.02\sin(25x))$. The extended domain is $\tilde{\Omega} = [0, 1.4]^2$. The viscosity is $\nu = 0.001$, the gravitational force is $\mathbf{F} = (0, 0, -9.81)$, the surface tension is $\tilde{\sigma} = 0.1$, the mobility is $\gamma = 0.01$ and the interface thickness is $\epsilon_\phi = \epsilon = 0.01$.

The figures 4.6-4.9 show the motion of the droplet with different contact angles between 60° and 150°. The pictures show the contours of the phase-field variable ψ and thus the position of the droplet between $t = 0$ and $t = 2.0$ at equidistant time intervals. The region $\{\phi < 0.5\}$ is marked black. Note
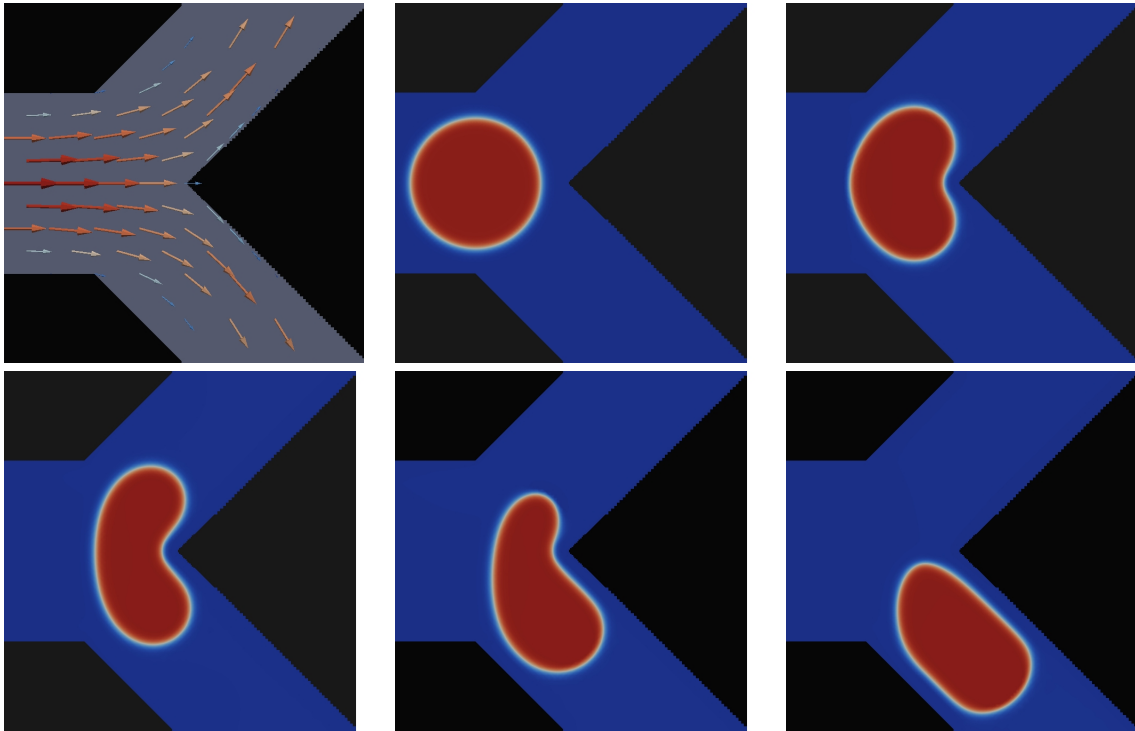
Figure 4.3: Flow field in the channel (top left) and snapshots of a droplet with contact angle 180° flowing through it at times $t = 0$, 0.2, 0.4, 0.6, and 0.8. The area $\{\phi < 0.5\}$ is colored black. Color online.
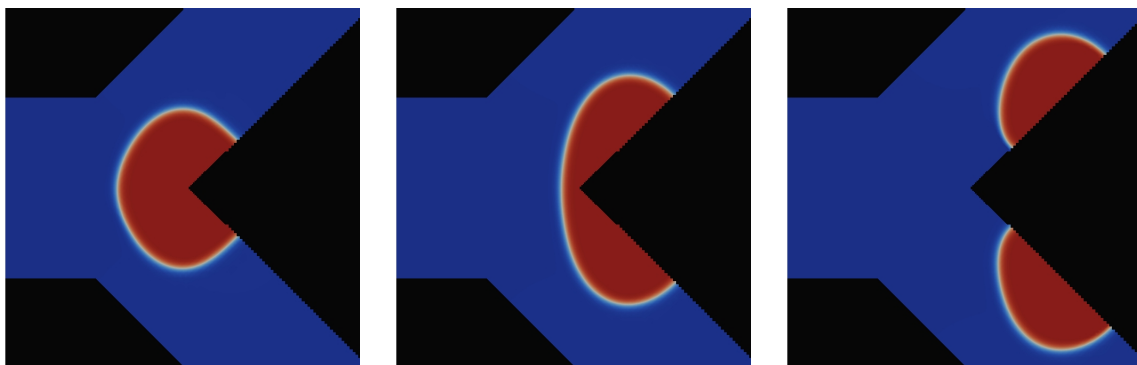
Figure 4.4: The evolution of a droplet flowing through a channel with the same parameters as in Figure 4.3 except with contact angle $\theta = 90^o$ at times $t = 0.3$, 0.6 and 0.9. Color online.

Figure 4.5: The evolution of a droplet flowing through a channel with the same parameters as in Figure 4.4 except with a larger surface tension $\tilde{\sigma} = 10.0$ at times $t = 0.3$, 0.9, and 1.23. Color online.

that there is no significant difference in droplet speed as friction has not been taken into account. In the case of the 60° contact angle the droplet breaks up at early times and a part of it stays in the upper left corner of the ramp while the other part slides down the ramp.
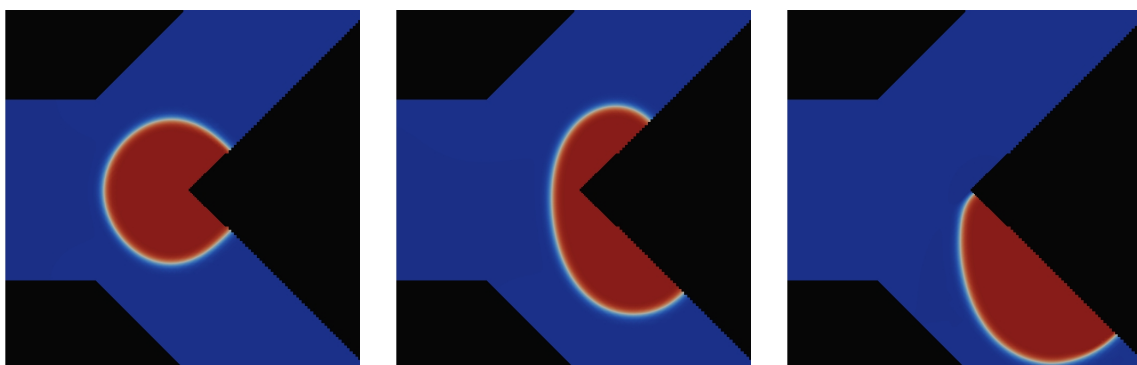
Drop break-up does not occur for the 90°, 120° and 150° contact angle cases; the complete droplet slides down the ramp as seen in Figures 4.6-4.9. Interestingly when the contact angle is $\theta = 150^o$ the droplet rotates as it slides down the ramp and even lifts off the ramp occasionally.

The volume of the drop can be calculated by $\frac{1}{2} \left(\int \phi \, dx - \int \phi \psi \, dx \right)$. During the simulation the volume of the drop slightly increased from 0.039938 to 0.039979. Thus, the error in drop volume is 0.1%. Because the numerical discretization for ψ is conservative, this small error arises from the use of adaptive mesh refinement which is not strictly conservative.
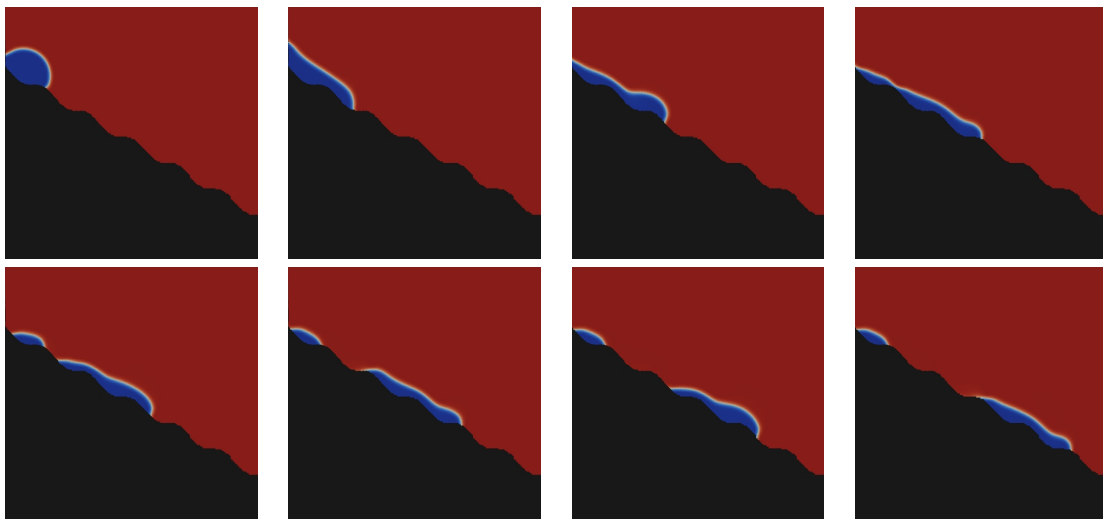
Figure 4.6: Droplet with contact angle of 60° sliding down the ramp. Color online.
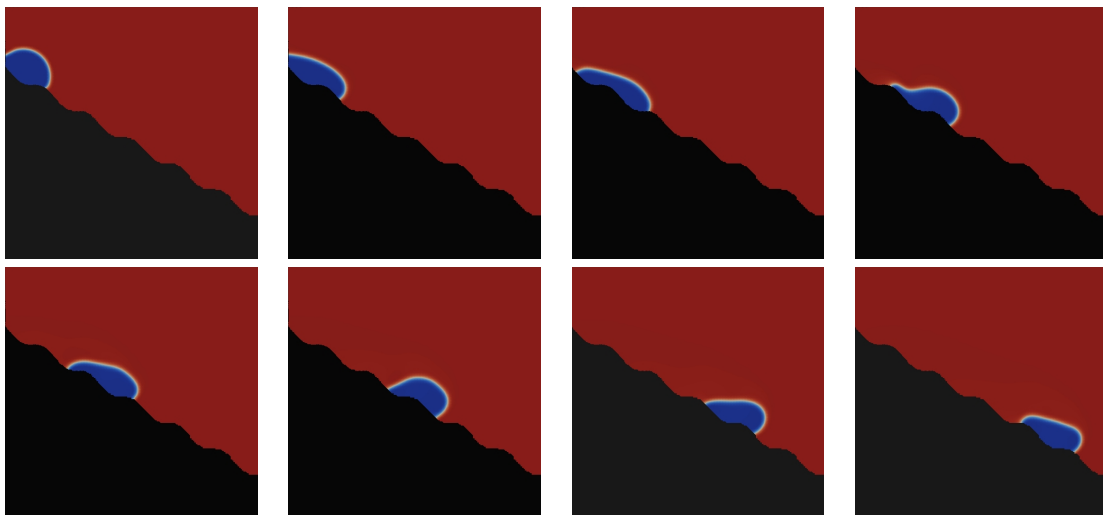
Figure 4.7: Droplet with contact angle of 90° sliding down the ramp. Color online.
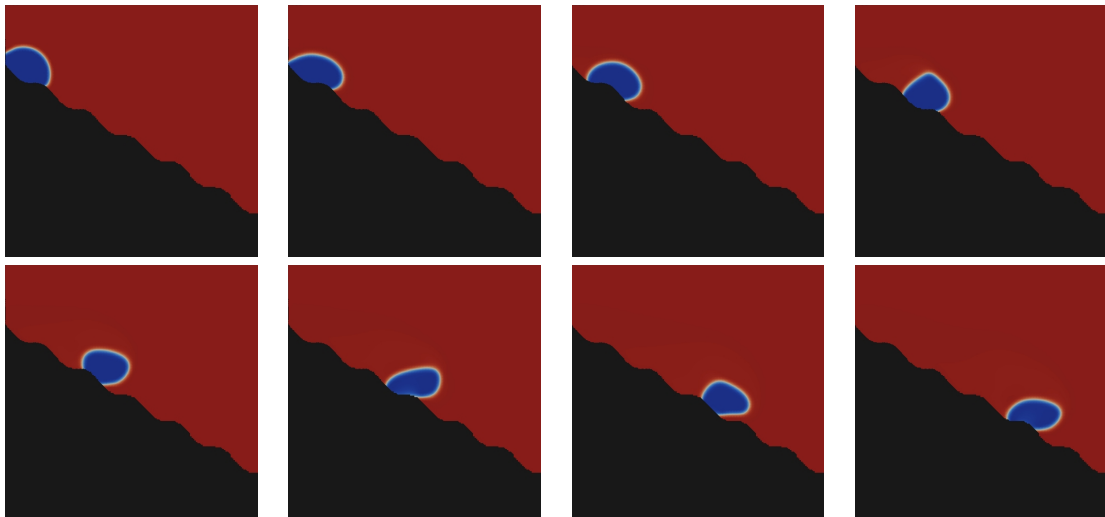
Figure 4.8: Droplet with a contact angle of 120° sliding down the ramp. Color online.
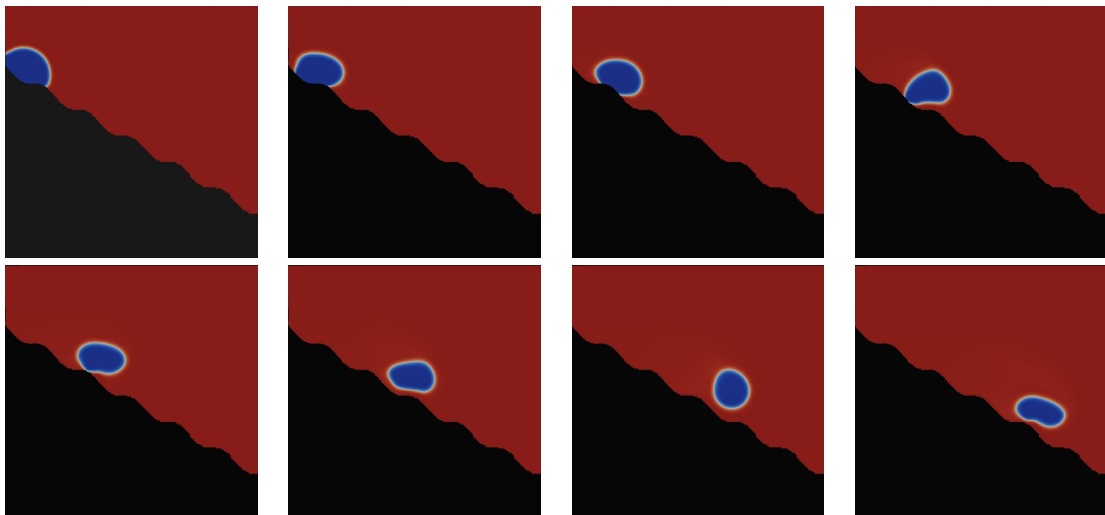
Figure 4.9: Droplet with a contact angle of 150° sliding down the ramp. Color online.
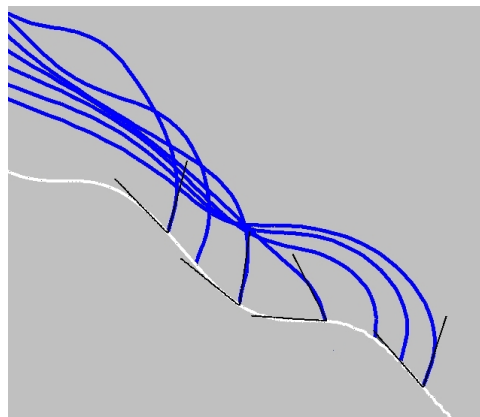
Figure 4.10: Overlay of the leading edge of a droplet (blue), with a 60° contact angle boundary condition, shown together with a local 60° coordinate system (black), at different times as the droplet slides down the ramp (white). Color online.

A close up of the droplets reveals that the contact angles for the simulated drops are very nearly that prescribed through the boundary condition. In Figure 4.10 a droplet with a 60° contact angle boundary condition is shown together with the local coordinate system at the leading tip (showing a 60° angle) as the droplet slides down the ramp. Clearly the error in contact angle is quite small with the largest deviations occurring where the slope of the ramp is the largest and thus the droplet is sliding the fastest (middle of image).

We now consider the same problem in 3D. Figure 4.11 shows a droplet sliding down a structured 45° ramp with a 90° contact angle. The other parameters are as in 2D except that the mobility is $\gamma = 1.0$. In addition, we used a larger interface thickness $\epsilon_\phi = 0.04$ for ϕ than for ψ ($\epsilon = 0.01$) in order to reduce the number of mesh elements. The droplet remains intact and thickens at the leading edge as it slides down the ramp. Interestingly, the trailing edge of the droplet acquires a rather sharp wedge-like shape.
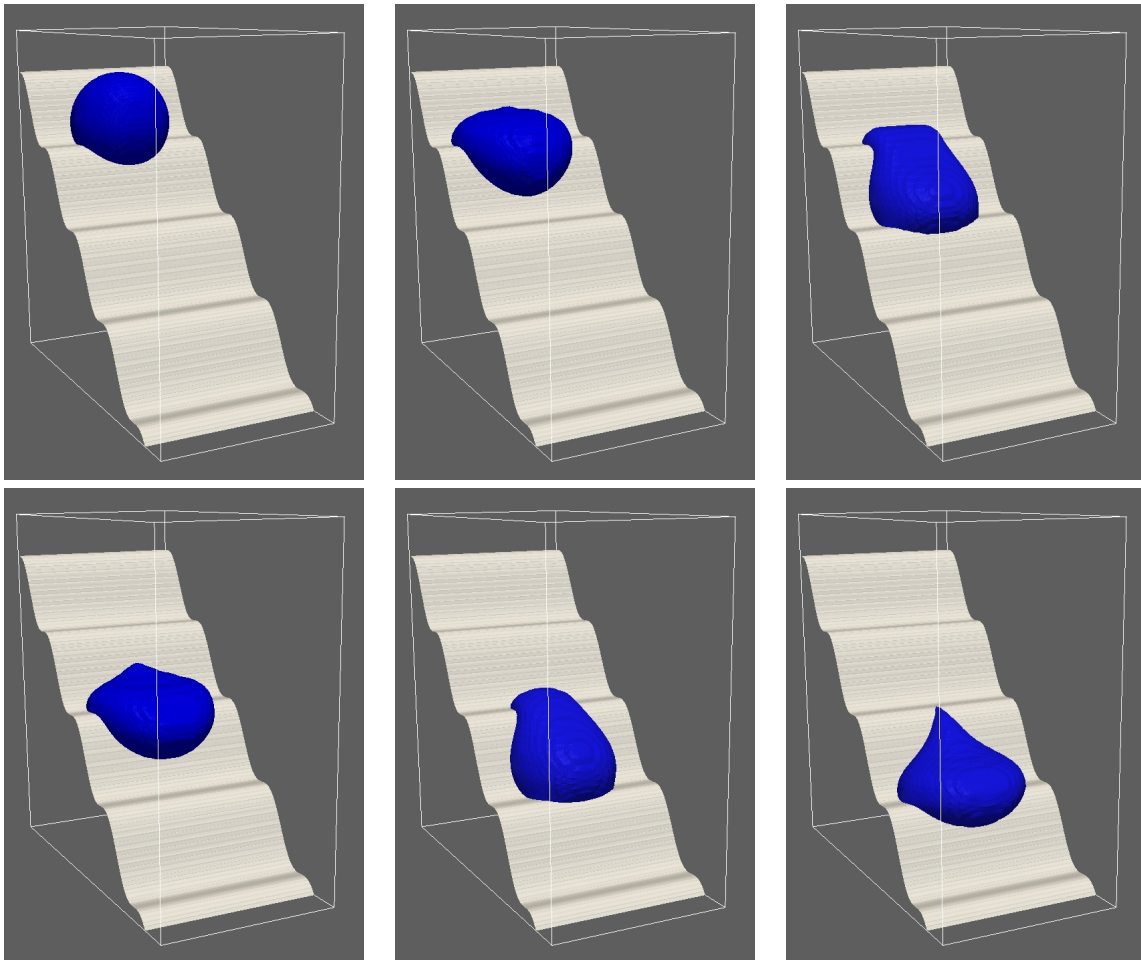
Figure 4.11: Sliding droplet with a 90° contact angle in 3D at times $t = 0$, 0.3, 0.62,0.95, 1.21, 1.42.

4.4.4 Moving domains

In the next example, we simulate a solid ball impacting a liquid/liquid interface in 2D. An axisymmetric version of this problem was previously simulated by [DQA09] who investigated the effect of different

wetting angles on the evolution using a NSCH model with adaptive, boundary-fitted finite elements. Here, we use the diffuse domain formulation with extended domain $\tilde{\Omega} = [0,1] \times [0,1.2]$. As initial condition ϕ is set at zero inside a circle of radius 0.15 which describes the solid ball. The function ϕ smoothly tends to one across the boundary of the ball. The diffuse domain moves with a constant velocity $\mathbf{g} = (0,-1)$. The viscosity is $\nu = 0.01$, the gravitational force is $\mathbf{F} = (0,-9.81)$, the surface tension is $\tilde{\sigma} = 0.1$, the mobility is $\gamma = 10$ and the interface thickness is $\epsilon_\phi = \epsilon = 0.01$. A 90° contact angle boundary condition is imposed. Figure 4.12 shows the results of the simulations. As the ball impacts the interface, a moving contact line forms on each side of the ball that leads to a narrow thread of upper fluid being pulled down into the lower fluid. Eventually the two contact lines merge, the ball separates from the interface and the fluids rebound upward as the ball falls through the lower fluid.
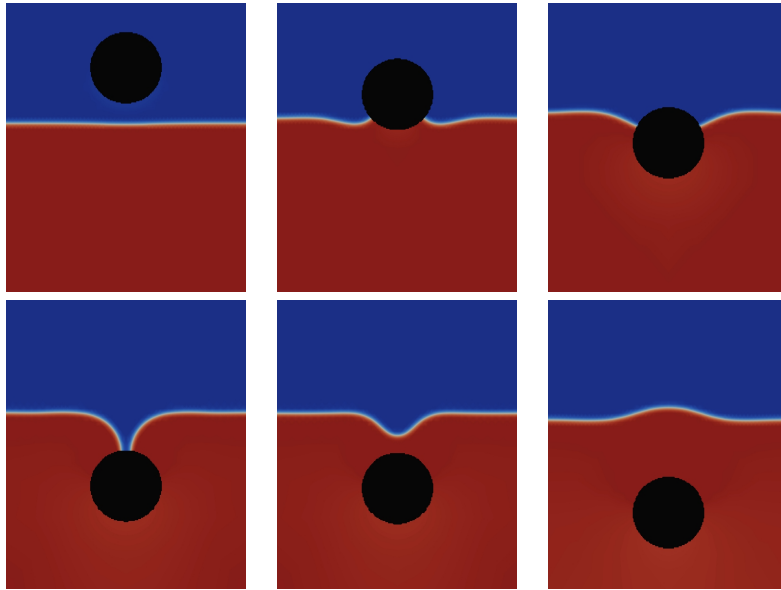
Figure 4.12: The impact of a solid ball into a liquid-liquid interface in 2D. The ball modeled, by the diffuse domain $\phi < 0.5$, is colored black. The snapshots are taken at times $t = 0, 0.1, 0.3, 0.49, 0.51, 0.61$. Color online.

4.4.5 Serpentine channel

As a final example, we use the DDNSCH model to simulate mixing inside a 2D droplet by chaotic advection which is induced by having the droplet flow through a winding, serpentine channel with thickness comparable to that of the droplet. [MS05] simulated this process by using a finite-volume/front tracking method and discretizing the equations in the complex geometry using a curvilinear grid, and visualizing the mixing using a particle tracking method. Here, we consider a similar configuration using the DDNSCH model, although we use a continuous field to assess the mixing.

The channel geometry is given by two sine functions with period length 0.2π and amplitude 0.2. The vertical distance between the upper and lower channel boundaries is 0.25 and the channel domain is embedded in the extended domain $\tilde{\Omega} = [-0.2, 2.2] \times [0, 0.8]$. Initially, a droplet of diameter 0.16 is placed at the upper left corner of the channel. See Figures 4.13 and 4.14.

Furthermore an additional variable e is used to indicate the concentration of a tracer material within the droplet. Consequently, e satisfies a convection-diffusion equation within the moving and deforming droplet:

$$\partial_t e + \nabla \cdot (\mathbf{u}e) - D\Delta e = 0 \quad \text{on } \{\psi < 0\}$$

where the diffusion parameter D is chosen to be very small, e.g. 10^{-8}, so that molecular diffusion is small and mixing is primarily due to chaotic advection. Following [LLRV09], this equation is reformulated using the diffuse domain approach as

$$\partial_t \left(\tilde{\psi}e \right) + \nabla \cdot \left(\tilde{\psi}\mathbf{u}e \right) - D\nabla \cdot (\tilde{\psi}\nabla e) = 0 \quad \text{on } \tilde{\Omega},$$

where

$$\tilde{\psi} = \frac{1}{2}(1 - \psi)$$

approximates the characteristic function of the droplet interior.

In figures, 4.13-4.14 the viscosity of the fluids is $\nu = 0.01$, the surface tension is $\tilde{\sigma} = 1.0$, the mobility $\gamma = 0.1$ and the interface thickness is $\epsilon_\phi = \epsilon = 0.01$. Further, we added a non-wetting condition by incorporating a penalty formulation in the free energy functional (last term):

$$F(\psi) = \int_\Omega \left[\frac{1}{4} \left(\psi^2 - 1 \right)^2 + \frac{\epsilon^2}{2} |\nabla \psi|^2 \right] dx + \int_\Gamma \frac{1}{2}(\psi - 1)^2 dx.$$

The corresponding functional derivative results in an additional term in the Cahn-Hilliard equation, which can be incorporated into (4.4) by setting [LLRV09]

$$BC_\psi = (\psi - 1)|\nabla \phi|.$$

Finally, we equip the model with a no-slip Dirichlet boundary condition $\mathbf{u} = \mathbf{0}$ on the upper and lower boundaries of the channel. At the inflow (left) and outflow (right) boundary we use a parabolic velocity profile with maximum speed $\mathbf{u} = (1, 0)$. The resulting flow field through the channel in the absence of the droplet is shown in figure 4.13.

Figure 4.14 shows snapshots of the evolving droplets and mixing patterns at times $t = 0.02, 0.22, 0.42, 0.62, 0.82, 1.02, 1.22, 1.42$. The droplet starts at the upper left corner and consists initially of tracer material in one half of the droplet (yellow) while the remaining tracer free portion is colored blue. The adaptive grid shown figure 4.14 makes it possible to identify the position of the channel as seen by the refinement along its boundary. Note that the grid is taken from time $t = 0.02$.

As the droplet flows through the channel, it deforms to an elongated shape it moves downwards and upwards through the straight regions. At the peaks and valleys where the flow changes from downward to upward (and vice versa) and the channel is wider, the surface tension brings the drop back to a more circular shape. Throughout this process, the velocity fields result in significant mixing within the droplet as indicated by the increasingly uniform distribution of green coloring.
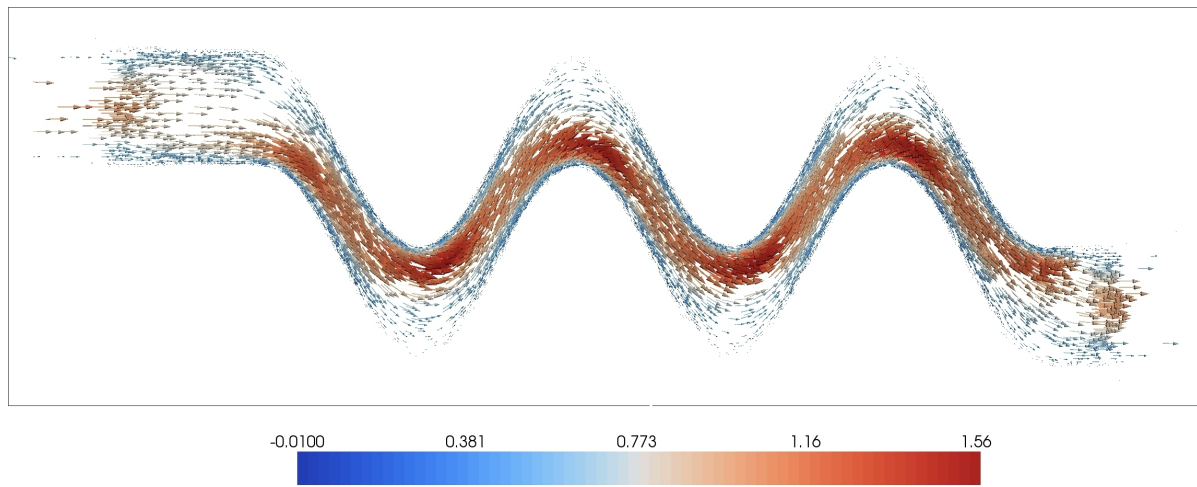
Figure 4.13: Flow field in a winding, serpentine channel shown on the extended domain $\tilde{\Omega}$. See text for details. Color online.
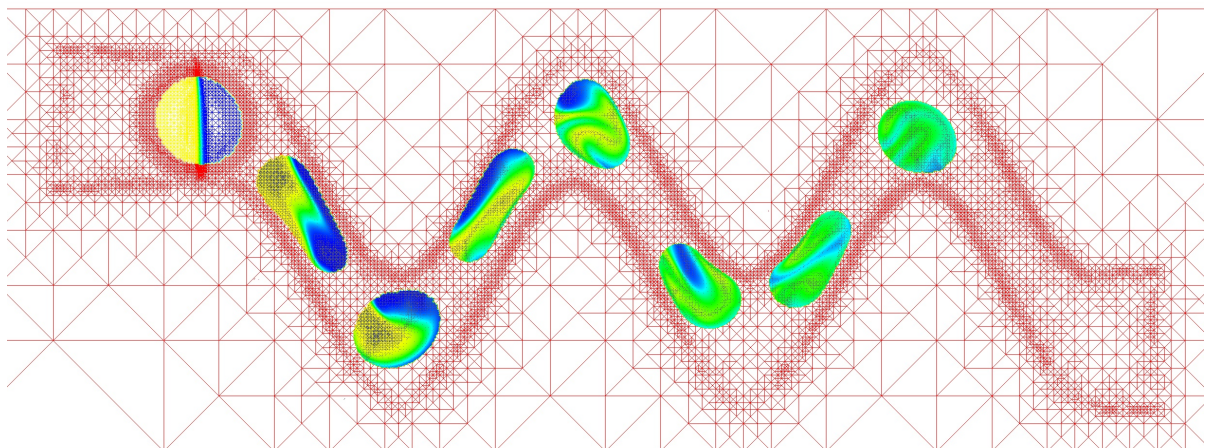

Figure 4.14: Snapshots of the droplet evolution and interior mixing patterns over time. See text for details. Color online.

4.5   Conclusions and future work

We have extended previous work and presented a diffuse domain approach to simulate two-phase flows in complex geometries. A concentration field was introduced to describe the distribution of one of the fluid phases. The concentration field is coupled to the Navier-Stokes equations for the fluid motion through extra stresses that mimic surface tension and is evolved by an advective Cahn-Hilliard equation that is equipped with boundary conditions that encode contact line information (e.g. equilibrium contact angle). The diffuse interface formulation circumvents mesh generation of complex geometries by embedding the complex domain in a larger, regular domain and reformulating the equations using a a phase-field function that approximates the characteristic function of the complex domain. This is particularly useful in 3D where the development of a high-quality meshes in a complex geometry is a nontrivial problem. The resulting diffuse domain equations on the regular domain were solved by a finite element method although any standard discretization method could be applied. Adaptive mesh refinement was needed to efficiently resolve the transition layers associated with the concentration and phase field variables. We demonstrated the applicability of the diffuse domain approach by solving several typical two-phase flow problems from micro- and nano- fluidics in both stationary and moving domains.

While the domains we considered were idealized, any other profiles could be used including those obtained from experimental images and micrographs. For example, in Figure 4.15, the flow over a realistic thin film taken from an AFM image [KUGS08] is shown. The Navier-Stokes equations are solved in the blue region above the thin film with a velocity $\mathbf{u} = (0.01m/s, 0, 0)$ imposed at the upper boundary, no-slip conditions $\mathbf{u} = \mathbf{0}$ imposed on the film surface and periodic conditions are used in the x and y directions. The compu-

Figure 4.15: AFM image of a thin film grown by electrodeposition, with simulated flow field in a boundary layer of electrolyte. AFM data from [KUGS08]. Color online.

tational domain is $[0, 2 \times 10^{-6}] \times [0, 2 \times 10^{-6}] \times [0, 8 \times 10^{-7}]m^3$. The thickness of the fluid layer is approximately 4×10^{-7} and $\epsilon_\phi = 2 \times 10^{-8}$. The density and viscosity of the liquid correspond to that of water; the effect of gravity is not considered. The results reveal that flow near the valleys of the film is suppressed and the fluid is nearly stagnant. This is a first step towards microscopically simulating the effect of flow on electrodeposition and the possibility of controlling the deposition process using magnetic fields, e.g. see [KUGS08].

An interesting open question is the sharp interface limit of the diffuse domain formulation. For problems without three-phase contact lines, the diffuse domain models converge to classical sharp interface models as the sharp interface thickness tends to zero. However, when a three-phase contact line is present, the classical sharp interface model is singular and the diffuse interface model is thus

a singular perturbation. The transition layers for ψ and ϕ may strongly interact yielding non-uniform convergence in interface thickness. Nevertheless, when the boundary layer thickness ϵ_ϕ tends to zero, we found convergence of the diffuse domain solution to the solution of the equations and boundary conditions in the original domain, for fixed interface thickness ϵ. However, if the concentration and phase field functions have the same transition layer thickness $\epsilon = \epsilon_\phi$, then further characterization is needed to identify the sharp interface limit $\epsilon \to 0$.

In the models presented here, the interaction between the fluid and the solid boundary was limited to no-slip and contact angle boundary conditions. Further, the motion of the solid was specified. In numerous applications, however, the motion of the solid and fluid are intimately coupled through hydrodynamic forces (e.g., solid particles moving in a flow). In addition, the solid may deform. In these cases, additional equations need to be solved to determine the evolution of the coupled system. For example, when the solid is rigid, the Newton-Euler equations need to be solved for the linear and angular particle velocities. When the solid is deformable, the elasticity equations need to be solved in the solid structure together with continuity of velocity and normal stress boundary conditions at the solid/liquid interface. Thus, a natural extension of this work is the development of a diffuse domain formulation for such fluid structure interactions. This is currently under development.

Chapter 5

A continuum model of colloid-stabilized interfaces

5.1 Introduction

Colloidal particles that are partially wetted by two immiscible fluids tend to adsorb at the interface be-
tween the fluids to minimize the overall free energy of the system. As the colloid density at an interface
increases, e.g. through adsorption of colloids or through a reduction in interface area, the colloids may
crowd and become immobilized forming a jammed colloidal monolayer. The crystallized interface
can be solid-like with mechanical rigidity. This ability to impart rigidity and surface elasticity is an
important difference between surface colloid and surfactant systems. In particular, unlike surfactants,
colloid jamming can lead interfaces with unusual shapes, such as nonspherical bubbles[SAMS05], and
unusual fluid configurations such as stabilized (Pickering) emulsions[Pic07, ZBD06, LCS08, Cle08,
Dic10] and bicontinuous morphologies[Cle08, CC08]. Stable bicontinuous morphologies in which
interpenetrating, continuous domains of two immiscible fluids are maintained in a rigid state by a
jammed layer of colloidal particles at their interface were discovered several years ago by Chung et
al.[COFC05] experimentally for thin films of polymeric fluids and by Stratford et al.[SAP$^+$05] numer-
ically for viscous fluids. Stratford et al. referred to such configurations as bicontinuous interfacially
jammed emulsion gels or bijels and proposed that bijels form a new class of soft materials with po-
tentially remarkable properties with elastic moduli and yield stress tunable over a very wide range.
Such structures have wide variety of potential applications including barrier materials[Ulb06], solar
cells[MYG$^+$05], food systems[Dic10], crossflow microreactors[SAP$^+$05] and as template scaffolds
for colloidal gels[SWCC09]. Experiments recently performed by Herzig et al.[HWS$^+$07] have demon-
strated the ability to produce three dimensional bijels using viscous fluids that are stable for several
months. Bijels have also been recently produced using biopolymers[FMD09].

When an interface is crystallized with colloid particles, a decrease in interface area would force the
colloids to desorb. However, the desorption energy is typically much larger than the thermal energy,
and thus the adsorption process of the colloids at the interface is practically irreversible since desorption

would increase the energy. On the other hand, an increase in interfacial area also leads to an overall increase in energy as the interface becomes more exposed by reducing the surface colloid fraction. Because the surface tension is the variation of the free energy with respect to interfacial area, this suggests that surface colloids are better described using an interfacial elasticity model rather than a surface tension model, which is more suitable for surfactants. See for example Refs.[CHS$^+$08, Cle08].

As we have seen in Sec. 2.7 elastic particle interactions are intrinsically included in the PFC model, which allows to describe the interfacial particles by a restriction of the PFC model to the interface. Contrary to the Lattice Boltzmann methods that are usually used to model bijels, this allows to average out the vibrational modes of the particles and to model particle-particle interactions on diffusive time scales. In this chapter we present such an approach, where we combine a classical Navier-Stokes-Cahn-Hilliard equation to model the two-phase flow system, with a surface phase field crystal model for the colloidal particle interactions. The resulting Navier-Stokes-Cahn-Hilliard-Surface-Phase-Field-Crystal (NSCHSPFC) model introduces a new elastic force resulting from the colloidal particle interactions. This force acts in addition to the interfacial tension on the fluid-fluid interface. The approach thus differs from the modeling in [JH11], in which the colloidal particles only affect the interfacial tension.

Additionally, a model for attachment of colloids to the interface is derived, and a concentration equation for a colloidal density in one fluid phase is used with attachment/detachment boundary conditions along the fluid-fluid interface. These surface and bulk equations are reformulated using the diffuse interface and diffuse domain approaches introduced in Refs.[RV06, LLRV09, TLL$^+$09] for solving partial differential equations on surfaces and complex domains and coupling surface and bulk problems. The governing equations, and extra stresses, are derived using an energy variation approach accounting for surface energy, modeled by a Cahn-Hilliard-type energy[CH58], and the energy associated with surface colloids from the surface PFC model. To confirm the results also a sharp interface model is derived. Using the tools in [RV06] formal matched asymptotics show convergence of the previous diffuse interface models to the derived sharp interface approach. Using a variety of flow configurations in two and three dimensions, we demonstrate that as colloids jam on the interface and the interface crystallizes, the elastic force may be strong enough to make the interface sufficiently rigid to resist external forces, such as an applied shear flow, as well as surface tension induced coarsening in bicontinuous structures. Finally, we demonstrate the solid-like properties of the new material, by considering a rigid body falling within a particle-stabilized gel. Combined with classical models for surfactants, which only influence the interfacial tension, see e.g. [TSLV10], the NSCHSPFC approach can also be used to model more recent experimental investigations on the influence of surfactants on particle-stabilized gels [TSC11].

The chapter is organized as follows. In Sec. 5.2 we derive the model using an energy variation argument. In Sec. 5.3 the numerical method is briefly described, and in Sec. 5.4 we show first simulation results. It is seen that the force coming from the elastic particle interactions leads to spurious velocities, which gives rise to introducing a regularization of the elastic force. In Sec. 5.5 a regularized elastic force is derived by averaging the elastic force over a vanishingly small control volume. In Sec. 5.6, a new, variational NSCHSPFC model is derived using a new approximation of the surface delta function. In Sec. 5.7, a new sharp interface model is derived and the new variational model is shown to be a diffuse interface approximation of the sharp interface system. Finally, numerical simulations with

the regularized diffuse interface model are presented in 5.8.

5.2 Mathematical Model

5.2.1 Model derivation

In this section, we derive the governing equations using an energy variation approach. To do this we need to define the total free energy of the system. As we have seen in Sec. 2.7 the PFC energy can be used to model elastic particle interactions in bulk systems. Here, we want to consider interfacial colloid particles, which requires to localize the PFC energy on a surface Γ. To describe the position of the fluid-fluid interface Γ, and of the two fluid phases, we use a phase field variable ψ such that $\psi = 0$ and 1 denote the fluid phases and $\psi = 0.5$ denotes the interface location: $\Gamma(t) = \{\mathbf{x} \in \Omega : \psi(\mathbf{x}, t) = 0.5\}$, with $\Omega \subset \mathbb{R}^{2,3}$. For example, one may take

$$\psi(\mathbf{x}, t) = \frac{1}{2} \left[1 - \tanh\left(\frac{d(\mathbf{x}, t)}{\sqrt{2}\epsilon} \right) \right] \tag{5.1}$$

where ϵ determines the interface thickness and $d(\mathbf{x}, t)$ denotes the signed distance function from the fluid-fluid interface to $\mathbf{x}$ at time t. As we have seen in Sec. 2.2 the function

$$B(\psi) = \psi^2(1 - \psi)^2, \tag{5.2}$$

when scaled by $6\sqrt{2}/\epsilon$, approximates the surface delta function δ_Γ:

$$\frac{6\sqrt{2}}{\epsilon} B(\psi) \approx \delta_\Gamma. \tag{5.3}$$

Now, we can use the diffuse interface approach [RV06, TLL$^+$09] to restrict the PFC energy to the surface (see Sec. 2.5). The surface phase field crystal (SPFC) energy, can then be written as

$$E_{SPFC} = \frac{\lambda}{\epsilon} \int B(\psi) f_{SH}(\varrho) \, dx, \tag{5.4}$$

where λ is an elastic energy coefficient and the Swift-Hohenberg energy density f_{SH} is given by

$$f_{SH}(\varrho) = \frac{\varrho^2}{2} \left(a + \tilde{\beta}q_0^4 \right) + \frac{g}{4}\varrho^4 - \tilde{\beta}q_0^2|\nabla\varrho|^2 + \frac{\tilde{\beta}}{2} \left(\frac{1}{B(\psi)} \nabla \cdot (B(\psi)\nabla\varrho) \right)^2. \tag{5.5}$$

See also Sec. 2.7 where the original PFC energy is stated. Note that the last term in Eq. 5.5 approximates $\frac{\tilde{\beta}}{2} \left(\Delta_\Gamma \varrho \right)^2$ according to Sec.2.3.2.

We now suppose that the total energy of the system consists of the SPFC energy, the surface energy E_σ and the kinetic energy E_{kin}:

$$E \quad = \quad E_{spfc} + E_\sigma + E_{kin}, \tag{5.6}$$

where the dimensional surface energy is approximated by the Cahn-Hilliard energy

$$E_\sigma = \tilde\sigma \int \frac{1}{\epsilon} \left(B(\psi) + \epsilon^2 |\nabla\psi|^2 \right) \, dx \tag{5.7}$$

and the kinetic energy is given by

$$E_{kin} = \frac{\bar\rho}{2} \int |\mathbf{u}|^2 \, dx \tag{5.8}$$

where $\bar\rho$ is the constant density of the fluid, and $\tilde\sigma$ is the scaled surface tension coefficient according to Sec. 2.6.2.

To reduce the number of parameters we will now nondimensionalize these energies. Introducing characteristic scales for space L (e.g., characteristic drop radius) and velocity $U = \sqrt{\sigma/(\bar\rho L)}$ (e.g. the characteristic surface tension velocity), we define the nondimensional quantities denoted by tildes:

$$\tilde{\mathbf{x}} = \mathbf{x}/L, \ \tilde t = tU/L, \ \tilde{\mathbf{u}} = \mathbf{u}/U, \ \tilde E = E/(\bar\rho U^2 L^3), \tag{5.9}$$

and

$$r = a/(\tilde\beta q_0^4), \ \tilde\epsilon = \epsilon/L, \ \delta = 1/(Lq_0). \tag{5.10}$$

Note that δ describes the ratio of the characteristic length scales of the fluid system to the colloid system. Now, we get the nondimensional energies

$$\tilde E_{kin} = \frac{1}{2} \int |\tilde{\mathbf{u}}|^2 \, d\tilde x, \ \ \tilde E_\sigma = \frac{1}{\tilde\epsilon} \int B(\psi) + \tilde\epsilon^2 |\tilde\nabla\psi| \, d\tilde x. \tag{5.11}$$

Taking $\rho = \sqrt{\dfrac{g}{\beta q_0^4}} \varrho$ (e.g. see also Sec. 2.7), the nondimensional SPFC energy becomes

$$\tilde E_{spfc} = \frac{El^{-1}}{\tilde\epsilon} \int B(\psi) f(\rho, \tilde\nabla\rho, \nu) \, d\tilde x, \tag{5.12}$$

where $El = \dfrac{\bar\rho U^2 L}{\lambda} \cdot \dfrac{g}{\beta^2 q_0^8} = \dfrac{\tilde\sigma}{\lambda} \cdot \dfrac{g}{\beta q_0^8}$ is an elasticity number that measures the strength of the SPFC energy relative to the surface energy, and

$$f(\rho, \tilde\nabla\rho, \nu) = \frac{1}{4}\rho^4 + \frac{1+r}{2}\rho^2 - \delta^2|\tilde\nabla\rho|^2 + \frac{\delta^4}{2}\nu^2, \tag{5.13}$$

$$\nu = \frac{1}{B}\tilde\nabla \cdot (B\tilde\nabla\rho). \tag{5.14}$$

Now, the total energy to be considered is

$$\tilde E = \tilde E_{kin} + \tilde E_{spfc} + \tilde E_\sigma \tag{5.15}$$

In the following we will only consider the nondimensional variables which allows us to drop the tildes.

We now derive the equations for the two-phase system with colloidal particles starting with an energy variation argument. We take the time derivative of the energy E, which is equivalent to varying ψ and ρ simultaneously. This gives

$$\dot{E} \quad = \quad \int_\Omega \mathbf{u}\dot{\mathbf{u}} + \dot{\psi}\frac{\delta E}{\delta \psi} + \dot{\rho}B\frac{\delta E}{\delta \rho} \; dx \tag{5.16}$$

where the overdot denotes the time derivative and

$$\frac{\delta E}{\delta \psi} \quad := \quad \frac{El^{-1}}{\epsilon}B'\left(f - \delta^4\nabla\nu\cdot\nabla\rho - \delta^4\nu^2\right) + \frac{1}{\epsilon}\left(B' - \epsilon^2\Delta\psi\right) \tag{5.17}$$

$$\frac{\delta E}{\delta \rho} \quad := \quad \frac{El^{-1}}{\epsilon}\left(\rho^3 + (1+r)\rho + 2\delta^2\nu + \frac{\delta^4}{B}\nabla\cdot(B\nabla\nu)\right). \tag{5.18}$$

We suppose the fluid motion is governed by the Navier-Stokes equations which, in the nondimensional variables introduced here, is given by

$$\dot{\mathbf{u}} = -\mathbf{u}\cdot\nabla\mathbf{u} - \nabla p + \frac{1}{Re}\Delta\mathbf{u} + \mathbf{F}, \quad \nabla\cdot\mathbf{u} = 0, \tag{5.19}$$

where p is the pressure and $Re = \bar{\rho}LU/\eta$, with η the viscosity, is the Reynolds number, and the force $\mathbf{F}$ is as yet unspecified. Note that if Re is small, the Stokes equations could be used instead of the Navier-Stokes equations and the analysis below remains valid.

The functions ψ and ρ are assumed to satisfy the conservation equations

$$\dot{\psi} \quad = \quad -\mathbf{u}\cdot\nabla\psi - \nabla\cdot\mathbf{J}_\psi \tag{5.20}$$

$$\frac{\partial}{\partial t}(B(\rho + \tilde{\rho})) \quad = \quad -\nabla\cdot(B(\rho + \tilde{\rho})\mathbf{u}) - \nabla\cdot\mathbf{J}_\rho \tag{5.21}$$

where the fluxes $\mathbf{J}_\rho$ and $\mathbf{J}_\psi$ have also not yet been specified. Note that Eq. (5.21) is the diffuse interface form of the surface mass conservation equation[RV06, TLL$^+$09] where $\rho + \tilde{\rho}$ is conserved on the surface. $\tilde{\rho}$ is a physical constant given by $\tilde{\rho} = \sqrt{g/(\beta q_0^4)}$. In the derivation of the PFC model (Sec. 2.7) it can be seen that the physical colloid density is given by a multiple of $\rho + \tilde{\rho}$, which gives reason to conserve $\rho + \tilde{\rho}$ on the interface.

Using the incompressibility of the fluid and Eq. (5.20), Eq. (5.21) can be rewritten as

$$\dot{\rho} \quad = \quad -\mathbf{u}\cdot\nabla\rho + \frac{B'}{B}(\rho + \tilde{\rho})\nabla\cdot\mathbf{J}_\psi - \frac{1}{B}\nabla\cdot\mathbf{J}_\rho \tag{5.22}$$

Next, we determine $\mathbf{F}$, $\mathbf{J}_\psi$ and $\mathbf{J}_\rho$ to ensure that the energy is nonincreasing in time ensuring thermodynamic consistency. Inserting Eqs. (5.19), (5.20) and (5.22) into Eq. (5.16) and integrating by parts,

the time derivative of the energy becomes

$$
\begin{aligned}
\dot{E} \;=\; & -\frac{1}{Re} \int_{\Omega} \nabla \mathbf{u} : \nabla \mathbf{u} \, dx \\
& + \int \mathbf{u} \cdot \left(\mathbf{F} - \frac{\delta E}{\delta \psi} \nabla \psi - B \frac{\delta E}{\delta \rho} \nabla \rho \right) dx \\
& + \int \mathbf{J}_{\psi} \cdot \nabla \left(\frac{\delta E}{\delta \psi} - B'(\rho + \tilde{\rho}) \frac{\delta E}{\delta \rho} \right) dx \\
& + \int \mathbf{J}_{\rho} \cdot \nabla \frac{\delta E}{\delta \rho} dx.
\end{aligned}
$$

In the above, we have assumed natural (or periodic) boundary conditions and dropped all the boundary terms. By taking

$$
\mathbf{F} \;=\; \frac{\delta E}{\delta \psi} \nabla \psi + B \frac{\delta E}{\delta \rho} \nabla \rho, \tag{5.23}
$$

$$
\mathbf{J}_{\psi} \;=\; -Pe_{\psi}^{-1} \epsilon B \nabla \left(\frac{\delta E}{\delta \psi} - B'(\rho + \tilde{\rho}) \frac{\delta E}{\delta \rho} \right), \tag{5.24}
$$

$$
\mathbf{J}_{\rho} \;=\; -Pe_{\rho}^{-1} B \nabla \frac{\delta E}{\delta \rho}, \tag{5.25}
$$

where Pe_{ψ} and Pe_{ρ} are Peclet numbers, we obtain $\dot{E} \leq 0$.

If the flux $\mathbf{J}_{\psi}$ as defined in Eq. (5.24) is used in the conservation equation (5.20), the resulting ψ does not provide a good description of the interface layer because of the contributions of E_{spfc} to the variational derivatives. In particular, unlike the hyperbolic tangent function in Eq. (5.1), the interface thickness is non-uniform, which can introduce spurious Marangoni-like velocities. Since the primary purpose of ψ is to track the two-phase interface, we simplify $\mathbf{J}_{\psi}$ and omit the terms dependent on E_{spfc}, which gives the standard Cahn-Hilliard flux

$$
\mathbf{J}_{\psi} = -Pe_{\psi}^{-1} \epsilon B \nabla \frac{\delta E_{\sigma}}{\delta \psi} = -Pe_{\psi}^{-1} B \nabla \left(B' - \epsilon^2 \Delta \psi \right). \tag{5.26}
$$

Although the resulting system is no longer variational and does not necessarily decrease the energy, this effect tends to be higher order since away from the interface $B(\psi) \approx 0$ and near the interface ψ locally equilibrates yielding $B'(\psi) - \epsilon^2 \Delta \psi \approx 0$. Note that if $\mathbf{J}_{\psi} \approx 0$, then $\dot{E} \leq 0$ with $\mathbf{F}$ and $\mathbf{J}_{\rho}$ given in Eqs. (5.23) and (5.25).

Using Eqs. (5.17) and (5.18), the force $\mathbf{F}$ in the Navier-Stokes equation can be written as

$$
\begin{aligned}
\mathbf{F} \;=\; & \frac{El^{-1}}{\epsilon} B' \nabla \psi (f - \nabla \nu \cdot \nabla \rho - \nu^2) + B \frac{\delta E}{\delta \rho} \nabla \rho + \frac{\delta E_{\sigma}}{\delta \psi} \nabla \psi \tag{5.27} \\
\;=\; & \frac{El^{-1}}{\epsilon} \nabla \left(B \left(f - \delta^4 \nabla \nu \cdot \nabla \rho - \delta^4 \nu^2 \right) \right) + \bar{\mathbf{F}}, \tag{5.28}
\end{aligned}
$$

where

$$
\bar{\mathbf{F}} = -\frac{El^{-1}}{\epsilon} B \nabla (f - \delta^4 \nabla \nu \cdot \nabla \rho - \delta^4 \nu^2) + B \frac{\delta E}{\delta \rho} \nabla \rho + \frac{\delta E_{\sigma}}{\delta \psi} \nabla \psi. \tag{5.29}
$$

We refer to the first two terms of $\bar{\mathbf{F}}$ as the elastic force and to the last term as the surface tension, or capillary, force. Note that if $\rho \approx \text{constant}$, so that the colloids are in the disordered or liquid state, then the elastic force is nearly zero. Further, Eq. (5.29) suggests that in equilibrium the interface experiences colloid-induced elastic stress just as it does capillary stress.

In the Navier-Stokes equations (5.19) we may use the force $\bar{\mathbf{F}}$ rather than $\mathbf{F}$ by introducing a new pressure $\bar{p}$ as

$$\bar{p} := p - \frac{El^{-1}}{\epsilon} B(f - \delta^4 \nabla\nu \cdot \nabla\rho - \delta^4 \nu^2).$$

Numerically, we find that using $\bar{\mathbf{F}}$ yields a more accurate solution than using $\mathbf{F}$.

5.2.2 Attachment of Colloids

We next consider the attachment of colloids to the interface with the idea of using attachment to drive the colloid density on the interface into the crystal part of the PFC phase diagram to induce colloid jamming and interface crystallization. Here, we do this by introducing a nondimensional colloid density in the bulk, c, which satisfies a convection-diffusion equation with a flux boundary condition at the interface that describes colloid attachment and detachment. We note that there are many other ways this could be done. For example, the bulk PFC equation (recall Sec. 5.2.1) could be used instead. However, since we are most interested in the case in which the colloids only crystallize at the interface, and not in the bulk fluid regions, the advection-diffusion equation is likely sufficient.

Here, we present the equations in nondimensional form and use the diffuse interface framework developed in Ref.[TSLV10]. For simplicity, we assume that the colloids are soluble only in the fluid phase $\psi \equiv 1$. This leads to the convection-diffusion equation:

$$\partial_t(\psi c) + \nabla \cdot (\psi \mathbf{u} c) = Pe_c^{-1} \nabla \cdot (\psi \nabla c) - hj|\nabla\psi|, \tag{5.30}$$

where Pe_c is a Peclet number, h is the penetration depth and j is the net flux of colloids to the interface. Note that $|\nabla\psi| \approx \delta_\Gamma$, the surface delta function. The net flux j must also be accounted for in the evolution of the surface colloid density ρ through the addition of a source. Therefore, Eq. (5.22) is modified accordingly as

$$\dot{\rho} = -\mathbf{u} \cdot \nabla\rho + \frac{B'}{B}\rho\nabla \cdot \mathbf{J}_\psi - \frac{1}{B}\nabla \cdot \mathbf{J}_\rho + j. \tag{5.31}$$

There are numerous ways of defining the source term j. In general it is not clear how to couple the macroscopic density c with the microscopic density ρ. The usual way of defining the net flux for macroscopic quantities is to use the constitutive assumption

$$j := Bi\left(c(\rho_\infty - \rho) - k^{-1}\rho\right), \tag{5.32}$$

where Bi is a Biot number that measures the adsorption rate relative to the surface tension time scale τ_σ and k^{-1} measures the relative rates of desorption and adsorption. The density ρ_∞ is a saturation constant that is in the crystal phase of the phase diagram of the PFC. The use of Eq. (5.32) may

introduce difficulties, however, when ρ is in the crystal phase of the PFC. In this case, ρ oscillates locally with each oscillation representing a colloidal particle. Hence, attachment at valleys of ρ may drive the peaks of ρ above ρ_∞, which results in detachment. However, as discussed in the introduction, the attachment process for colloids is essentially irreversible so that detachment should be very limited.

To avoid this behavior one could use the simple form

$$j := Bi\,c \tag{5.33}$$

making the attachment and detachment independent of ρ by postulating that every existing colloid in the bulk will attach to the interface. In this case colloid saturaturation is reached when c is depleted.

Another way to overcome the oscillations of ρ and connect the macroscopic and microscopic bulk and surface colloid densities in Eq. (5.32) is to use an average $<\rho>$ instead of the microscopic ρ in Eq. (5.32) and take

$$j := Bi\left(c(\rho_\infty - <\rho>) - k^{-1}<\rho>\right), \tag{5.34}$$

where $<\rho>$ could be either a local or global average of ρ over the interface.

We have implemented all of the above formulations for the flux term j and observed that all of these formulations behave similarly, at least qualitatively. For the simulations presented in Sec. 5.4.1 we use Eq. (5.32) for j.

5.2.3   Summary of governing equations

Putting everything together, we now summarize the nondimensional Navier-Stokes-Cahn-Hilliard-Surface-Phase-Field-Crystal (NSCHSPFC) equations and the associated boundary conditions. We write the equations as a system of 2nd order partial differential equations. The advective Cahn-Hilliard equation governs the motion of the two-phase interface:

$$\partial_t\psi + \mathbf{u}\cdot\nabla\psi = Pe_\psi^{-1}\nabla\cdot(B\nabla\mu), \tag{5.35}$$
$$\mu = B'(\psi) - \epsilon^2\Delta\psi. \tag{5.36}$$

The Surface Phase-Field-Crystal equation on the diffuse interface defined by ψ governs the evolution of the surface colloids:

$$\partial_t(B\rho) + \nabla\cdot(B\mathbf{u}\rho) = Pe_\rho^{-1}\nabla\cdot(B\nabla\omega) + Bj, \tag{5.37}$$
$$B\omega = B(\rho - \tilde{\rho})\left((\rho - \tilde{\rho})^2 + 1 + r\right) + 2\delta^2 B\nu + \delta^4\nabla\cdot(B\nabla\nu), \tag{5.38}$$
$$B\nu = \nabla\cdot(B\nabla\rho), \tag{5.39}$$
$$j = Bi\left(c(\rho_\infty - \rho) - k^{-1}\rho\right). \tag{5.40}$$

The bulk colloid density evolves according to the convection-diffusion equation:

$$\partial_t(\psi c) + \nabla\cdot(\psi\mathbf{u}c) = Pe_c^{-1}\nabla\cdot(\psi\nabla c) - hj|\nabla\psi|. \tag{5.41}$$

Finally, the Navier-Stokes equations, with surface tension and elastic forces, governs the motion of the fluids:

$$
\begin{aligned}
\nabla \cdot \mathbf{u} &= 0, & (5.42) \\
\partial_t \mathbf{u} + (\mathbf{u} \cdot \nabla)\mathbf{u} &= -\nabla \bar{p} + \frac{1}{Re}\Delta \mathbf{u} + \frac{1}{\epsilon}\mu\nabla\psi \\
&\quad + \frac{El^{-1}}{\epsilon}B\left(\omega\nabla\rho - \nabla(f - \delta^4\nabla\nu \cdot \nabla\rho - \delta^4\nu^2)\right). & (5.43)
\end{aligned}
$$

The NSCHSPFC system is equipped with the initial conditions

$$
\mathbf{u}(t=0,\mathbf{x}) = \mathbf{u}_0(\mathbf{x}), \;\; \psi(t=0,\mathbf{x}) = \psi_0(\mathbf{x}), \;\; \rho(t=0,\mathbf{x}) = \rho_0(\mathbf{x}), \;\; c(t=0,\mathbf{x}) = c_0(\mathbf{x}), \quad \text{in } \Omega
$$

and either natural boundary conditions

$$
\frac{\partial\psi}{\partial\mathbf{n}} = \frac{\partial\rho}{\partial\mathbf{n}} = \frac{\partial c}{\partial\mathbf{n}} = \frac{\partial\mu}{\partial\mathbf{n}} = \frac{\partial\nu}{\partial\mathbf{n}} = \frac{\partial\omega}{\partial\mathbf{n}} = 0, \qquad \mathbf{u} = \mathbf{u}_\infty \quad \text{on } \partial\Omega,
$$

where $\mathbf{n}$ denotes the outward normal vector, or periodic boundary conditions.

5.3 Numerical methods

An adaptive finite element method is used to solve the high-order nonlinear system of equations; the method is implemented using the adaptive finite element toolbox AMDiS [VV07]. We solve the coupled system as follows. First the Cahn-Hilliard equations (5.35)-(5.36) are solved to determine the position of the interface, then the SPFC equations (5.37)-(5.40) are solved to determine the surface colloid density and finally the Navier-Stokes equations (5.42) and (5.43) are solved to determine the fluid velocity using the new position of the interface and the surface density of the colloids in the surface tension and elastic forces. If colloids are present in the bulk, then the Eq. (5.41) is solved after the Navier-Stokes equation. To ensure the well-posedness of Eqs. (5.37)-(5.39), B is replaced by $B+\xi$, see Ref.[RV06] for example. Analogously, in Eq. (5.41), ψ is replaced by $\psi + \xi$. Here, we use $\xi = 10^{-6}$.

A semi-implicit Euler method is used for the time discretization keeping as many terms implicit as possible. Nonlinear terms are linearized by a Taylor expansion dropping terms of order two and higher so that the equations are linear at the implicit time step. The linearized system is solved using the direct unsymmetric multifrontal method (UMFPACK [Dav95]).

We use linear basis functions for all variables. Accordingly, the Cahn-Hilliard and SPFC equations are solved as coupled systems of second order equations (e.g., see Refs.[ALV10, BAA07]). The Navier-Stokes equations are solved using a first order projection method developed in Ref.[Cho68]. The scheme is given by

$$\frac{\mathbf{u}^* - \mathbf{u}^{m-1}}{\tau} - \eta\Delta\mathbf{u}^* + \mathbf{u}^{m-1}\cdot\nabla\mathbf{u}^* + \nabla p^{m-1} = \tilde{\mathbf{F}}^m, \tag{5.44}$$

$$\tau\Delta p^* = \nabla\cdot\mathbf{u}^*, \tag{5.45}$$

$$\mathbf{u}^m = \mathbf{u}^* - \tau\nabla p^*, \tag{5.46}$$

$$p^m = p^{m+1} + p^*, \tag{5.47}$$

where τ denotes the timestep and the superscripts denote the time iteration.

Adaptive meshes are indispensible for providing a high spatial resolution along the fluid-fluid interfaces described implicitly by ψ. For local mesh adaptation, we use an L^2-like error indicator based on a jump residual (e.g., see Refs.[Ver96, VV07]) for ψ to maintain approximately 5 grid points across the transition layers. Although we did not find it necessary to do here, additional mesh refinement can be used to increase local resolution of the flow field (e.g., velocity gradients, etc.).

5.4 First simulation results

5.4.1 Retracting ellipse

As a first test for the NSCHSPFC model we consider the case of an initially elliptical fluid droplet surrounded by another fluid. The computational domain is $\Omega = [-2, 2] \times [-2, 2]$. We start with an initial condition as in Eq. (5.1) using

$$d = 1.0 - \sqrt{\left(\frac{x}{0.35}\right)^2 + \left(\frac{y}{1.8}\right)^2}.$$

Since this d is only an approximation to a signed distance function of an ellipse, we refine the initial condition by solving the Cahn-Hilliard equations (5.35) and (5.36) for a short time with velocity $\mathbf{u} = 0$ to obtain better approximation of Eq. (5.1) where the actual signed distance function is used. The resulting ψ is the initial condition ψ_0 for the following simulations. It describes an elliptical drop with a vertical diameter of about 3 and a horizontal thickness of around 0.75.

To get an initial condition for ρ we solve the SPFC equations (5.37)-(5.40) on the fixed interface defined by ψ_0 (e.g. $\mathbf{u}$ is set to zero). We use as an initial condition for ρ, a constant value of -0.3 plus a uniformly distributed random perturbation between $[-0.05, 0.05]$ at each node. Hereafter, we write such a condition as $\rho_0 = -0.3 \pm 0.05$. Since this surface density is in the crystal phase of the PFC, the colloidal particles become ordered and arrange in a crystal-like state. We stop solving the SPFC equations when a stationary state of colloid density is reached. The solution ρ shown in Fig. 5.1 is taken as the initial condition ρ_0 for the full NSCHSPFC system. Note that a single colloid corresponds to the combination of one darker region ($\rho < 0$) and one lighter region ($\rho > 0$). The remaining parameters are chosen as follows: $\tau = 0.017$, $r = -0.4$, $\tilde{\rho} = 0$, $Pe_\rho = 3.76$, $Pe_\psi = 0.47$, $Re = 0.38$, $El = 0.002$, $\epsilon = 0.03$, $\delta = 0.067$, $Bi = 0$ and the fluid is initially quiescent (e.g., $\mathbf{u} = 0$ at time $t = 0$). The natural boundary conditions with $\mathbf{u}_\infty = \mathbf{0}$ are used.
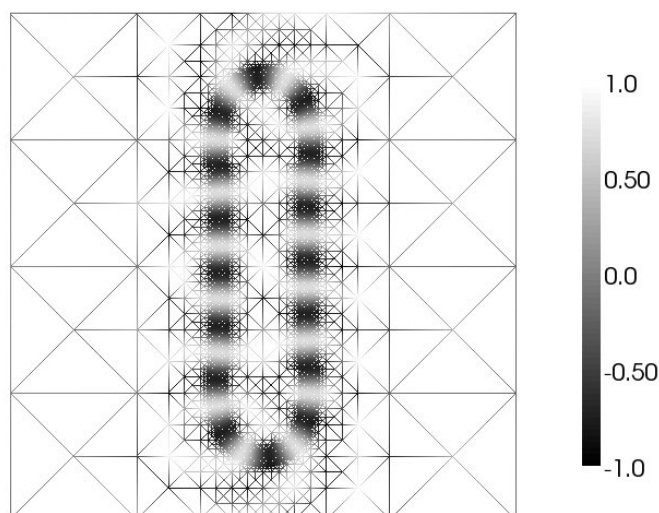
Figure 5.1: Initial condition ρ_0 for the NSCHSPFC system obtained by solving the SPFC equation on an elliptical diffuse interface, as described in the text.

Fig. 5.2 shows the NSCHSPFC simulation (bottom) and a comparison to the NSCH model (top) which has no elastic force ($El^{-1} = 0$). One can see that in the latter case surface tension makes the ellipse retract to become circular. However, in the presence of colloids, the retraction is stopped by the elastic force as the colloids jam at the interface and the interface crystallizes. Note that at late times, the interface may start to wobble a little. This is likely due to the combination of the surface elasticity induced by the colloids and the inertial forces in the fluid.

The velocity **u** at the top of the ellipse at an early time ($t = 1.67$) is shown in Fig. 5.3. The elastic force induces local straining flows around the interface (two per colloid). The maximum magnitudes of the velocities induced by the surface tension and elastic force are about ten times larger than that induced by surface tension only. Consequently, we need to use smaller timesteps and a finer grid in a neighborhood of the interface to resolve the system with elastic forces than are required to solve the system without elastic forces. The magnitude of the straining flows can be decreased by increasing El. To compensate for an increased El, the number of colloids on the interface may be increased, which increases the interface stiffness by enabling colloid jamming and interface crystallization to occur more readily. This can be achieved by making the colloidal particles smaller resulting in a smaller parameter δ, as we now demonstrate.

To investigate the influence of the number of colloids on the system we vary the parameter δ, which relates the characteristic colloid size to the characteristic drop radius. Now we proceed as before. We first solve the SPFC equation on a fixed interface until a stationary state is reached. We use three values of $\delta = 0.133$, 0.067 and 0.033. This yields 8, 16 and 32 colloids on the interface as seen in Fig. 5.4. Using the same parameters and boundary conditions as before, with the exception of δ, the initial ellipses are evolved in time in an initially quiescent fluid.

In Fig. 5.5, the interface length, calculated from the length of the $\psi = 0.5$ contour, is plotted as a function of time. In all cases the elastic force is strong enough to stop the retraction, with the decrease in length being inversely proportional to δ. Thus, increasing the number of colloids makes the interface stiffer by making it easier for the colloids to jam. Note that for $\delta = 0.133$, a minimum
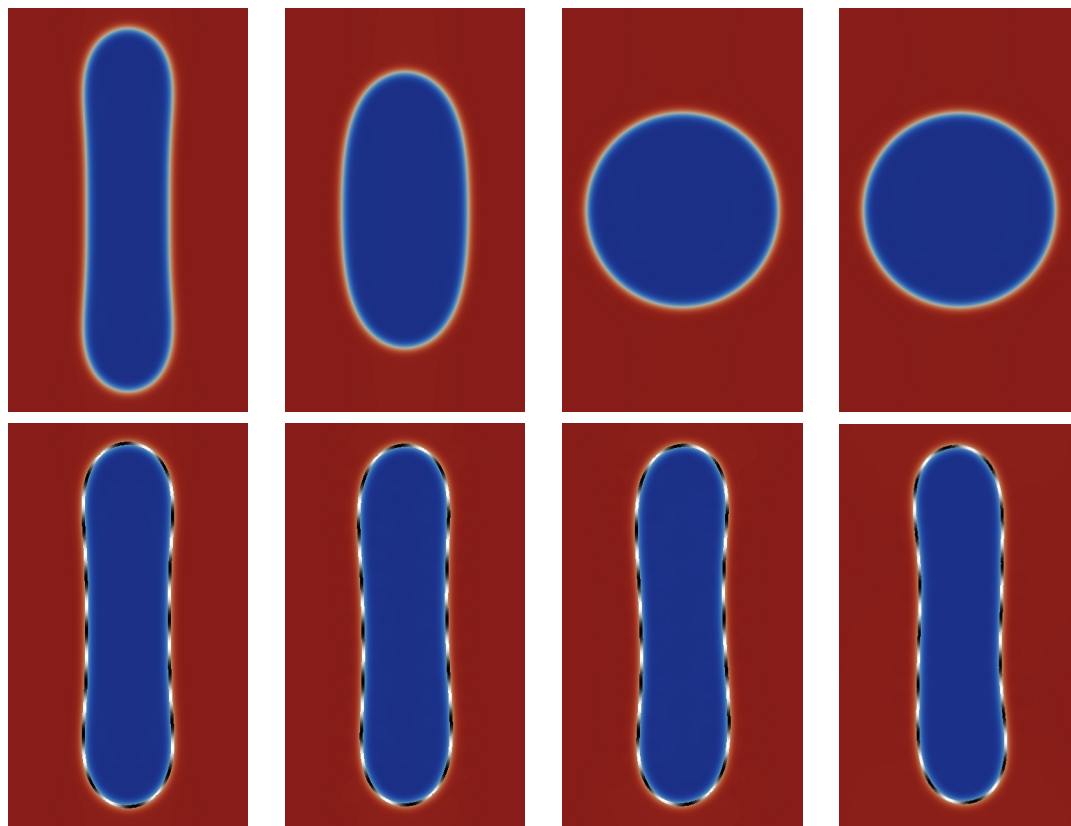
Figure 5.2: Retraction of an elliptical drop without (top) and with (bottom) colloidal forces at times $t = 0, 33, 167, 1671$, from left to right. The drop and matrix fluids have different shades, lighter (red online) for $\psi = 1$ and darker (blue online) for $\psi = 0$. The colloids (ρ) on the interface are colored black ($\rho < 0$) and white ($\rho > 0$).
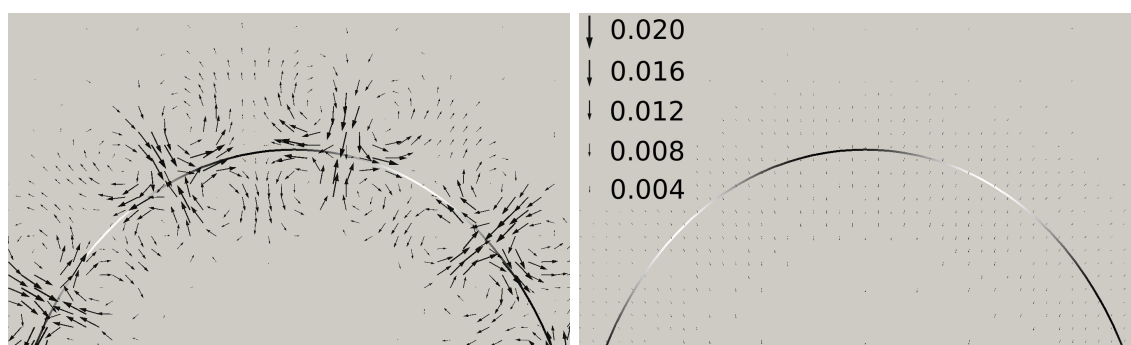
Figure 5.3: Velocity field at the top of the ellipse at the early time $t = 1.67$. The black-white curve represents the interface. Left: The NSCHSPFC system induces localized straining flows along the interface. Right: The velocity induced by surface tension only (elastic force turned off, $El^{-1} = 0$), at the same time, for comparison.
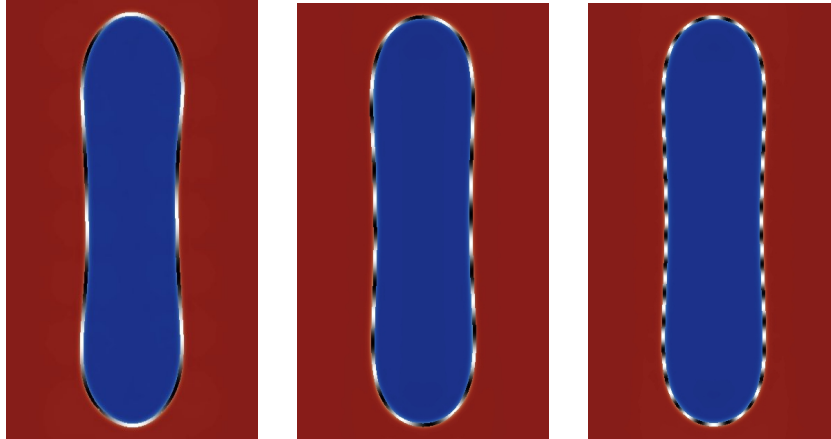
Figure 5.4: Drop morphologies with 8, 16 and 32 colloids at the interface used as initial condition for the NSCHSPFC model.
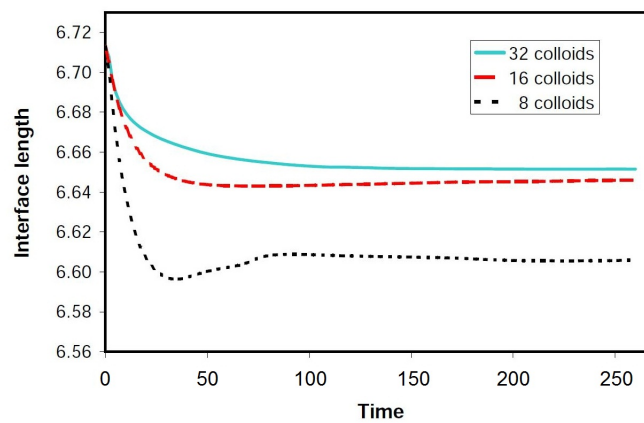
Figure 5.5: Interface length as a function of time for different numbers of colloids on the interface, see text for details.

in interface length occurs around time $t \approx 50$ as the drop starts to retract to a circle; its length only decreases by only about 1% though. After this, the particles seem to slightly over compress and the drop rebounds a little to an equilibrium configuration. This occurs to a much lesser extent for the case 16 colloids. In the case with 32 colloids, the interface length evolves monotonically with very slight decrease in length. To reach the smaller values of δ needed to model specific experiments (e.g., Refs.[COFC05, HWS$^+$07, FMD09]), larger scale simulations are necessary. This is currently research in progress.

Next, we incorporate attachment into the system. Therefore we solve an additional concentration equation as described in Sec. 5.2.2. As initial condition we impose a colloid concentration in the lower region of the domain:

$$c_0(x, y) = \begin{cases} 1, & \text{if } y < -1.67 \\ 0, & \text{else.} \end{cases}$$

The parameters are the same as before, with $\delta = 0.067$, and the parameters associated with attachment are $Bi = 0.6$, $k^{-1} = 0$, $Pe_c = 37.6$, $h = 0.67$, and $\rho_\infty = 0.0$. The initial surface colloid density $\rho_0 = -0.8$, which is in the liquid phase of the PFC (e.g., the colloid phase is disordered). Thus, attachment is needed to order the colloids and crystallize the interface. Accordingly, the surface colloid structure evolves dynamically together with the interface evolution and attachment from the bulk matrix fluid. The results, shown in Fig. 5.6, show that colloids attach to and crystallize the interface starting at the bottom of the ellipse (closest to the bulk source) and move upwards as time progresses. Correspondingly, the retraction stops first at the bottom of the ellipse, since the colloids jam there first, with the retraction becoming progressively more arrested as the colloid structure moves up the ellipse. This leads to the development of an asymmetrical shape because the drop retracts more at the top.

5.4.2 Drop in shear flow

We consider a drop in shear flow to show that the colloids on the interface induce both repulsive and attractive forces. This ability to impart rigidity, akin to surface elasticity, is an important difference between colloid stabilized and surfactant stabilized systems. Surfactants can lower the surface tension but they do not generally result in significant surface elasticity. This makes it easier for colloid stabilized systems to resist external forces such as arise in an externally applied shear flow.

To illustrate this, we simulated a drop with colloids and elastic force (NSCHSPFC), a drop without colloids (NSCH) and a drop without colloids but with insoluble surfactants on its surface. The latter can be modeled using the tools from chapter 2 which yields the same formulation as in Teigen et al. [TSLV10]. According to Eqs. (2.66) and (2.16) the surfactant concencentration c_s on the interface satisfies:

$$\partial_t(Bc_s) + \nabla \cdot (B\mathbf{u}c_s) = \frac{1}{Pe_{c_s}}\nabla \cdot (B\nabla c_s), \tag{5.48}$$

where Pe_{c_s} is the surfactant Peclet number. The nondimensional surface tension (scaled by the clean surface tension) is now dependent on c_s and using the linear expansion of Eq. 2.53 around $c_s = 0$
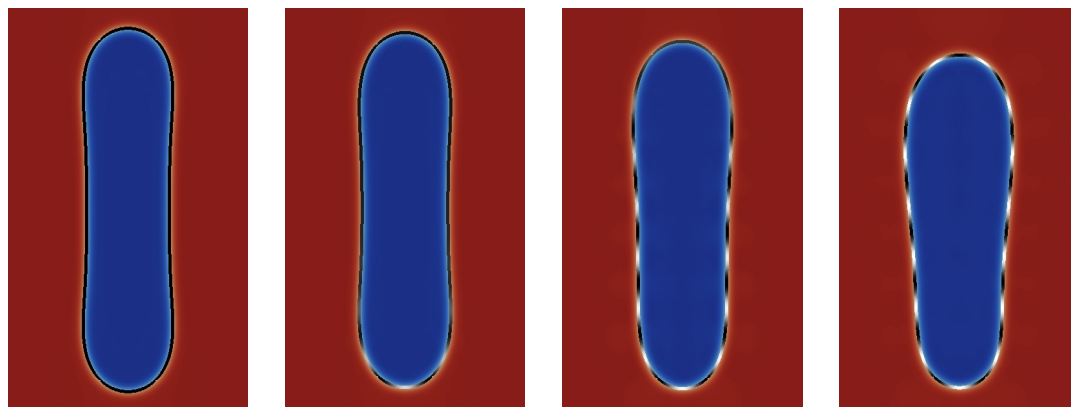
Figure 5.6: Retraction of an elliptical drop with simulated attachment of colloids. From left to right, the times shown are $t = 0, 3.3, 10.0, 33.4$
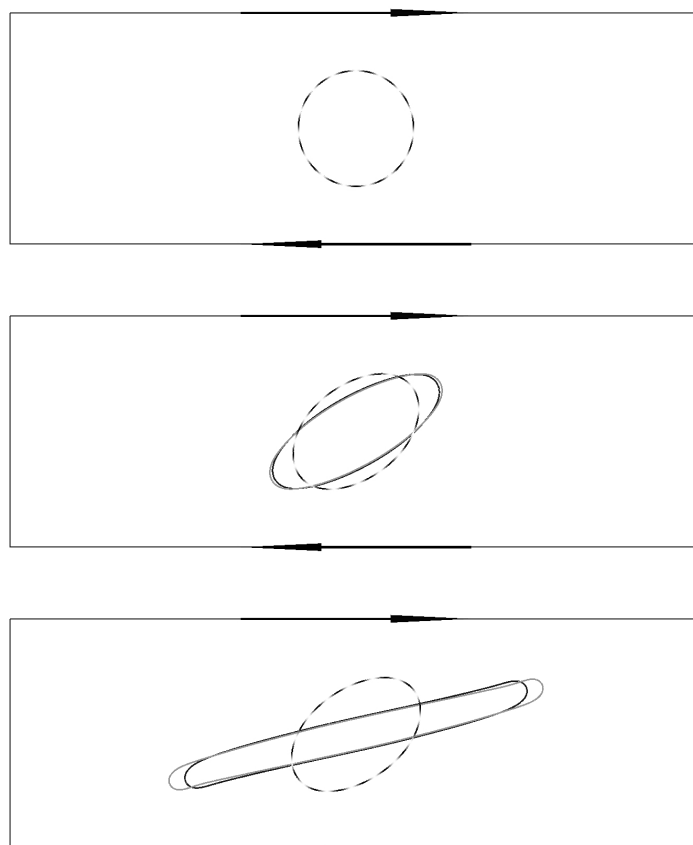

Figure 5.7: A drop under shear flow. With colloids (black-white), without colloids (black) and with insoluble surfactants on the interface (grey) at times $t = 0, 10.0, 33.4$.

yields

$$\sigma_s = (1 - \beta c_s). \tag{5.49}$$

with a constant factor β. Having a space dependent surface tension makes it necessary to account for the additional Marangoni force term $-\sqrt{2}/6\, \nabla_\Gamma \sigma_s \delta_\Gamma$ in the Navier-Stokes equations (see Eq. (2.69)). Here, the $\sqrt{2}/6$ arises in order to match the scaling of the interface delta function δ_Γ with the scaling of the surface tension force, see Secs. 2.6.2 and 2.2. Using $|\nabla\psi|$ as approximation to the surface delta function and Eq. (2.31) yields following force in the Navier-Stokes equation

$$\mathbf{F} = (1 - \beta c_s)\frac{\delta E_\sigma}{\delta\psi}\nabla\psi - \frac{\sqrt{2}}{6}\beta|\nabla\psi|\left(\mathbf{I} - \frac{\nabla\psi \otimes \nabla\psi}{|\nabla\psi|^2}\right)\nabla c_s, \tag{5.50}$$

to account for the capillary and Marangoni forces. An asymptotic analysis as $\epsilon \to 0$ reveals that this formulation approximates the desired sharp interface limit $\frac{6}{\sqrt{2}}\mathbf{F} \sim -(1 - \beta c_s)\kappa\delta_\Gamma\mathbf{n} - \beta\nabla_s c_s\delta_\Gamma$.

In our simulations we use $\beta = 0.5$, $Pe_{c_s} = 39$ and the initial condition $c_s = 1.0$. Here the domain size is $\Omega = [-6, 6] \times [-2, 2]$ and a drop of radius 1 is placed in the center. To obtain an initial configuration with colloids on the interface, we solve the SPFC equations first on this fixed interface to steady state starting from an initial colloid density $\rho_0 = -0.3 \pm 0.05$. This creates a stationary state with 15 colloids at the circular interface. Note that there are fewer colloids here than in the elliptical case considered previously since the interface length is smaller. This solution ρ is taken as the initial condition for the complete NSCHSPFC system. We take $\tau = 0.0084$, $El = 4 \times 10^{-4}$, $\delta = 0.067$, $Bi = 0$ and the remaining parameters as in the previous section. We use periodic boundary conditions on the left and right boundaries of the domain. At the top and bottom boundaries, the natural boundary conditions are used with $\mathbf{u}_\infty = (0.24, 0)$ and $\mathbf{u}_\infty = (-0.24, 0)$, respectively. The initial fluid velocity is $\mathbf{u}_0 = (0.12\, y, 0)$.

The result is shown in Fig. 5.7. The drop with colloids (black and white) deforms only slightly and reaches a steady morphology around time $t = 10$ and thereafter resists deformation by the shear flow. In contrast, the drop with surfactants (grey) and the clean drop without colloids and surfactants ($\beta = 0$, $El^{-1} = 0$, black) increasingly elongate in time. As expected the drop with surfactants deforms the most.

5.4.3 Stabilizing bicontinuous structures

We next investigate the potential of colloidal particles to stabilize bicontinuous structures generated by spinodal decomposition in the computational domain $[-2, 2] \times [-2, 2]$. We first attempted to model this by solving the full NSCHSPFC system using an initial condition in which the fluid is quiescent, no interface is present (e.g., $\psi = 0.5 \pm 0.1$) and colloids are only present in the bulk. Thus interface crystallization should arise from attachment of colloids at the interface as it nucleates and coarsens. However, we found that the fluid phases never reached a steady, stable state due to the competing effects between the sizes of the fluid structures that form at early times and the colloid sizes. In particular, the fluid structures should be larger than the size of the colloids (e.g., $\delta < 1$).

As an alternative initial condition, we first generate sufficiently large fluid structures via spinodal decomposition by solving the CH equation in the absence of flow ($\mathbf{u} = 0$) using the initial condition for ψ mentioned above with a large interface thickness $\epsilon = 0.16$ for a few time steps. Then, to generate the initial condition for the full NSCHSPFC system, the CH and SPFC equations are solved together for several more time steps, again in the absence of flow, with $\epsilon = 0.03$ to refine the interface thickness and to create the colloid structure on the complex interface. As initial data for the CH-SPFC solve, the previously generated ψ is used together with the colloid density $\rho_0 = -0.3 \pm 0.05$. The resulting ψ, ρ are used as the initial condition ψ_0, ρ_0 for the full NSCHSPFC system. The parameters are the same as in Sec. 5.4.1 with $\delta = 0.067$; periodic boundary conditions are used in each coordinate direction.

Figure 5.8 shows a comparison between the NSCHSPFC model (bottom) and a NSCH model without the elastic force ($El^{-1} = 0$, top). In the latter case the structure coarsens significantly. When colloids are present, the elastic force induced by the particles is able to prevent the coarsening as the colloids jam and the interface crystallizes. Indeed, it can be seen in Fig. 5.10 the interface length (long-dashed) decreases only slightly throughout the simulation. In contrast, without colloids, the interface length decreases substantially over the simulation (solid). Hence, the colloids stabilize the system against coarsening.
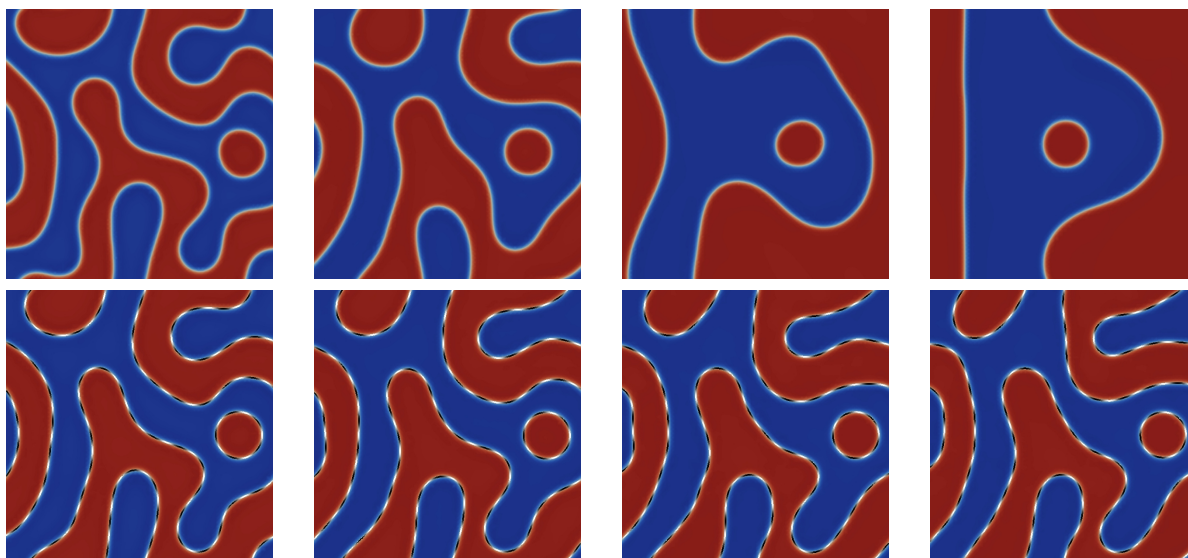
Figure 5.8: The evolution of a complex fluid structure generated by spinodal decomposition without (top) and with (bottom) colloidal forces at times $t = 0, 16.7, 83.6, 167$, from left to right. The presence of colloids arrests the coarsening.

5.4.4 Stabilizing bicontinuous structures using coarsening-induced jamming

Interface coarsening provides another route to driving the surface colloid density ρ into the crystal part of the PFC phase diagram, leading to colloid jamming and interface crystallization. For example, if the fluid structure coarsens in time and the interface length decreases then, in the absence of attachment, the absolute value of ρ increases. This can bring ρ into the crystal phase of the SPFC and thus induces crystallization of the interface.
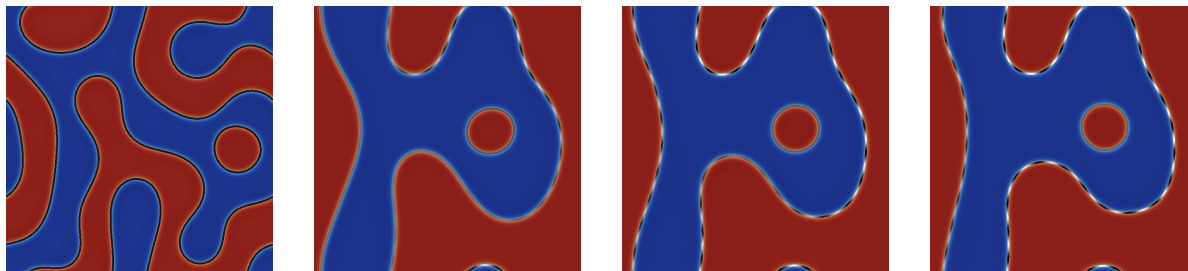
Figure 5.9: Coarsening of a complex fluid structure with simulated jamming of colloids. The times shown are $t = 0, 58.5, 83.6, 167$, from left to right.

To simulate coarsening-induced jamming we use the same initial interfacial configuration in Sec. 5.4.3 but start with an unordered colloid configuration. We test whether ordering and crystallization of the interface may occur as the complex fluid structure coarsens. Here, we take $\tilde{\rho} = 1$ which leads due to the conservation of $\rho + \tilde{\rho}$ to an increase in ρ when the interface length decreases. The initial SPFC density is $\rho_0 = -0.65$, ψ_0 and the remaining parameters as the same as in Sec. 5.4.3.

The results are shown in Fig. 5.9. At early times, the fluid structure coarsens and the NSCHSPFC evolution is very similar to that for the NSCH system without colloids (Fig. 5.8(top)). At these early times, the interface has not yet crystallized. Therefore the elastic force is small and the evolution is dominated by the surface tension force. As the interface coarsens, the colloid density increases and eventually reaches the limit where the colloids jam and the interface crystallizes. This occurs around time $t \approx 60$ and crystallization begins in the upper right portion of the interface first. The crystal region then spreads rapidly around the interface. Interestingly, although the coarsening slows significantly after the initial crystallization, the increased elastic forces do not immediately stop the coarsening because there are some adjustments in the colloid distribution that result in changing the local colloid density (particularly at the upward pointing finger in the center of the domain). This results in a small amount of additional localized coarsening. As the colloid density equilibrates and the colloids jam fully, the coarsening of the fluid structure ceases. Note that crystallization does not occur on the isolated drop because the drop is nearly circular and thus does not coarsen enough to increase the colloid density to the crystallization limit.

To quantify the coarsening process, the total interface length (calculated as described earlier) is plotted in Fig. 5.10 as a function of time for the three simulations modeling the bicontinuous structures (Figs. 5.8 and 5.9). At early times, before the interface crystallizes, the interface length for the simulation shown in Fig. 5.9 (short dashed) evolves very similarly as the case without colloids ($El^{-1} = 0$, solid). Thus, the elastic force seems to have almost no effect on the system if the surface colloid density is in the liquid phase. The point at which the colloids start to jam and the interface begins to crystallize is clearly indicated by the abrupt stop in the decrease of the interface length around $t \approx 60$. The additional localized coarsening that occurs in response to colloid redistribution is seen by the slight decrease in interface length around $t \approx 80$. After the colloids jam fully, the interface length stays almost perfectly constant.
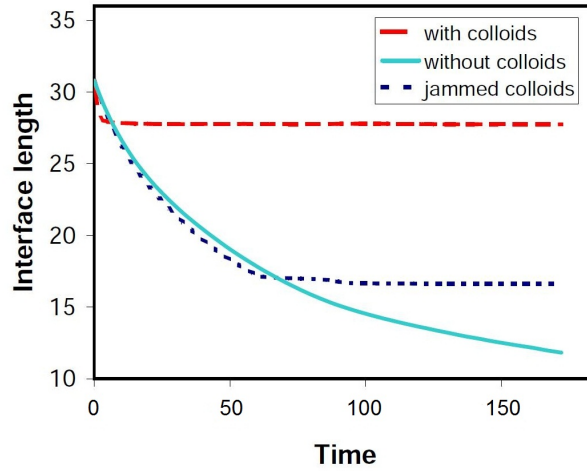
Figure 5.10: The evolution of the interface length for the simulations shown in Figs. 5.8 and 5.9. Without elastic force (solid line), with elastic force from the beginning (long-dashed) and with elastic force where the colloids jam and the interface crystallizes during coarsening (short-dashed).

5.5   A regularized elastic force

It was demonstrated so far that the NSCHSPFC model is capable to describe, at least phenomenologically, two-phase systems where colloids are present at the interface. However, we have also seen that the colloidal force induces strong local straining flows around the interface, which require small time steps and a fine grid to be resolved. The aim of this section is to improve the model by suppressing these spurious velocities. Let us recall that the force in the Navier-Stokes equation can be written as

$$\mathbf{F} = \mu\nabla\psi + \frac{El^{-1}}{\epsilon}B(\psi)\omega\nabla\rho + \mathbf{F}_{el}, \tag{5.51}$$

with

$$\mathbf{F}_{el} = \frac{El^{-1}}{\epsilon}\nabla B(\psi)\left(f - \delta^4\nabla\nu\cdot\nabla\rho - \delta^4\nu^2\right), \tag{5.52}$$

where $\mathbf{F}_{el}$ is the part of the colloidal force directed normal to the interface. In the following we will refer to $\mathbf{F}_{el}$ as elastic force. This force is responsible for the induced spurious velocities, since ∇B is directed in opposing directions on both sides of the interface.

We will now present a way to regularize $\mathbf{F}_{el}$ which can eliminate the spurious flows. The idea is to average $\mathbf{F}_{el}$ over a control volume located at the interface and then take the limit as the control volume becomes infinitesimally small. To do this, we will restrict ourselves to 2D and consider a single point x_0 on the interface (see Fig.5.11). We define a control volume with tangential thickness Δs and normal thickness Δz which we assume large enough to capture all of the non-zero part of $\mathbf{F}_{el}$ in a vicinity of x_0, e.g. $\epsilon \ll \Delta z$. If we now calculate the integral of $\mathbf{F}_{el}$ over V and let Δs tend to zero, we will get the effective force acting on the interface at x_0.
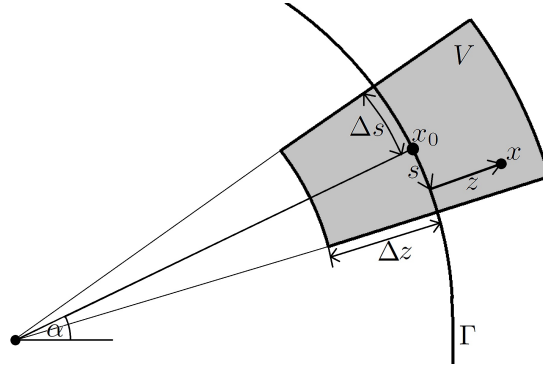
Figure 5.11: The control volume V defined around an arbitrary interface point x_0.

A coordinate point x in V can be expressed using the arc length s and the normal distance z by

$$x(s, z) = \left(\frac{1}{\kappa} + z\right)(\cos(\alpha + \kappa s), \sin(\alpha + \kappa s)), \tag{5.53}$$

where κ is the curvature of the interface at the point $x(s, 0)$. The Jacobian matrix of this coordinate transformation reads

$$J = \begin{pmatrix} \cos(\alpha + \kappa s) & -(1 + \kappa z)\sin(\alpha + \kappa s) \\ \sin(\alpha + \kappa s) & (1 + \kappa z)\cos(\alpha + \kappa s) \end{pmatrix}. \tag{5.54}$$

Now, we consider the integral of $\mathbf{F}_{el}$ over the volume V,

$$\int_V \mathbf{F}_{el}\mathrm{d}x = \int_{-\Delta s}^{\Delta s}\int_{-\Delta z}^{\Delta z} \mathbf{F}_{el}|J|\mathrm{d}z\mathrm{d}s \tag{5.55}$$

$$= \int_{-\Delta s}^{\Delta s}\int_{-\Delta z}^{\Delta z} \mathbf{F}_{el}(1 + \kappa z)\mathrm{d}z\mathrm{d}s \tag{5.56}$$

$$= \frac{El^{-1}}{\epsilon}\int_{-\Delta s}^{\Delta s}\int_{-\Delta z}^{\Delta z} \nabla B(\psi)\left(\frac{1}{4}\rho^4 + \frac{1+r}{2}\rho^2 - \delta^2|\nabla\rho|^2\right.$$
$$\left. - \frac{\delta^4}{2}\nu^2 - \delta^4\nabla\nu\cdot\nabla\rho\right)(1 + \kappa z)\mathrm{d}z\mathrm{d}s. \tag{5.57}$$

Since ρ and ν are constant in the normal direction to first order, it holds

$$\rho(x(s, z)) \approx \rho(x(s, 0)), \quad \nu(x(s, z)) \approx \nu(x(s, 0)) \tag{5.58}$$

and consequently

$$\nabla\rho(x(s, z)) \approx \nabla\rho(x(s, 0))\frac{1}{1 + \kappa z}, \quad \nabla\nu(x(s, z)) \approx \nabla\nu(x(s, 0))\frac{1}{1 + \kappa z}. \tag{5.59}$$

Using this in (5.57) we get

$$\int_V \mathbf{F}_{el} dx \approx \frac{El^{-1}}{\epsilon} \int_{-\Delta s}^{\Delta s} \left(\frac{1}{4}\rho^4 + \frac{1+r}{2}\rho^2 - \frac{\delta^4}{2}\nu^2 \right) (x(s,0))$$
$$\cdot \int_{-\Delta z}^{\Delta z} \nabla B(\psi)(1+\kappa z) \ dz ds$$
$$- \frac{El^{-1}}{\epsilon} \int_{-\Delta s}^{\Delta s} \left(\delta^2 |\nabla \rho|^2 + \delta^4 \nabla \nu \cdot \nabla \rho \right) (x(s,0))$$
$$\cdot \int_{-\Delta z}^{\Delta z} \nabla B(\psi) \frac{1}{1+\kappa z} \ dz ds. \tag{5.60}$$

Using that $B = \psi^2(1-\psi)^2$ and Eq.(5.1), the integrals over z can be approximated analytically. For $\epsilon \to 0$ it holds

$$\int_{-\Delta z}^{\Delta z} \nabla B(\psi)(1+\kappa z) dz \to -\frac{1}{6\sqrt{2}}\epsilon \mathbf{n}\kappa, \tag{5.61}$$

$$\int_{-\Delta z}^{\Delta z} \nabla B(\psi) \frac{1}{1+\kappa z} dz \to +\frac{1}{6\sqrt{2}}\epsilon \mathbf{n}\kappa. \tag{5.62}$$

Hence, we get

$$\int_V \mathbf{F}_{el} dx \approx -\frac{El^{-1}}{6\sqrt{2}} \int_{-\Delta s}^{\Delta s} \kappa \mathbf{n} g(x(s,0)) ds, \tag{5.63}$$

$$\tag{5.64}$$

where

$$g := \frac{1}{4}\rho^4 + \frac{1+r}{2}\rho^2 - \frac{\delta^4}{2}\nu^2 + \delta^2 |\nabla \rho|^2 + \delta^4 \nabla \nu \cdot \nabla \rho. \tag{5.65}$$

Hence, we have

$$\int_V \mathbf{F}_{el} dx = \int_V -\frac{El^{-1}}{6\sqrt{2}}\delta_\Gamma \kappa \mathbf{n} g ds, \tag{5.66}$$

with a Dirac interface delta function δ_Γ. Now, letting the control volume V become infinitesimal small by taking $\Delta s \to 0$ leads to the point force

$$\mathbf{F}_{new} := -\frac{El^{-1}}{6\sqrt{2}}\delta_\Gamma \kappa \mathbf{n} g \tag{5.67}$$

at x_0. Since the above calculations hold for arbitrary x_0, this point force is valid in every interface point. Note that $\mathbf{F}_{new}$ can be seen as the sharp interface version of $\mathbf{F}_{el}$, which we confirm in Sec.5.7. Now, we can use the Cahn Hilliard chemical potential to approximate the curvature and hence get a diffuse

interface version of $\mathbf{F}_{new}$. According to Eq. (2.30) we have for $\epsilon \to 0$

$$\mu \nabla \psi \to -\frac{1}{3\sqrt{2}} \kappa \delta_\Gamma \mathbf{n} \tag{5.68}$$

which leads to the approximation

$$\mathbf{F}_{new} \approx \frac{El^{-1}}{2} g\mu\nabla\psi. \tag{5.69}$$

Now, the new governing equations are (5.35)-(5.42) with the new momentum equation:

$$\partial_t \mathbf{u} + (\mathbf{u} \cdot \nabla)\mathbf{u} = -\nabla\bar{p} + \frac{1}{Re}\Delta\mathbf{u} + \mu\nabla\psi + \frac{El^{-1}}{\epsilon}B(\psi)\omega\nabla\rho + \mathbf{F}_{new}. \tag{5.70}$$

Note that the new system converges to the old system as $\epsilon \to 0$, since $\mathbf{F}_{el} \to \mathbf{F}_{new}$. We confirm in Sec. 5.4.1, that the new elastic force eliminates spurious velocities and leads to improved properties of the system.

5.6   A variational diffuse interface model

In this section we will present a variational approach to derive a diffuse interface system containing the new elastic force. To do so, we introduce a new approximation to the surface delta function,

$$e = \frac{\epsilon^2}{4}|\nabla\psi|^2 + \frac{1}{2}B(\psi), \tag{5.71}$$

which has the same scaling to the surface delta function as B. This form of an approximation to the surface delta function has already been used in [LRV09, RV07]. Now, we use e instead of B to restrict the PFC energy to the interface:

$$\tilde{E}_{spfc} = \frac{El^{-1}}{\epsilon} \int_\Omega e\tilde{f}\mathrm{d}x, \quad \text{with} \tag{5.72}$$

$$\tilde{f} = \frac{1}{4}\rho^4 + \frac{1+r}{2}\rho^2 - \delta^2|\nabla\rho|^2 + \frac{\delta^4}{2}\tilde{\nu}^2, \tag{5.73}$$

$$\tilde{\nu} = \frac{1}{e}\nabla \cdot (e\nabla\rho). \tag{5.74}$$

Note, that we will use the tilde notation to distinguish variables that differ from the original model. The total energy to be considered is now

$$\tilde{E} = \tilde{E}_{spfc} + E_\sigma + E_{kin}. \tag{5.75}$$

5.6.1 Energy variation

We now derive the equations for the two-phase system with colloidal particles starting with an energy variation argument. To do so, we suppose the fluid motion is governed by the Navier-Stokes equations, which are given by

$$\dot{\mathbf{u}} = -\mathbf{u} \cdot \nabla \mathbf{u} - \nabla p + \frac{1}{Re} \Delta \mathbf{u} + \tilde{\mathbf{F}}, \quad \nabla \cdot \mathbf{u} = 0, \tag{5.76}$$

where the overdot denotes the time derivative, p is the pressure and the force $\tilde{\mathbf{F}}$ is as yet unspecified. Note that if Re is small, the Stokes equations could be used instead of the Navier-Stokes equations and the analysis below remains valid. It is often useful to represent forces in the Navier-Stokes equation as the divergence of a stress tensor. Hence, our goal will be to derive a singular stress tensor, whose divergence will be $\tilde{\mathbf{F}}$. Furthermore, the functions ψ and ρ are assumed to satisfy the conservation equations

$$\dot{\psi} = - \mathbf{u} \cdot \nabla \psi - \nabla \cdot \tilde{\mathbf{J}}_\psi, \tag{5.77}$$

$$\frac{\partial}{\partial t} (e(\rho + \tilde{\rho})) = - \nabla \cdot (e\mathbf{u}(\rho + \tilde{\rho})) - \nabla \cdot \tilde{\mathbf{J}}_\rho, \tag{5.78}$$

where the fluxes $\tilde{\mathbf{J}}_\rho$ and $\tilde{\mathbf{J}}_\psi$ have also not yet been specified. Note that Eq. (5.78) is the basic diffuse interface form of the surface mass conservation equation[RV06, TLL$^+$09], where $\rho + \tilde{\rho}$ is conserved as discussed in Sec. 5.2.1. Using the incompressibility of the fluid and Eq. (5.77), Eq. (5.78) can be rewritten as

$$e(\dot{\rho} + \mathbf{u} \cdot \nabla \rho) = - (\rho + \tilde{\rho}) (\dot{e} + \mathbf{u} \cdot \nabla e) - \nabla \cdot \tilde{\mathbf{J}}_\rho. \tag{5.79}$$

We next take the time derivative of the energy $\tilde{E}$ and insert the previously defined evolution equations for ρ, ψ and $\mathbf{u}$. Requiring that $\dot{\tilde{E}} \leq 0$ enables us to pose constitutive relations for the singular stress tensor and fluxes. First, we compute

$$\dot{E}_{kin} = \int_\Omega \mathbf{u}\dot{\mathbf{u}} \, \mathrm{d}x. \tag{5.80}$$

Inserting (5.19) into (5.80) and integrating by parts gives

$$\dot{E}_{kin} = \int_\Omega -\frac{1}{Re} \nabla \mathbf{u} : \nabla \mathbf{u} + \mathbf{u} \cdot \tilde{\mathbf{F}} \, \mathrm{d}x, \tag{5.81}$$

where $\nabla \mathbf{u} : \nabla \mathbf{u} = \left(\frac{\partial \mathbf{u}_i}{\partial x_j} \right) \frac{\partial \mathbf{u}_i}{\partial x_j}$. Next, we consider the surface energy E_σ and get

$$\dot{E}_\sigma = \int_\Omega \frac{1}{\epsilon} B'(\psi)\dot{\psi} + \epsilon \nabla \psi \cdot \nabla \dot{\psi} \, \mathrm{d}x. \tag{5.82}$$

Inserting Eq. (5.77) yields

$$
\begin{aligned}
\dot{E}_\sigma =& \int_\Omega -\frac{1}{\epsilon}B'(\psi)\nabla\psi\cdot\mathbf{u} - \epsilon\nabla\psi\cdot\nabla\nabla\psi\cdot\mathbf{u} - \epsilon\nabla\psi\cdot\nabla\mathbf{u}\cdot\nabla\psi \\
&- \frac{1}{\epsilon}B'(\psi)\nabla\cdot\tilde{\mathbf{J}}_\psi - \epsilon\nabla\psi\cdot\nabla\nabla\cdot\tilde{\mathbf{J}}_\psi \,\mathrm{d}x
\end{aligned}
\tag{5.83}
$$

$$
\begin{aligned}
=& \int_\Omega -\mathbf{u}\cdot\nabla\left[\frac{1}{\epsilon}B(\psi) + \frac{\epsilon}{2}|\nabla\psi|^2\right] - \epsilon\nabla\psi\otimes\nabla\psi:\nabla\mathbf{u} \\
&- \frac{1}{\epsilon}B'(\psi)\nabla\cdot\tilde{\mathbf{J}}_\psi - \epsilon\nabla\psi\cdot\nabla\nabla\cdot\tilde{\mathbf{J}}_\psi \,\mathrm{d}x.
\end{aligned}
\tag{5.84}
$$

Integrating by parts and dropping all boundary terms gives

$$
\dot{E}_\sigma = \int_\Omega \mathbf{u}\cdot\nabla\cdot(\epsilon\nabla\psi\otimes\nabla\psi) - \left(\frac{1}{\epsilon}B'(\psi) + \epsilon\nabla\psi\cdot\nabla\right)\nabla\cdot\tilde{\mathbf{J}}_\psi \,\mathrm{d}x.
\tag{5.85}
$$

Next, we can compute

$$
\dot{\tilde{E}}_{spfc} = \frac{El^{-1}}{\epsilon}\int_\Omega \dot{e}\tilde{f} + e\dot{\tilde{f}} \,\mathrm{d}x
\tag{5.86}
$$

$$
= \frac{El^{-1}}{\epsilon}\int_\Omega \tilde{f}(\dot{e} + \mathbf{u}\cdot\nabla e) + e(\dot{\tilde{f}} + \mathbf{u}\cdot\nabla\tilde{f}) - \mathbf{u}\cdot\nabla(e\tilde{f}) \,\mathrm{d}x
\tag{5.87}
$$

$$
= \frac{El^{-1}}{\epsilon}\int_\Omega \tilde{f}(\dot{e} + \mathbf{u}\cdot\nabla e) + e(\dot{\tilde{f}} + \mathbf{u}\cdot\nabla\tilde{f}) \,\mathrm{d}x.
\tag{5.88}
$$

Now, we will evaluate $\int_\Omega e(\dot{\tilde{f}} + \mathbf{u}\cdot\nabla\tilde{f})\,\mathrm{d}x$. To make the calculations clearer, we split $\tilde{f}$ into its zero order part $\tilde{f}_0 = \frac{1}{4}\rho^4 + \frac{1+r}{2}\rho^2$, its first order part $\tilde{f}_1 = -\delta^2|\nabla\rho|^2$ and its second order part $\tilde{f}_2 = \frac{\delta^4}{2}\tilde{\nu}^2$. Accordingly, we obtain

$$
\int_\Omega e(\dot{\tilde{f}}_0 + \mathbf{u}\cdot\nabla\tilde{f}_0)\,\mathrm{d}x = \int_\Omega e(\dot{\rho} + \mathbf{u}\cdot\nabla\rho)(\rho^3 + (1+r)\rho)\,\mathrm{d}x,
\tag{5.89}
$$

$$
\int_\Omega e(\dot{\tilde{f}}_1 + \mathbf{u}\cdot\nabla\tilde{f}_1)\,\mathrm{d}x = \int_\Omega -2e\delta^2\nabla\rho\nabla\dot{\rho} - 2e\delta^2\nabla\nabla\rho:(\nabla\rho\otimes\mathbf{u})\,\mathrm{d}x
\tag{5.90}
$$

$$
= \int_\Omega 2e\delta^2\tilde{\nu}(\dot{\rho} + \mathbf{u}\cdot\nabla\rho) + 2e\delta^2\nabla\mathbf{u}:(\nabla\rho\otimes\nabla\rho)\,\mathrm{d}x
\tag{5.91}
$$

$$
= \int_\Omega 2e\delta^2\tilde{\nu}(\dot{\rho} + \mathbf{u}\cdot\nabla\rho) - \mathbf{u}\cdot\nabla\cdot(2e\delta^2\nabla\rho\otimes\nabla\rho)\,\mathrm{d}x,
\tag{5.92}
$$

and

$$
\int_\Omega e(\dot{\tilde{f}}_2 + \mathbf{u} \cdot \nabla \tilde{f}_2) \, \mathrm{d}x = \delta^4 \int_\Omega - \tilde{\nu}^2(\dot{e} + \mathbf{u} \cdot \nabla e) + \tilde{\nu}\nabla \cdot (\dot{e}\nabla\rho) + \tilde{\nu}\mathbf{u} \cdot \nabla \cdot (\nabla\rho \otimes \nabla e)
$$
$$
+ \tilde{\nu}\nabla \cdot (e\nabla\dot{\rho}) + \tilde{\nu}\mathbf{u} \cdot \nabla \cdot (e\nabla\nabla\rho) \, \mathrm{d}x \tag{5.93}
$$
$$
= \delta^4 \int_\Omega - \tilde{\nu}^2(\dot{e} + \mathbf{u} \cdot \nabla e) - (\nabla\tilde{\nu} \cdot \nabla\rho)\dot{e} - e\nabla\tilde{\nu} \cdot \nabla\dot{\rho}
$$
$$
+ \tilde{\nu}\mathbf{u} \cdot \nabla \cdot (\nabla(e\nabla\rho)^T) \, \mathrm{d}x \tag{5.94}
$$
$$
= \delta^4 \int_\Omega - \tilde{\nu}^2(\dot{e} + \mathbf{u} \cdot \nabla e) - (\nabla\tilde{\nu} \cdot \nabla\rho)\dot{e} + \nabla \cdot (e\nabla\tilde{\nu})\dot{\rho} \tag{5.95}
$$
$$
+ \tilde{\nu}\mathbf{u} \cdot \nabla \cdot (\nabla(e\nabla\rho))^T \, \mathrm{d}x. \tag{5.96}
$$

Now, we can use that

$$
\tilde{\nu}\mathbf{u} \cdot \nabla \cdot (\nabla(e\nabla\rho))^T = \mathbf{u} \cdot \nabla \cdot (\tilde{\nu}\nabla(e\nabla\rho))^T - \mathbf{u} \cdot \nabla(e\nabla\rho) \cdot \nabla\tilde{\nu} \tag{5.97}
$$
$$
= \mathbf{u} \cdot \nabla \cdot (\tilde{\nu}\nabla(e\nabla\rho))^T - \mathbf{u} \cdot \nabla e\nabla\tilde{\nu} \cdot \nabla\rho - e\mathbf{u} \cdot \nabla\nabla\rho \cdot \nabla\tilde{\nu} \tag{5.98}
$$
$$
= \mathbf{u} \cdot \nabla \cdot (\tilde{\nu}\nabla(e\nabla\rho))^T - \mathbf{u} \cdot \nabla e\nabla\tilde{\nu} \cdot \nabla\rho - \mathbf{u} \cdot \nabla \cdot (e\nabla\tilde{\nu} \otimes \nabla\rho)
$$
$$
+ \nabla \cdot (e\nabla\tilde{\nu})\mathbf{u} \cdot \nabla\rho \tag{5.99}
$$
$$
= \mathbf{u} \cdot \nabla \cdot (\nabla(\tilde{\nu}e\nabla\rho))^T - \mathbf{u} \cdot \nabla \cdot (e\nabla\rho \otimes \nabla\tilde{\nu}) - \mathbf{u} \cdot \nabla e\nabla\tilde{\nu} \cdot \nabla\rho
$$
$$
- \mathbf{u} \cdot \nabla \cdot (e\nabla\tilde{\nu} \otimes \nabla\rho) + \nabla \cdot (e\nabla\tilde{\nu})\mathbf{u} \cdot \nabla\rho \tag{5.100}
$$
$$
= \mathbf{u} \cdot \nabla(\nabla \cdot (\tilde{\nu}e\nabla\rho)) - \mathbf{u} \cdot \nabla \cdot (e\nabla\rho \otimes \nabla\tilde{\nu}) - \mathbf{u} \cdot \nabla e\nabla\tilde{\nu} \cdot \nabla\rho
$$
$$
- \mathbf{u} \cdot \nabla \cdot (e\nabla\tilde{\nu} \otimes \nabla\rho) + \nabla \cdot (e\nabla\tilde{\nu})\mathbf{u} \cdot \nabla\rho. \tag{5.101}
$$

Inserting Eq. (5.101) into Eq. (5.96) yields

$$
\int_\Omega e(\dot{\tilde{f}}_2 + \mathbf{u} \cdot \nabla \tilde{f}_2) \, \mathrm{d}x = \delta^4 \int_\Omega - (\tilde{\nu}^2 + \nabla\tilde{\nu} \cdot \nabla\rho)(\dot{e} + \mathbf{u} \cdot \nabla e) + \nabla \cdot (e\nabla\tilde{\nu})(\dot{\rho} + \mathbf{u} \cdot \nabla\rho)
$$
$$
- \mathbf{u} \cdot \nabla \cdot (e\nabla\tilde{\nu} \otimes \nabla\rho + e\nabla\rho \otimes \nabla\tilde{\nu}) \, \mathrm{d}x. \tag{5.102}
$$

Now, let us put Eqs. (5.89), (5.92) and (5.102) together to get

$$
\int_\Omega e(\dot{\tilde{f}} + \mathbf{u} \cdot \nabla \tilde{f}) \, \mathrm{d}x = \int_\Omega - \delta^4(\tilde{\nu}^2 + \nabla\tilde{\nu} \cdot \nabla\rho)(\dot{e} + \mathbf{u} \cdot \nabla e) \tag{5.103}
$$
$$
+ e(\dot{\rho} + \mathbf{u} \cdot \nabla\rho)\left(\rho^3 + (1+r)\rho + 2\delta^2\tilde{\nu} + \frac{\delta^4}{e}\nabla \cdot (e\nabla\tilde{\nu})\right)
$$
$$
- \mathbf{u} \cdot \nabla \cdot (2\delta^2 e\nabla\rho \otimes \nabla\rho + \delta^4 e\nabla\tilde{\nu} \otimes \nabla\rho + \delta^4 e\nabla\rho \otimes \nabla\tilde{\nu}) \, \mathrm{d}x.
$$

We can insert Eq. (5.103) into Eq. (5.88) which gives

$$
\dot{\tilde{E}}_{spfc} = \int_\Omega \frac{El^{-1}}{\epsilon}(\tilde{f} - \delta^4\tilde{\nu}^2 - \delta^4\nabla\tilde{\nu}\cdot\nabla\rho)(\dot{e} + \mathbf{u}\cdot\nabla e)
$$
$$
+ e(\dot{\rho} + \mathbf{u}\cdot\nabla\rho)\frac{\delta\tilde{E}}{\delta\rho} \tag{5.104}
$$
$$
- \frac{El^{-1}}{\epsilon}\mathbf{u}\cdot\nabla\cdot(2\delta^2 e\nabla\rho\otimes\nabla\rho + \delta^4 e\nabla\tilde{\nu}\otimes\nabla\rho + \delta^4 e\nabla\rho\otimes\nabla\tilde{\nu})\,\mathrm{d}x,
$$

where we have introduced

$$
\frac{\delta\tilde{E}}{\delta\rho} := \frac{El^{-1}}{\epsilon}\left(\rho^3 + (1+r)\rho + 2\delta^2\tilde{\nu} + \frac{\delta^4}{e}\nabla\cdot(e\nabla\tilde{\nu})\right). \tag{5.105}
$$

Note, that the notation $\frac{\delta\tilde{E}}{\delta\rho}$ makes sense, since the material derivative of ρ is multiplied with this term in the energy time derivative. Now, let us insert the evolution equation for ρ from Eq. (5.79). We obtain

$$
\dot{\tilde{E}}_{spfc} = \int_\Omega \left[\frac{El^{-1}}{\epsilon}\left(\tilde{f} - \delta^4\tilde{\nu}^2 - \delta^4\nabla\tilde{\nu}\cdot\nabla\rho\right) - \frac{\delta\tilde{E}}{\delta\rho}(\rho + \tilde{\rho})\right](\dot{e} + \mathbf{u}\cdot\nabla e)
$$
$$
- \frac{\delta\tilde{E}}{\delta\rho}\nabla\cdot\mathbf{J}_\rho \tag{5.106}
$$
$$
- \frac{El^{-1}}{\epsilon}\mathbf{u}\cdot\nabla\cdot(2\delta^2 e\nabla\rho\otimes\nabla\rho + \delta^4 e\nabla\tilde{\nu}\otimes\nabla\rho + \delta^4 e\nabla\rho\otimes\nabla\tilde{\nu})\,\mathrm{d}x.
$$

By analogy with Eq. (5.105) we may also define the notation $\frac{\delta\tilde{E}}{\delta e}$ by

$$
\frac{\delta\tilde{E}}{\delta e} := \frac{El^{-1}}{\epsilon}\left(\tilde{f} - \delta^4\tilde{\nu}^2 - \delta^4\nabla\tilde{\nu}\cdot\nabla\rho\right) - \frac{\delta\tilde{E}}{\delta\rho}(\rho + \tilde{\rho}). \tag{5.107}
$$

It remains to evaluate the material derivative of e. Using (5.77) we may calculate

$$
\dot{e} = -\frac{1}{2}B'(\psi)\nabla\psi\cdot\mathbf{u} - \frac{\epsilon^2}{2}\nabla\psi\cdot\nabla\nabla\psi\cdot\mathbf{u} - \frac{\epsilon^2}{2}\nabla\psi\cdot\nabla\mathbf{u}\cdot\nabla\psi
$$
$$
- \left(\frac{1}{2}B'(\psi) + \frac{\epsilon^2}{2}\nabla\psi\cdot\nabla\right)\nabla\cdot\tilde{\mathbf{J}}_\psi \tag{5.108}
$$
$$
= -\mathbf{u}\cdot\nabla e - \frac{\epsilon^2}{2}\nabla\psi\otimes\nabla\psi : \nabla\mathbf{u} - \left(\frac{1}{2}B'(\psi) + \frac{\epsilon^2}{2}\nabla\psi\cdot\nabla\right)\nabla\cdot\tilde{\mathbf{J}}_\psi. \tag{5.109}
$$

Inserting Eq. (5.109) into Eq. (5.106) yields

$$
\begin{aligned}
\dot{\tilde{E}}_{spfc} = \int_{\Omega} & -\frac{\delta \tilde{E}}{\delta e}\left(\frac{1}{2}B'(\psi) + \frac{\epsilon^2}{2}\nabla\psi \cdot \nabla\right)\nabla \cdot \tilde{\mathbf{J}}_{\psi} \\
& -\nabla \cdot \tilde{\mathbf{J}}_{\rho}\frac{\delta \tilde{E}}{\delta \rho} \\
& -\frac{El^{-1}}{\epsilon}\mathbf{u} \cdot \nabla \cdot (2\delta^2 e \nabla\rho \otimes \nabla\rho + \delta^4 e \nabla\tilde{\nu} \otimes \nabla\rho + \delta^4 e \nabla\rho \otimes \nabla\tilde{\nu}) \\
& +\mathbf{u} \cdot \nabla \cdot \left(\frac{\epsilon^2}{2}\frac{\delta \tilde{E}}{\delta e}\nabla\psi \otimes \nabla\psi\right)\ \mathrm{d}x.
\end{aligned}
\tag{5.110}
$$

Now, let us put the kinetic energy, the SPFC energy and the surface energy together to obtain the time derivative of the total energy:

$$
\begin{aligned}
\dot{\tilde{E}} = & -\int_{\Omega}\frac{1}{Re}\nabla\mathbf{u} : \nabla\mathbf{u}\ \mathrm{d}x \\
& +\int_{\Omega}-\left(\frac{\delta \tilde{E}}{\delta e} + \frac{2}{\epsilon}\right)\left(\frac{1}{2}B'(\psi) + \frac{\epsilon^2}{2}\nabla\psi \cdot \nabla\right)\nabla \cdot \tilde{\mathbf{J}}_{\psi}\ \mathrm{d}x \\
& +\int_{\Omega}-\nabla \cdot \tilde{\mathbf{J}}_{\rho}\frac{\delta \tilde{E}}{\delta \rho}\ \mathrm{d}x \\
& +\int_{\Omega}\mathbf{u} \cdot \left(\tilde{\mathbf{F}} - \nabla \cdot \mathbf{T}_{sing}\right)\ \mathrm{d}x,
\end{aligned}
\tag{5.111}
$$

where we have introduced the singular stress tensor

$$
\begin{aligned}
\mathbf{T}_{sing} = & \frac{El^{-1}}{\epsilon}e\left(2\delta^2\nabla\rho \otimes \nabla\rho + \delta^4\nabla\tilde{\nu} \otimes \nabla\rho + \delta^4\nabla\rho \otimes \nabla\tilde{\nu}\right) \\
& -\epsilon\nabla\psi \otimes \nabla\psi\left(1 + \frac{\epsilon}{2}\frac{\delta \tilde{E}}{\delta e}\right).
\end{aligned}
\tag{5.112}
$$

Integrating by parts gives

$$
\begin{aligned}
\dot{\tilde{E}} = & -\int_{\Omega}\frac{1}{Re}\nabla\mathbf{u} : \nabla\mathbf{u}\ \mathrm{d}x \\
& +\int_{\Omega}\tilde{\mathbf{J}}_{\psi} \cdot \nabla\left(\mu\left[\frac{\epsilon}{2}\frac{\delta \tilde{E}}{\delta e} + 1\right] - \frac{\epsilon^2}{2}\nabla\frac{\delta \tilde{E}}{\delta e} \cdot \nabla\psi\right)\ \mathrm{d}x \\
& +\int_{\Omega}\tilde{\mathbf{J}}_{\rho} \cdot \nabla\frac{\delta \tilde{E}}{\delta \rho}\ \mathrm{d}x \\
& +\int_{\Omega}\mathbf{u} \cdot \left(\tilde{\mathbf{F}} - \nabla \cdot \mathbf{T}_{sing}\right)\ \mathrm{d}x.
\end{aligned}
\tag{5.113}
$$

By taking

$$\tilde{\mathbf{F}} = \nabla \cdot \mathbf{T}_{sing}, \tag{5.114}$$

$$\tilde{\mathbf{J}}_\psi = - Pe_\psi^{-1} \epsilon B \nabla \left(\mu \left[\frac{\epsilon}{2} \frac{\delta \tilde{E}}{\delta e} + 1 \right] - \frac{\epsilon^2}{2} \nabla \frac{\delta \tilde{E}}{\delta e} \cdot \nabla \psi \right), \tag{5.115}$$

$$\tilde{\mathbf{J}}_\rho = - Pe_\rho^{-1} \epsilon e \nabla \frac{\delta \tilde{E}}{\delta \rho}, \tag{5.116}$$

we obtain $\dot{\tilde{E}} \leq 0$, which ensures thermodynamic consistency.

If the flux $\tilde{\mathbf{J}}_\psi$ as defined in Eq. (5.115) is used in the conservation equation (5.77), the resulting ψ does not provide a good description of the interface layer because of the contributions of $\tilde{E}_{spfc}$ to the variational derivatives. To be more precise, the factor of the Cahn-Hilliard chemical potential, $\frac{\epsilon}{2} \frac{\delta \tilde{E}}{\delta e} + 1$, may be negative if El^{-1} is large, which results in a negative Cahn-Hilliard mobility. Since the primary purpose of ψ is to track the two-phase interface, we simplify $\tilde{\mathbf{J}}_\psi$ and omit the terms dependent on $\tilde{E}_{spfc}$, which gives the standard Cahn-Hilliard flux

$$\tilde{\mathbf{J}}_\psi = - Pe_\psi^{-1} \epsilon B(\psi) \nabla \frac{\delta E_\sigma}{\delta \psi} = - Pe_\psi^{-1} \epsilon B \nabla \mu. \tag{5.117}$$

Although the resulting system is no longer variational and does not necessarily decrease the energy, this effect tends to be higher order since away from the interface $B(\psi) \approx 0$ and near the interface ψ locally equilibrates yielding $B'(\psi) - \epsilon^2 \Delta \psi \approx 0$. Note that if $\tilde{\mathbf{J}}_\psi \approx 0$, then $\dot{\tilde{E}} \leq 0$ with $\mathbf{F}$ and $\tilde{\mathbf{J}}_\rho$ given in Eqs. (5.114) and (5.116). In addition, we will show in Sec. 5.7 that the system we obtained above is the diffuse interface version of a thermodynamically consistent sharp interface system, and in this sense remains variational.

5.6.2   Summary of governing equations

Putting everything together, we now summarize the new nondimensional Navier-Stokes-Cahn-Hilliard-Surface-Phase-Field-Crystal (NSCHSPFC) equations. We write the equations as a system of 2nd order partial differential equations. The advective Cahn-Hilliard equation governing the motion of the two-phase interface remains unchanged, but is repeated here for completeness:

$$\partial_t \psi + \mathbf{u} \cdot \nabla \psi = Pe_\psi^{-1} \epsilon \nabla \cdot (B(\psi) \nabla \mu), \tag{5.118}$$

$$\mu = \epsilon^{-1} B'(\psi) - \epsilon \Delta \psi. \tag{5.119}$$

The new Surface Phase-Field-Crystal equation on the diffuse interface is given by

$$\partial_t (e(\rho + \tilde{\rho})) + \nabla \cdot (e\mathbf{u}(\rho + \tilde{\rho})) = Pe_\rho^{-1} \nabla \cdot (e\nabla \tilde{\omega}), \tag{5.120}$$

$$e\tilde{\omega} = e\rho \left(\rho^2 + 1 + r \right) + 2\delta^2 e\tilde{\nu} + \delta^4 \nabla \cdot (e\nabla \tilde{\nu}), \tag{5.121}$$

$$e\tilde{\nu} = \nabla \cdot (e\nabla \rho). \tag{5.122}$$

Finally, the Navier-Stokes equations govern the motion of the fluids:

$$\partial_t \mathbf{u} + (\mathbf{u} \cdot \nabla)\mathbf{u} = -\nabla p + \frac{1}{Re}\Delta \mathbf{u} + \nabla \cdot \mathbf{T}_{sing}, \tag{5.123}$$

$$\nabla \cdot \mathbf{u} = 0, \tag{5.124}$$

where the surface tension and elastic force are contained in the singular stress tensor $\mathbf{T}_{sing}$ defined in Eqs. (5.112), (5.107), (5.105). The NSCHSPFC system is equipped with the initial conditions

$$\mathbf{u}(t=0,\mathbf{x}) = \mathbf{u}_0(\mathbf{x}), \ \ \psi(t=0,\mathbf{x}) = \psi_0(\mathbf{x}), \ \ \rho(t=0,\mathbf{x}) = \rho_0(\mathbf{x}), \quad \text{in } \Omega$$

and either natural boundary conditions

$$\frac{\delta\psi}{\delta\mathbf{n}} = \frac{\delta\rho}{\delta\mathbf{n}} = \frac{\delta\mu}{\delta\mathbf{n}} = \frac{\delta\tilde{\nu}}{\delta\mathbf{n}} = \frac{\delta\tilde{\omega}}{\delta\mathbf{n}} = 0, \qquad \mathbf{u} = \mathbf{u}_\infty \quad \text{on } \delta\Omega,$$

where $\mathbf{n}$ denotes the outward normal vector, or periodic boundary conditions.

5.6.3 Evaluating the divergence of the stress tensor

In this section we will evaluate the divergence of the stress tensor $\mathbf{T}_{sing}$ to obtain further insight into the force $\tilde{\mathbf{F}}$. This will enable a straightforward comparison with the sharp interface analogue given in Sec. 5.7. Moreover, we will see that $\tilde{\mathbf{F}}$ includes the new elastic force $\mathbf{F}_{new}$. First, one may easily verify that

$$\frac{El^{-1}}{\epsilon}\nabla \cdot \left[e \left(2\delta^2 \nabla\rho \otimes \nabla\rho + \delta^4 \nabla\tilde{\nu} \otimes \nabla\rho + \delta^4 \nabla\rho \otimes \nabla\tilde{\nu} \right) \right]$$

$$= e \left(\frac{\delta\tilde{E}}{\delta\rho}\nabla\rho - \nabla\left[\frac{\delta\tilde{E}}{\delta e} + \frac{\delta\tilde{E}}{\delta\rho}(\rho + \tilde{\rho}) \right] \right) \tag{5.125}$$

and

$$-\nabla \cdot \left[\epsilon\nabla\psi \otimes \nabla\psi \left(1 + \frac{\epsilon}{2}\frac{\delta\tilde{E}}{\delta e} \right) \right] = -\epsilon\nabla\left(1 + \frac{\epsilon}{2}\frac{\delta\tilde{E}}{\delta e} \right) \cdot \nabla\psi \otimes \nabla\psi$$

$$-\epsilon\left(1 + \frac{\epsilon}{2}\frac{\delta\tilde{E}}{\delta e} \right)(\Delta\psi\nabla\psi + \nabla\psi \cdot \nabla\nabla\psi) \tag{5.126}$$

$$= -\epsilon\nabla\left(1 + \frac{\epsilon}{2}\frac{\delta\tilde{E}}{\delta e} \right) \cdot \nabla\psi \otimes \nabla\psi$$

$$+ \left(1 + \frac{\epsilon}{2}\frac{\delta\tilde{E}}{\delta e} \right)\left(\mu\nabla\psi - \frac{2}{\epsilon}\nabla e \right). \tag{5.127}$$

Adding both gives

$$\tilde{\mathbf{F}} = \nabla \cdot \mathbf{T}_{sing} = -\nabla \left(e \left[\frac{2}{\epsilon} + \frac{\delta \tilde{E}}{\delta e} \right] \right) - e(\rho + \tilde{\rho}) \nabla \frac{\delta \tilde{E}}{\delta \rho}$$

$$- \frac{\epsilon^2}{2} \nabla \psi \otimes \nabla \psi \cdot \nabla \frac{\delta \tilde{E}}{\delta e} + \left(1 + \frac{\epsilon}{2} \frac{\delta \tilde{E}}{\delta e} \right) \mu \nabla \psi. \tag{5.128}$$

The first term on the RHS is a gradient term and can therefore be neglected as it does not affect the flow profile (e.g., modifies the pressure). We will drop the term and note this by using equivalent ($\equiv$) instead of equal ($=$) in the following. Therefore, we have

$$\tilde{\mathbf{F}} \equiv - e(\rho + \tilde{\rho}) \nabla \frac{\delta \tilde{E}}{\delta \rho} - \frac{\epsilon^2}{2} \nabla \psi \otimes \nabla \psi \cdot \nabla \frac{\delta \tilde{E}}{\delta e} + \left(1 + \frac{\epsilon}{2} \frac{\delta \tilde{E}}{\delta e} \right) \mu \nabla \psi. \tag{5.129}$$

Now, examine $\nabla \psi \cdot \nabla \frac{\delta \tilde{E}}{\delta e}$. First, we may use that ρ, $\tilde{\nu}$ and $\frac{\delta \tilde{E}}{\delta \rho}$ are to highest order constant in normal direction and $\nabla \psi$ is normal to the interface. This allows the approximation

$$\nabla \psi \cdot \nabla \frac{\delta \tilde{E}}{\delta e} \approx \frac{El^{-1}}{\epsilon} \nabla \psi \cdot \nabla \left(-\delta^2 |\nabla \rho|^2 - \delta^4 \nabla \tilde{\nu} \cdot \nabla \rho \right) \tag{5.130}$$

$$= - \frac{El^{-1}}{\epsilon} \left(2\delta^2 \nabla \psi \cdot \nabla \nabla \rho \cdot \nabla \rho + \delta^4 \nabla \psi \cdot \nabla \nabla \rho \cdot \nabla \tilde{\nu} + \delta^4 \nabla \psi \cdot \nabla \nabla \tilde{\nu} \cdot \nabla \rho \right)$$

$$= - \frac{El^{-1}}{\epsilon} \left(2\delta^2 \nabla (\nabla \psi \cdot \nabla \rho) \cdot \nabla \rho - 2\delta^2 \nabla \rho \cdot \nabla \nabla \psi \cdot \nabla \rho \right. \tag{5.131}$$

$$\left. + \delta^4 \nabla (\nabla \psi \cdot \nabla \rho) \cdot \nabla \tilde{\nu} + \delta^4 \nabla (\nabla \psi \cdot \nabla \tilde{\nu}) \cdot \nabla \rho - 2\delta^4 \nabla \rho \cdot \nabla \nabla \psi \cdot \nabla \tilde{\nu} \right)$$

$$\approx \frac{El^{-1}}{\epsilon} \left(2\delta^2 \nabla \rho \cdot \nabla \nabla \psi \cdot \nabla \rho + 2\delta^4 \nabla \rho \cdot \nabla \nabla \psi \cdot \nabla \tilde{\nu} \right) \tag{5.132}$$

$$\approx \frac{El^{-1}}{\epsilon} \left(2\delta^2 |\nabla \rho|^2 + 2\delta^4 \nabla \tilde{\nu} \cdot \nabla \rho \right) \mathbf{t} \cdot \nabla \nabla \psi \cdot \mathbf{t}, \tag{5.133}$$

where

$$\mathbf{t} := \frac{\nabla \rho}{|\nabla \rho|} \approx \frac{\nabla \tilde{\nu}}{|\nabla \tilde{\nu}|} \tag{5.134}$$

denotes the unit tangent vector. From differential geometry (e.g. see [Har99]) it is known that

$$\mathbf{t} \cdot \nabla \nabla \psi \cdot \mathbf{t} = \kappa_{\mathbf{t}} |\nabla \psi|, \tag{5.135}$$

where $\kappa_{\mathbf{t}}$ is the normal curvature of the interface along $\mathbf{t}$. In the following, we will restrict ourselves to 2D, where $\kappa_{\mathbf{t}} = \kappa$. Inserting Eq. (5.135) into Eq. (5.133), we can write

$$\frac{\epsilon^2}{2} \nabla \psi \otimes \nabla \psi \cdot \nabla \frac{\delta \tilde{E}}{\delta e} \approx \frac{El^{-1}}{2} \epsilon \nabla \psi |\nabla \psi| \kappa \left(2\delta^2 |\nabla \rho|^2 + 2\delta^4 \nabla \tilde{\nu} \cdot \nabla \rho \right). \tag{5.136}$$

Now, we can use the fact that $\nabla\psi = \mathbf{n}|\nabla\psi|$ and that $3\sqrt{2}\epsilon|\nabla\psi|^2$ approximates the surface delta function for $\epsilon \to 0$ and deduce

$$\frac{\epsilon^2}{2}\nabla\psi \otimes \nabla\psi \cdot \nabla\frac{\delta\tilde{E}}{\delta e} \approx \frac{El^{-1}}{2}\frac{1}{3\sqrt{2}}\delta_\Gamma \kappa \mathbf{n}\left(2\delta^2|\nabla\rho|^2 + 2\delta^4\nabla\tilde{\nu}\cdot\nabla\rho\right). \tag{5.137}$$

Finally, using Eq. (2.30), we obtain

$$\frac{\epsilon^2}{2}\nabla\psi \otimes \nabla\psi \cdot \nabla\frac{\delta\tilde{E}}{\delta e} \approx -\frac{El^{-1}}{2}\mu\nabla\psi\left(2\delta^2|\nabla\rho|^2 + 2\delta^4\nabla\tilde{\nu}\cdot\nabla\rho\right). \tag{5.138}$$

This can be inserted into Eq. (5.129) to give

$$\begin{aligned}\tilde{\mathbf{F}} \cong &-e(\rho+\tilde{\rho})\nabla\frac{\delta\tilde{E}}{\delta\rho} - \frac{\epsilon}{2}\mu\nabla\psi\frac{\delta\tilde{E}}{\delta\rho}(\rho+\tilde{\rho}) + \mu\nabla\psi \\ &+ \frac{El^{-1}}{2}\mu\nabla\psi\left(\frac{1}{4}\rho^4 + \frac{1+r}{2}\rho^2 - \frac{\delta^4}{2}\tilde{\nu}^2 + \delta^2|\nabla\rho|^2 + \delta^4\nabla\tilde{\nu}\cdot\nabla\rho\right).\end{aligned} \tag{5.139}$$

Examining the last term on the RHS, we recover the (new) elastic force $\mathbf{F}_{new}$ derived in Sec. 5.5. Also, the third term, $\mu\nabla\psi$, occurred in the original equations, but the first and second terms in $\tilde{\mathbf{F}}$ differ from the original NSCHSPFC model from Sec. 5.2. This is due to the fact that in the derivation of the NSCHSPFC model in Sec. 5.2, the assumption of conserved dynamics led to an additional term in the Cahn-Hilliard chemical potential rather than in the force $\tilde{\mathbf{F}}$ and was dropped, since it led to a poor description of the interface. If in the derivation of the model we had neglected the conservation of $\rho+\tilde{\rho}$ as well, that is, if we had assumed the evolution of ρ to be given by

$$e\frac{\partial}{\partial t}\rho = -e\nabla\cdot(\mathbf{u}\rho) - \nabla\cdot\tilde{\mathbf{J}}_\rho \tag{5.140}$$

instead of Eq. (5.78), we would have obtained

$$\begin{aligned}\tilde{\mathbf{F}} \cong &e\frac{\delta\tilde{E}}{\delta\rho}\nabla\rho + \mu\nabla\psi \\ &+ \frac{El^{-1}}{2}\mu\nabla\psi\left(\frac{1}{4}\rho^4 + \frac{1+r}{2}\rho^2 - \frac{\delta^4}{2}\tilde{\nu}^2 + \delta^2|\nabla\rho|^2 + \delta^4\nabla\tilde{\nu}\cdot\nabla\rho\right),\end{aligned} \tag{5.141}$$

which is the exact same force as derived in the previous section, with B replaced by e. To sum up, the new NSCHSPFC model presented in this section is in 2D equivalent to the original model equipped with the new elastic force and additional terms to account for the conservation of $\rho+\tilde{\rho}$. In the next section we validate the model by demonstrating that the NSCHSPFC model is a diffuse interface approximation of a thermodynamically consistent sharp interface model.

5.7 Sharp interface model

In this section we derive a 2D sharp interface version of the NSCHSPFC model which we will call Navier-Stokes-Surface-Phase-Field-Crystal (NSSPFC) model. A similar calculation can be done in 3D, but involves more complicated differential geometry, e.g. see [ARRV12], where the variational derivatives of the sharp interface surface PFC energy are computed. For the derivation here we use a one-dimensional parametrization of the interface and we demonstrate that the NSCHSPFC model derived in the previous section is a diffuse interface approximation of the NSSPFC model.

In the following let us denote the arc length by s and the derivative along the interface with subscript s. We derive the NSSPFC model following the ideas in [ALV11] but replacing the total energy E with its sharp interface analogue

$$\bar{E} = \bar{E}_{spfc} + \bar{E}_{\sigma} + E_{kin}, \tag{5.142}$$

where

$$\bar{E}_{spfc} = \frac{E l^{-1}}{6\sqrt{2}} \int_{\Gamma} \bar{f} \mathrm{d}s, \tag{5.143}$$

with

$$\bar{f} = \frac{1}{4}\rho^4 + \frac{1+r}{2}\rho^2 - \delta^2 \rho_s^2 + \frac{\delta^4}{2}\rho_{ss}^2, \tag{5.144}$$

$$\tag{5.145}$$

and

$$\bar{E}_{\sigma} = \int_{\Gamma} \frac{1}{3\sqrt{2}} \mathrm{d}s, \tag{5.146}$$

are the sharp interface versions of E_{spfc} and E_{σ}, respectively. The factors $6\sqrt{2}$ and $3\sqrt{2}$ arise to match the scaling according to Eqs.(5.4) and (2.2). Now, we can parametrize the interface with a real-valued parameter $\alpha \in [0, 1]$ and write

$$\bar{E} = \frac{E l^{-1}}{6\sqrt{2}} \int_0^1 \bar{f} s_\alpha \mathrm{d}\alpha + \int_0^1 \frac{1}{3\sqrt{2}} s_\alpha \mathrm{d}\alpha + E_{kin}. \tag{5.147}$$

To vary Γ and ρ we take the time derivative of $\bar{E}$,

$$\frac{\mathrm{d}}{\mathrm{d}t}\bar{E} = \frac{E l^{-1}}{6\sqrt{2}} \int_0^1 \dot{\bar{f}} s_\alpha + \bar{f} \partial_t s_\alpha \mathrm{d}\alpha + \int_0^1 \frac{1}{3\sqrt{2}} \partial_t s_\alpha \mathrm{d}\alpha + \frac{\mathrm{d}}{\mathrm{d}t}E_{kin}, \tag{5.148}$$

where the overdot denotes the material derivative $\partial_t + \mathbf{u} \cdot \nabla$. Now, we can use that

$$\partial_t s_\alpha = s_\alpha(T_s + \kappa V), \tag{5.149}$$

where T is the tangential and V the normal velocity. We get

$$\frac{\mathrm{d}}{\mathrm{d}t}\bar{E} = \int_0^1 \frac{El^{-1}}{6\sqrt{2}} \left(\dot{\bar{f}} s_\alpha + \bar{f} s_\alpha (T_s + \kappa V)\right) + \frac{1}{3\sqrt{2}} s_\alpha (T_s + \kappa V)\mathrm{d}\alpha + \frac{\mathrm{d}}{\mathrm{d}t} E_{kin}$$
$$= \int_\Gamma \frac{El^{-1}}{6\sqrt{2}} \left(\dot{\bar{f}} + \bar{f}(T_s + \kappa V)\right) + \frac{1}{3\sqrt{2}}\kappa V \mathrm{d}s + \frac{\mathrm{d}}{\mathrm{d}t} E_{kin}. \tag{5.150}$$

Furthermore, we compute

$$\int_\Gamma \dot{\bar{f}} \mathrm{d}s = \int_\Gamma (\rho^3 + (1+r)\rho)\dot{\rho} - 2\delta^2 \rho_s \left(\frac{1}{s_\alpha}\rho_\alpha\right)^\cdot + \delta^4 \rho_{ss} \left(\frac{1}{s_\alpha}\left(\frac{1}{s_\alpha}\rho_\alpha\right)_\alpha\right)^\cdot \mathrm{d}s$$
$$= \int_\Gamma (\rho^3 + (1+r)\rho)\dot{\rho} - 2\delta^2 \rho_s \dot{\rho}_s + 2\delta^2 \rho_s \frac{\partial_t s_\alpha}{s_\alpha}\rho_s$$
$$\quad - \delta^4 \rho_{ss}\left(\frac{\partial_t s_\alpha}{s_\alpha}\rho_{ss}\right) + \delta^4 \rho_{ss}\left(\frac{\partial_t s_\alpha}{s_\alpha}\rho_s\right)_s + \delta^4 \rho_{ss}(\dot{\rho})_{ss}\mathrm{d}s$$
$$= \int_\Gamma \dot{\rho}\left(\rho^3 + (1+r)\rho + 2\delta^2 \rho_{ss} + \delta^4 \rho_{ssss}\right)$$
$$\quad + \frac{\partial_t s_\alpha}{s_\alpha}\left(2\delta^2 \rho_s^2 - \delta^4 \rho_{ss}^2 + \delta^4 \rho_{sss}\rho_s\right)\mathrm{d}s. \tag{5.151}$$

Now, let us define

$$\frac{\delta \bar{E}}{\delta \rho} = \frac{El^{-1}}{6\sqrt{2}}\left(\rho^3 + (1+r)\rho + 2\delta^2 \rho_{ss} + \delta^4 \rho_{ssss}\right) \tag{5.152}$$

and

$$\bar{g} := \bar{f} + 2\delta^2 \rho_s^2 - \delta^4 \rho_{ss}^2 + \delta^4 \rho_{sss}\rho_s. \tag{5.153}$$

From Eqs. (5.150), (5.151) and (5.149) we obtain

$$\frac{\mathrm{d}}{\mathrm{d}t}\bar{E} = \int_\Gamma \dot{\rho}\frac{\delta \bar{E}}{\delta \rho} + \frac{El^{-1}}{6\sqrt{2}}(T_s + \kappa V)g\mathrm{d}s + \int_\Gamma \frac{1}{3\sqrt{2}}\kappa V\mathrm{d}s + \frac{\mathrm{d}}{\mathrm{d}t} E_{kin}$$
$$= \int_\Gamma \dot{\rho}\frac{\delta \bar{E}}{\delta \rho} + \frac{El^{-1}}{6\sqrt{2}}\left(\kappa V g - T g_s\right)\mathrm{d}s + \int_\Gamma \frac{1}{3\sqrt{2}}\kappa V\mathrm{d}s + \frac{\mathrm{d}}{\mathrm{d}t} E_{kin}$$
$$= \int_\Gamma \dot{\rho}\frac{\delta \bar{E}}{\delta \rho} + \frac{El^{-1}}{6\sqrt{2}}\kappa V g - T\frac{\delta \bar{E}}{\delta \rho}\rho_s \mathrm{d}s + \int_\Gamma \frac{1}{3\sqrt{2}}\kappa V\mathrm{d}s + \frac{\mathrm{d}}{\mathrm{d}t} E_{kin}. \tag{5.154}$$

Now, we can use that $\frac{\mathrm{d}}{\mathrm{d}t} E_{kin} = \int_\Omega \mathbf{u} \cdot \partial_t \mathbf{u}\mathrm{d}x$ and suppose that the fluid motion is governed by the

Navier-Stokes equation which in nondimensional form is given by

$$\partial_t \mathbf{u} = -\mathbf{u} \cdot \nabla \mathbf{u} - \nabla p + \frac{1}{Re} \Delta \mathbf{u} + \bar{\mathbf{F}}, \quad \nabla \cdot \mathbf{u} = 0 \quad \text{in } \Omega. \tag{5.155}$$

The force $\bar{\mathbf{F}}$ is as yet unspecified. Furthermore, we assume the evolution of ρ as:

$$\dot{\rho} = -\nabla_\Gamma \cdot T(\rho + \tilde{\rho}) - (\rho + \tilde{\rho})\kappa V - \nabla_\Gamma \cdot \bar{\mathbf{J}}_\rho \quad \text{on } \Gamma, \tag{5.156}$$

which ensures conservation of $\rho + \tilde{\rho}$. Also the flux $\bar{\mathbf{J}}_\rho$ has not yet been specified. Now, we can insert Eqs. (5.155) and (5.156) into Eq. (5.154). The time derivative of the energy becomes

$$\begin{aligned}
\frac{\mathrm{d}}{\mathrm{d}t}\bar{E} &= \int_\Omega -\frac{1}{Re}\nabla \mathbf{u} : \nabla \mathbf{u} + \mathbf{u} \cdot \bar{\mathbf{F}} \mathrm{d}x + \int_\Gamma \bar{\mathbf{J}}_\rho \nabla_\Gamma \frac{\delta \bar{E}}{\delta \rho} \mathrm{d}s \\
&\quad + \int_\Gamma \frac{El^{-1}}{6\sqrt{2}}\kappa V g + \frac{1}{3\sqrt{2}}\kappa V - \kappa V(\rho + \tilde{\rho})\frac{\delta \bar{E}}{\delta \rho} + T(\rho + \tilde{\rho})\nabla_\Gamma \frac{\delta \bar{E}}{\delta \rho} \mathrm{d}s \\
&= -\frac{1}{Re}\int_\Omega \nabla \mathbf{u} : \nabla \mathbf{u} \mathrm{d}x + \int_\Gamma \bar{\mathbf{J}}_\rho \nabla_\Gamma \frac{\delta \bar{E}}{\delta \rho} \mathrm{d}s \\
&\quad + \int_\Omega \mathbf{u} \cdot \left(\bar{\mathbf{F}} + \delta_\Gamma \left[\frac{El^{-1}}{6\sqrt{2}}\kappa \mathbf{n} g + \frac{1}{3\sqrt{2}}\kappa \mathbf{n} - \kappa \mathbf{n}(\rho + \tilde{\rho})\frac{\delta \bar{E}}{\delta \rho} \right. \right. \\
&\qquad\qquad\qquad \left.\left. + (\rho + \tilde{\rho})\nabla_\Gamma \frac{\delta \bar{E}}{\delta \rho} \right] \right) \mathrm{d}x.
\end{aligned}$$

Hence, we obtain decreasing energy, $\dot{\bar{E}} \leq 0$, by taking

$$\bar{\mathbf{F}} = -\frac{El^{-1}}{6\sqrt{2}}\delta_\Gamma \kappa \mathbf{n} g - \frac{1}{3\sqrt{2}}\delta_\Gamma \kappa \mathbf{n} + \delta_\Gamma \kappa \mathbf{n}\frac{\delta \bar{E}}{\delta \rho}(\rho + \tilde{\rho}) - \delta_\Gamma(\rho + \tilde{\rho})\nabla_\Gamma \frac{\delta \bar{E}}{\delta \rho}, \tag{5.157}$$

$$\bar{\mathbf{J}}_\rho = -6\sqrt{2}Pe_\rho^{-1}\nabla_\Gamma \frac{\delta E}{\delta \rho}. \tag{5.158}$$

Now, the resulting governing equations for the sharp interface NSSPFC model are Eqs. (5.155) and (5.156) with $\bar{\mathbf{F}}$ and $\bar{\mathbf{J}}_\rho$ from Eqs. (5.157) and (5.158). We can obtain a diffuse interface approximation for $\bar{\mathbf{F}}$ by using Eqs. (2.13) and (2.30) to approximate δ_Γ and $\delta_\Gamma \kappa \mathbf{n}$, respectively. Doing so, we recover the force $\tilde{\mathbf{F}}$ from Eq. (5.139) derived in the previous section with the identifications $\nabla \rho \to \rho_s$, $\tilde{\nu} \to \rho_{ss}$ and $\nabla \tilde{\nu} \to \rho_{sss}$. Furthermore, with $\bar{\mathbf{J}}_\rho$ chosen as in Eq. (5.158) the evolution equation for ρ matches exactly its diffuse interface analogue given in Eq. (5.78). In this sense, the NSCHSPFC system given in Sec. 5.6 is the diffuse interface version of the thermodynamically consistent sharp interface model (5.155)-(5.158) and its generalization to 3D.

5.8 Simulations with the improved system

In this section we test the new model using different flow configurations. The numerical method used is as described in Sec. 5.3 where this time the equations to be solved are (5.118)-(5.124). For the 3D simulations we use an MPI based parallelization with 64 cores and a PETSc solver TFQMR (transpose-

free quasi-minimal residual) with the block Jacobi preconditioner. The local subproblems are solved using incomplete LU factorization [VWed].

5.8.1 Retracting ellipse

As a first test for the new NSCHSPFC model we consider the case of an initially elliptical fluid droplet surrounded by another fluid. The test setup and parameters are the same as in Sec. 5.4.1
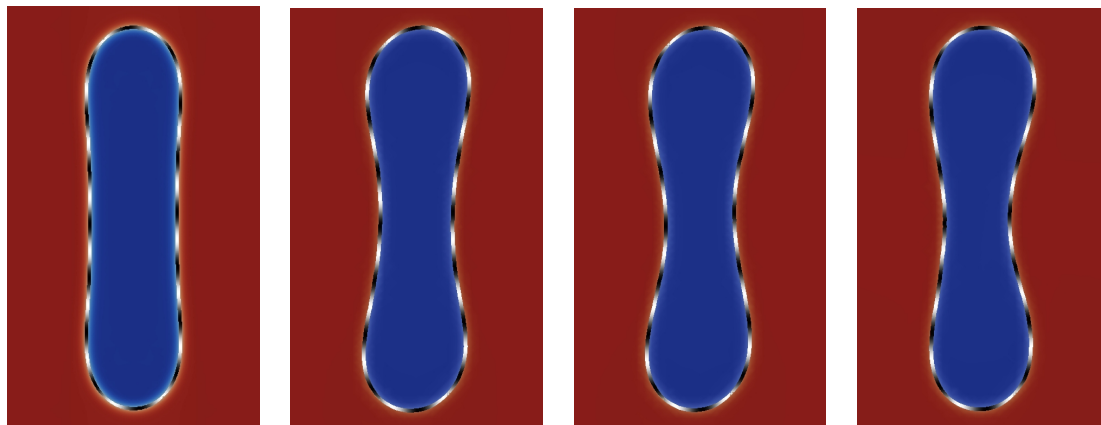

Figure 5.12: Retraction of an elliptical drop with the new elastic force at times $t = 0,33,67,1671$, from left to right. The drop and matrix fluids have different shades, lighter (red online) for $\psi = 1$ and darker (blue online) for $\psi = 0$. The colloids (ρ) on the interface are colored black ($\rho < 0$) and white ($\rho > 0$). Compare with Fig. 5.2.

Fig. 5.12 shows the simulation with the new elastic force. See Fig. 5.2 for a comparison with the old elastic force and without colloids ($El^{-1} = 0$). As we have seen, when no colloids are present the surface tension makes the ellipse retract to become circular. The presence of colloids stops the retraction by the elastic force as the colloids jam at the interface, generating a strong elastic force, and the interface crystallizes. This occurs using both the old and new forms of the elastic force. Driven by the new force, the ellipse starts to develop a neck in the middle, similar to results for elastic membranes. Such results are observed for a Helfrich model with a bending energy under the constraint of local inextensibility, see e.g. [STL⁺10]. The jamming of the colloidal particles in our model effectively leads to such a constraint and the elastic force resulting from the particle interactions might be interpreted as a microscopic origin of the bending energy. These interpretations provide further support for the use of the new forcing term.

In Fig. 5.13 the interface length, calculated by the length of the $\psi = 0.5$ contour, is plotted as a function of time for different strengths of elastic forces. Initially the particles are slightly over compressed, which results in a slight expansion of the elliptical drop. When the elasticity increases (El decreases) this effect increases and the particles can better counteract the surface tension. Furthermore, the old and new formulation of the elastic force lead to different final interface lengths (Fig. 5.13 (a),(e)).

The velocity **u** at the top of the ellipse at early times is shown in Fig. 5.14. For the previous model, the elastic force induces local straining flows around the interface (two per colloid) which restricts
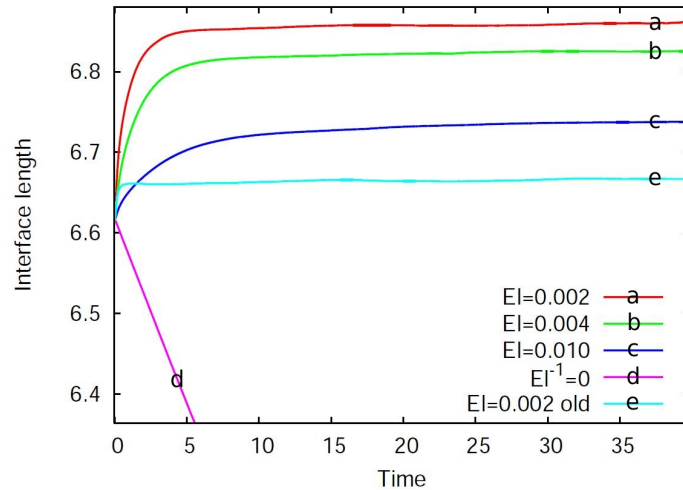
Figure 5.13: The interface length versus time for the new elastic force formulation for different strengths of elastic forces (a)-(d), and for the old elastic force for $El = 0.002$ (e).

the numerical simulations to relatively small time steps and a very fine grid in a neighborhood of the interface. With the new model the straining flows seems to vanish and the velocity is much smoother.

Another non-physical behaviour of the old model is the achievement of a stable, almost stationary state with non-zero velocity. This is a characteristic feature of spurious currents (e.g., [JTB02]). Fig. 5.15(left) shows the kinetic energy of the system as a measure for the total magnitude of the velocity. For the previous model E_{kin} reaches a plateau above zero, whereas with the new model E_{kin} seems to converge to zero versus time. Also the total energy (Fig. 5.15, right) is decreased significantly more when $\mathbf{F}_{new}$ is used instead of $\mathbf{F}_{el}$.

5.8.2   Retracting ellipsoid

A significant benefit of the new formulation is that it requires much less computational power and therefore enables 3D simulations to be performed. We next model an ellipsoidal droplet subject to surface tension with and without colloids at the interface. The computational domain is $\Omega = [-4, 4] \times [-4, 4]$. We create the initial ellipsoid and the initial particle number density in the same way as in Sec. 5.4.1, this time with

$$d = 1.0 - \sqrt{\left(\frac{x}{0.8}\right)^2 + \left(\frac{y}{0.8}\right)^2 + \left(\frac{z}{3.3}\right)^2}.$$

The parameters are $\tau = 1.09$, $Pe_\rho = 12.25$, $Pe_\psi = 0.76$, $Re = 1.23$, $El = 0.025$ and the remaining parameters as before.

Fig. 5.16 shows the simulation without colloids ($El^{-1} = 0$) and with the new elastic force. When no colloids are present the surface tension makes the ellipsoid retract to become a circular. As in the 2D case, the presence of colloids stops the retraction by the elastic force as the colloids jam at the interface and the interface crystallizes. Another interesting effect that did not occure in 2D is that the interface bulges out at some particles. To explain this finding it is useful to look for each particle at the number of neighboring particles. Most particles on the interface have 6 neighbors which agrees with the optimal ordering of equal-sized particles in the plane. But as predicted by Euler's theorem there are also defect
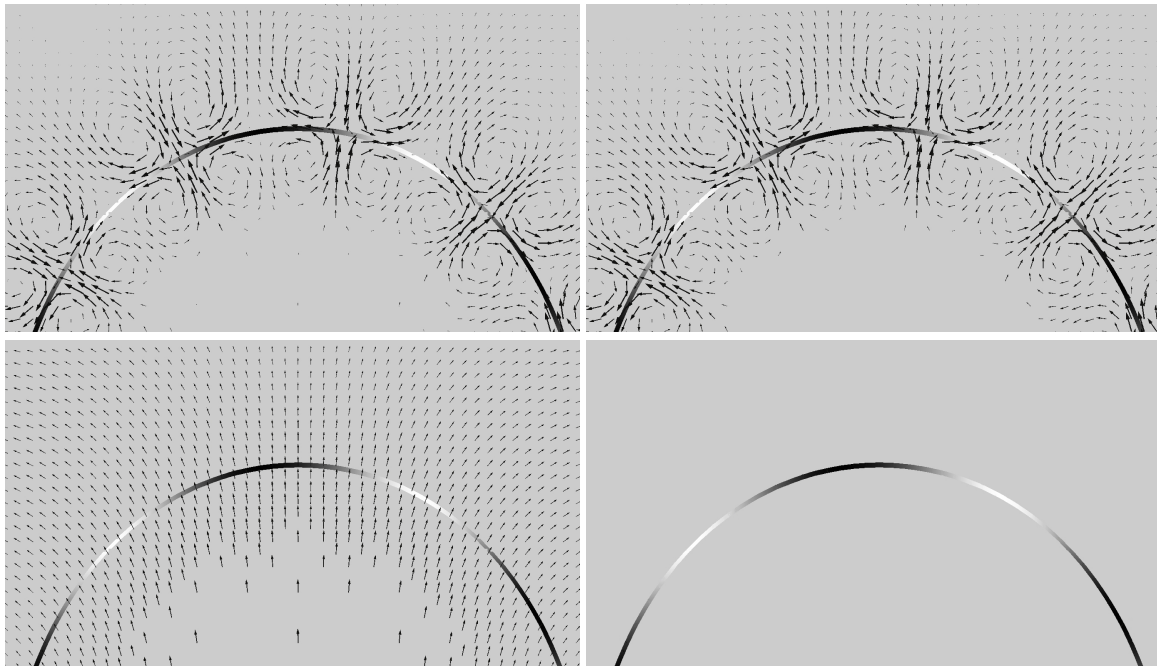
Figure 5.14: Velocity field at the top of the ellipse for the old (top) and new (bottom) formulation of the elastic force at the early time $t = 0.5$ (left) and at $t = 5.0$ (right). The black-white line indicates the interface position. The arrow length indicates the velocity magnitude, for the new formulation at $t = 5.0$ (bottom right) the arrows are too small to be seen.
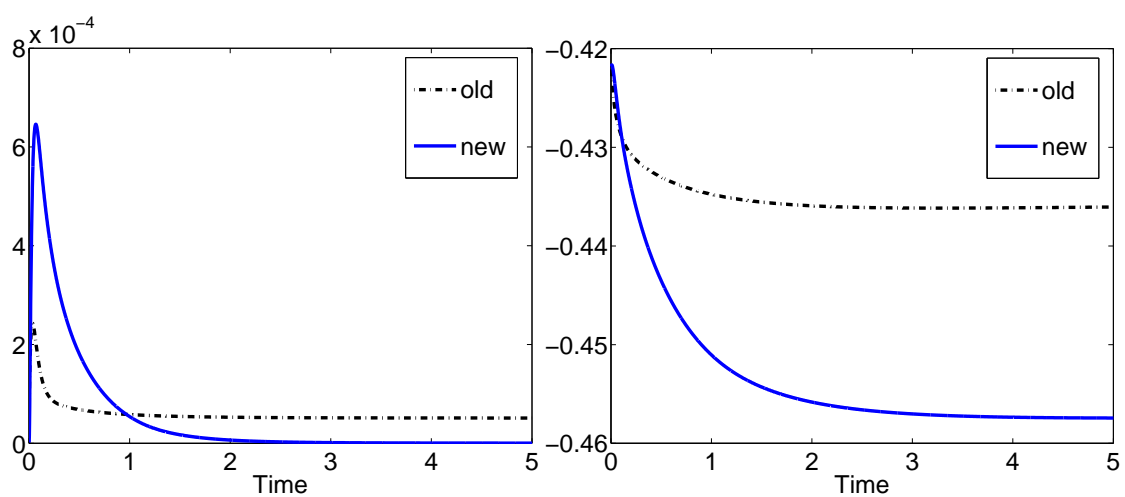
Figure 5.15: The kinetic energy (left) and total energy (right) versus time for the simulations shown in Figs. 5.12, 5.2.
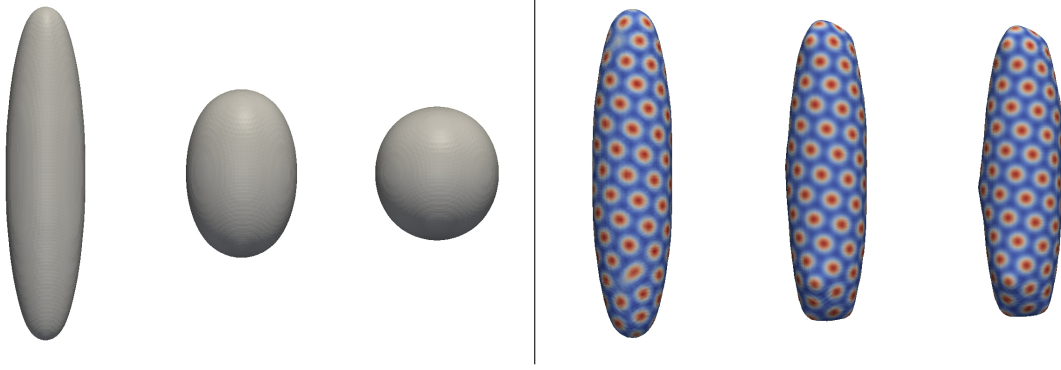
Figure 5.16: The interface of an retracting ellipsoidal drop at times $t = 0, 28, 150$. Left: Without colloidal forces. Right: With the new elastic force, colored by ρ.

particles having only 5 neighbors. These defect particles can minimize their elastic energy by interface buckling, which is what we see in Fig. 5.16. Therefore, our results agree well with observations from nature, e.g. in viral growth [ARRV12].

5.8.3 Jamming spinodal decomposition

Now, we investigate the potential of colloidal particles to stabilize bicontinuous structures generated by spinodal decomposition. The computational domain is $\Omega = [0, 8/3]^3$. As initial condition, we first generate fluid structures via spinodal decomposition by solving the CH equation in the absence of flow ($\mathbf{u} = 0$) using the initial condition $\psi = 0.5 \pm 0.1$ with a large interface thickness $\epsilon = 0.1$ for a few time steps. Then, to generate the initial condition for the full NSCHSPFC system, the CH and SPFC equations are solved together for several more time steps, again in the absence of flow, with $\epsilon = 0.03$ to refine the interface thickness and to create the colloid structure on the complex interface. As initial data for the CHSPFC solver, the previously generated ψ is used together with the colloid density $\rho_0 = -0.3 \pm 0.05$. The resulting ψ, ρ are used as the initial condition ψ_0, ρ_0 for the full NSCHSPFC system. The parameters are the same as in Sec. 5.8.1 with $\tau = 0.067$, $Pe_\psi = 0.23$, $El = 0.005$ and $\tilde{\rho} = -0.3$; periodic boundary conditions are used in each coordinate direction.

Figure 5.17 shows a comparison between the NSCHSPFC model (bottom) and a NSCH model without colloidal forces ($El^{-1} = 0$, top). In the latter case the structure coarsens significantly. When colloids are present, the elastic force induced by the particles is able to prevent the coarsening as the colloids jam and the interface crystallizes. The interface area versus time is plotted in Fig. 5.18.

5.8.4 A ball falling into a fluid structure

Finally, we demonstrate a significant advantage of the multi-scale NSCHSPFC model: The possibility of incorporating additional macroscopic effects. We model a solid ball, under the influence of gravity, falling through a colloid crystallized surface. This involves (1) solving the NSCHSPFC model only in $\Omega \backslash \Omega_{ball}$ and (2) moving the ball with a velocity that takes into account all the forces acting on the ball. For the first part we can apply a diffuse domain approach as done in [ALV10]. We therefore define a
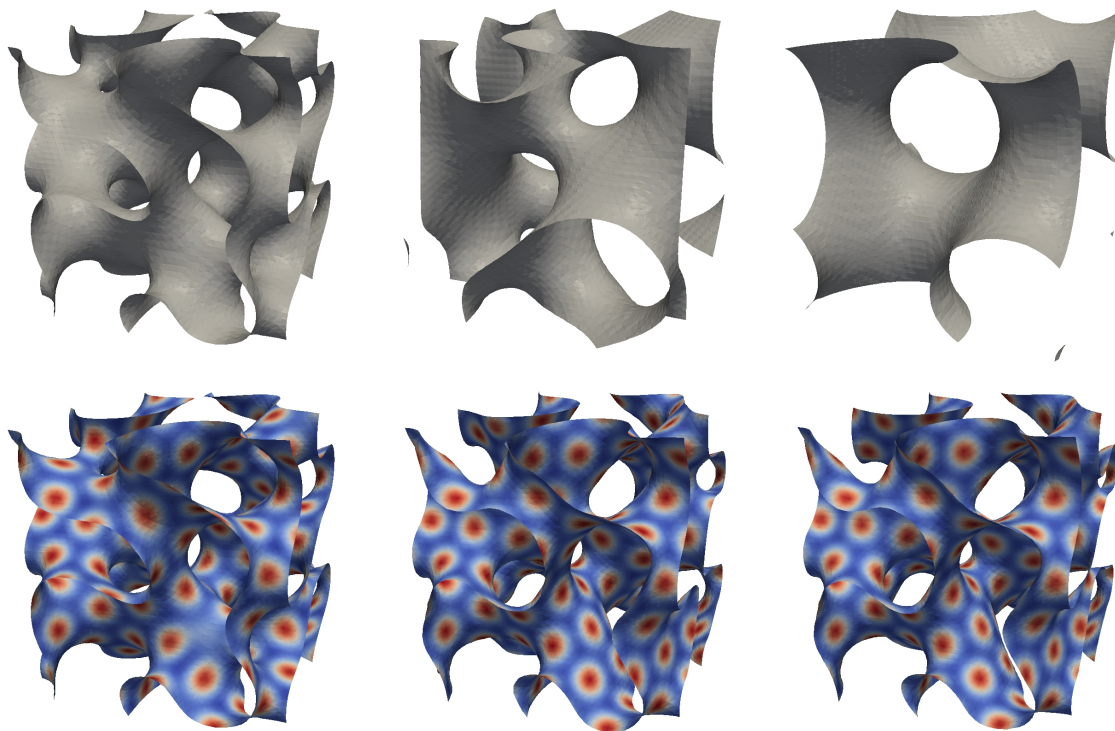
Figure 5.17: Coarsening of a fluid structure after spinodal decomposition without(top) and with(bottom) colloidal forces at times $t = 0$,134,267. Color online.
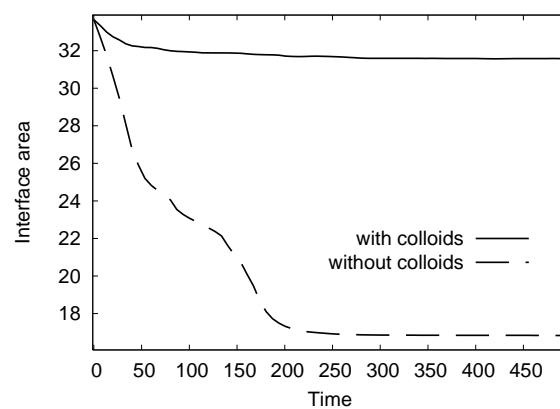

Figure 5.18: The interface area versus time for the case with and without colloids.

ball of radius 1 by a phase field ϕ using Eq. (5.1) with

$$d = 1.0 - \sqrt{(x - x_0)^2 + (y - y_0)^2}. \tag{5.159}$$

Here (x_0, y_0) denotes the coordinate of the ball's center. Using the diffuse domain approach (see Secs. 2.5, 4.2) we can now formulate the NSCHSPFC model in the domain where $\{\phi \approx 1\}$: The advective Cahn-Hilliard equation becomes

$$\phi(\partial_t \psi + \mathbf{u} \cdot \nabla \psi) = Pe_\psi^{-1} \epsilon \nabla \cdot (\phi B(\psi) \nabla \mu), \tag{5.160}$$

$$\phi \mu = \epsilon^{-1} \phi B'(\psi) - \epsilon \nabla \cdot (\phi \nabla \psi). \tag{5.161}$$

Note that this formulation imposes a contact angle of $90°$ between the fluid-fluid interface and the solid ball. The diffuse domain surface-phase-field-crystal equation[*] is

$$\partial_t(e\phi(\rho + \tilde{\rho})) + \nabla \cdot (e\phi \mathbf{u}(\rho + \tilde{\rho})) = Pe_\rho^{-1} \nabla \cdot (e\phi \nabla \tilde{\omega}), \tag{5.162}$$

$$e\phi\tilde{\omega} = e\phi\rho\left(\rho^2 + 1 + r\right) + 2\delta^2 e\phi\tilde{\nu} + \delta^4 \nabla \cdot (e\phi \nabla \tilde{\nu}), \tag{5.163}$$

$$e\phi\tilde{\nu} = \nabla \cdot (e\phi \nabla \rho). \tag{5.164}$$

Finally, the Navier-Stokes equation becomes

$$\phi\left(\partial_t \mathbf{u} + (\mathbf{u} \cdot \nabla)\mathbf{u}\right) = -\phi \nabla p + \frac{1}{Re} \nabla \cdot (\phi \nabla \mathbf{u}) + \nabla \cdot (\phi \mathbf{T}_{sing}), \tag{5.165}$$

$$\nabla \cdot (\phi \mathbf{u}) = \mathbf{v} \cdot \nabla \phi, \tag{5.166}$$

where $\mathbf{v}$ is the velocity of the moving ball. To obtain the ball velocity we solve Newton's equation, which in nondimensional form, reads

$$\dot{\mathbf{v}} = \left(\frac{\rho_{fluid}}{\rho_{ball}} - 1\right)\mathbf{g} + \frac{\rho_{fluid}}{V \rho_{ball}} \int_{\partial \Omega_{ball}} \mathbf{T} \cdot \mathbf{n} \, dA, \tag{5.167}$$

where ρ_{ball} is the physical density of the ball, V the nondimensional ball volume, $\mathbf{g}$ the nondimensional gravity force and

$$\mathbf{T} := -p\mathbf{I} + \frac{1}{Re}\left(\nabla \mathbf{u} + \nabla \mathbf{u}^T\right) + \mathbf{T}_{sing} \tag{5.168}$$

the nondimensional total stress tensor, with $\mathbf{T}_{sing}$ from Eq. (5.112). We can approximate Eq. (5.167) by

$$\dot{\mathbf{v}} = \left(\frac{\rho_{fluid}}{\rho_{ball}} - 1\right)\mathbf{g} + \frac{\rho_{fluid}}{V \rho_{ball}} \int_\Omega \mathbf{T} \cdot \nabla \phi \, dx. \tag{5.169}$$

---

[*]This equation is derived variationally by restricting the total energy to the diffuse domain marked by $\phi \approx 1$, and then restricting the energy to the surface using e.

Finally, we can calculate the new ball coordinates at any time step m by $(x_0, y_0)^m = (x_0, y_0)^{m-1} + \tau \mathbf{v}$, and then compute the new ball phase field ϕ according to Eq. (5.159).

The simulation is performed in $\Omega = [-2, 2] \times [0, 12]$. We define ψ so that there is a single horizontal fluid-fluid interface at $y = 6\frac{2}{3}$ (see Fig. 5.19). The initial condition for ρ is created as in the previous sections. We set the ball's center initially at $(x_0(0), y_0(0)) = (0, 8\frac{2}{3})$, the initial ball velocity is set to zero. Furthermore, we use $\rho_{ball} = 2\rho_{fluid}$, $\tau = 0.033$, $\epsilon = 0.04$, $Pe_\psi = 1.88$ and $\mathbf{g} = (0, -0.48)$. Simulations are carried out once without colloids ($El^{-1} = 0$), once with little elastic colloid interaction ($El = 0.01$) and once with stronger colloid interaction ($El = 0.002$). The remaining parameters and boundary conditions are as in Sec. 5.8.1.

In the case when no colloids are present the ball pushes the interface downwards, then penetrates it and falls right through it. A little droplet of the upper (blue) fluid adheres to the ball, where we observe the prescribed contact angle of $90°$. The presence of colloids makes the interface stiffer. In the case of a small strength of elasticity ($El = 0.01$) the interface deforms significantly less before the ball touches it. As the ball penetrates into the crystallized interface some colloids are pushed out and the ball loses speed. Finally, the ball stops falling and is trapped at the interface, despite gravity, held by the colloid-induced elastic forces. When the elastic interactions are stronger ($El = 0.002$) the ball does not even penetrate the interface. Here, the interface behaves like a solid and the ball reaches a steady position right above the interface. Fig. 5.22[a] shows the position of the ball over time for the three test cases, and Fig. 5.22[b] shows the minimum distance between the ball and interface when $El = 0.002$.
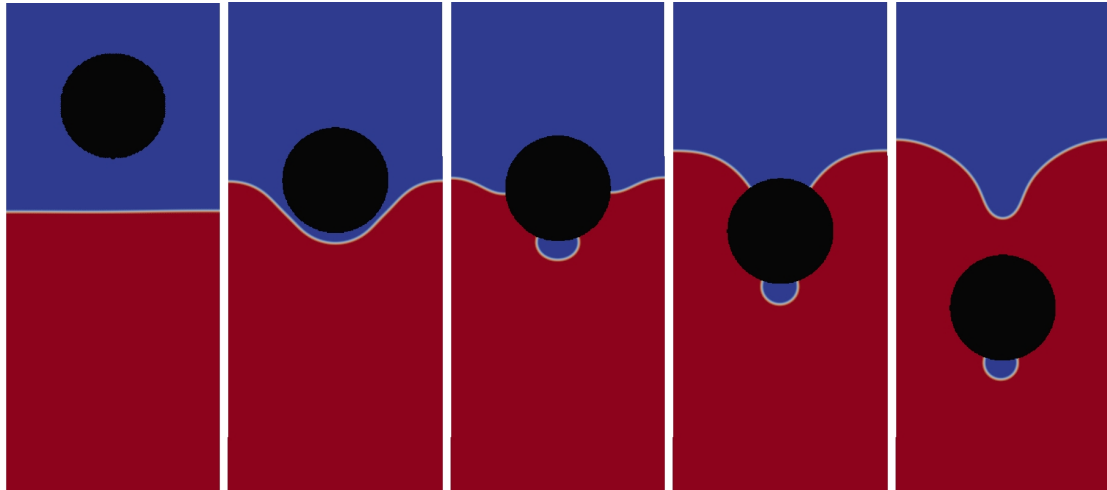
Figure 5.19: The fall of a solid ball through a fluid-fluid interface without colloids at times $t = 0,224,254,401,685$. Color online.

Figure 5.20: The fall of a solid ball through a fluid-fluid interface with colloids and low elasticity ($El = 0.01$). Images correspond to the same times as Fig. 5.19. Color online.

Figure 5.21: The fall of a solid ball through a fluid-fluid interface with colloids and high elasticity ($El = 0.002$). Images correspond to the same times as Fig. 5.19. Color online.
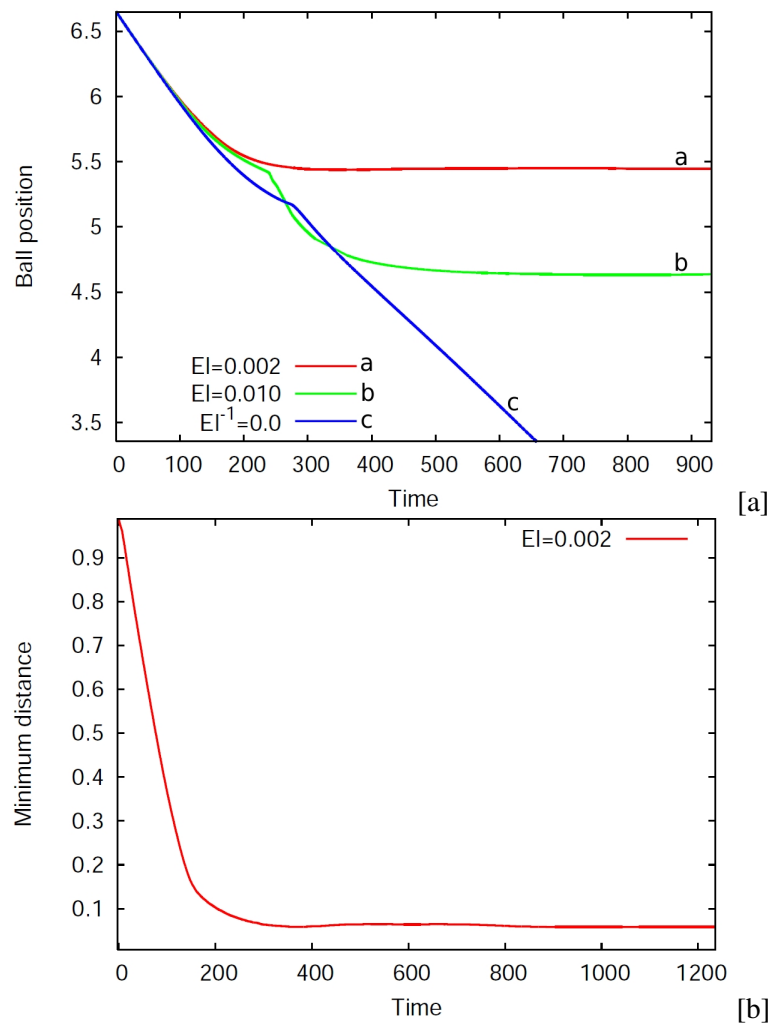
Figure 5.22: [a] The vertical position of the center of the ball over time for different strengths of elastic forces. [b] The minimum distance between the ball and interface when $El = 0.002$.
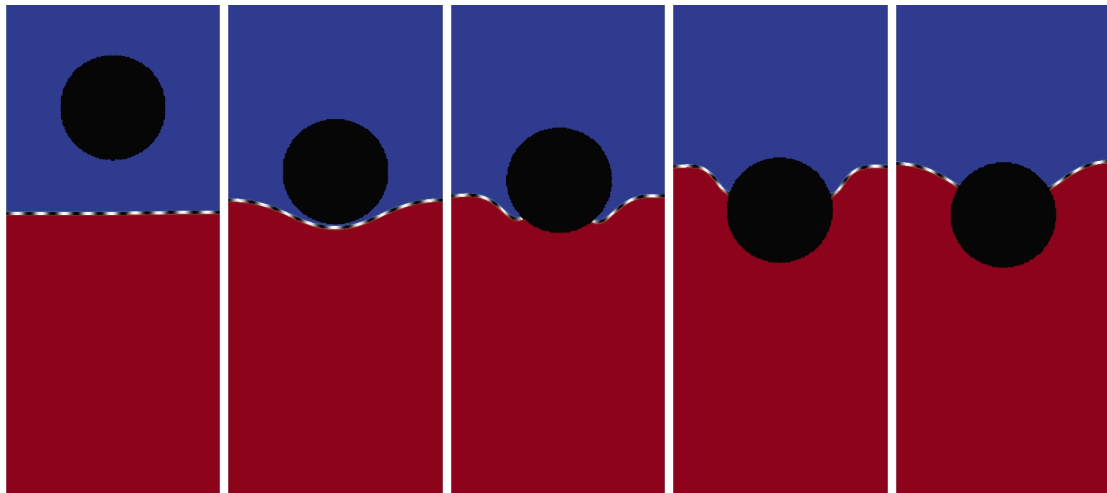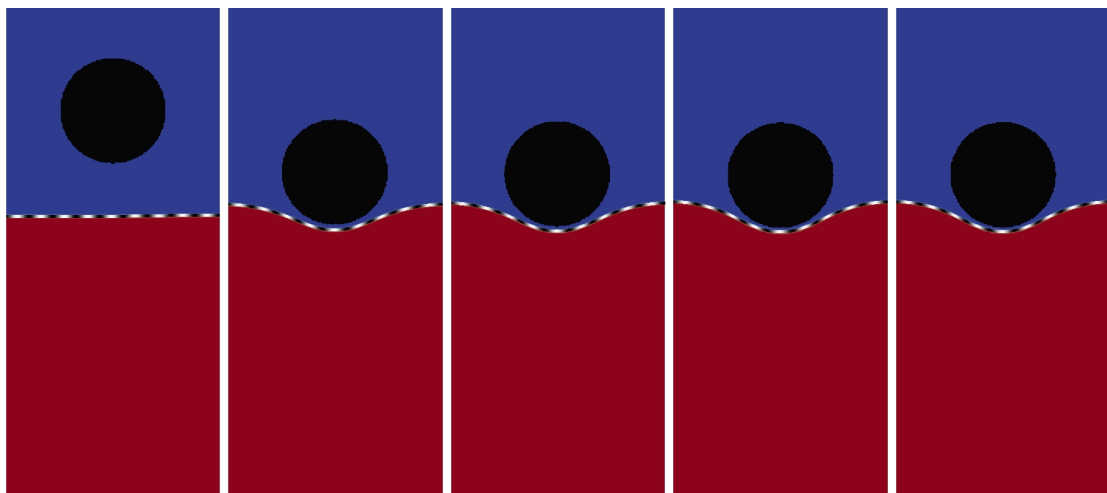
Chapter 6

Conclusions and outlook

In this thesis we have developed a model to simulate the effect of colloids at interfaces in a two-phase system. Our approach combines a Navier-Stokes-Cahn-Hilliard model for the macroscopic two-phase system with a surface Phase-Field-Crystal model for the microscopic colloidal system along the interface. The PFC model allows to use both, attractive and repulsive interactions, see [BGP$^+$11] for an appropriate parametrization of the PFC model. In the resulting NSCHSPFC model, the presence of colloids introduces elastic forces at the interface between the two immiscible fluid phases which account for the particle interactions.

To assess the accuracy of the used flow model we first conducted a benchmark study for diffuse interface models for two-phase flow. We compared different state-of-the-art diffuse interface models with other well-known interface tracking methods and found good agreement. Further, for solving the equations in arbitrary complex geometries we developed a diffuse domain approach for the Navier-Stokes Cahn-Hilliard equations. The diffuse domain formulation circumvents mesh generation of complex geometries by embedding the complex domain in a larger, regular domain and reformulating the equations using a phase-field function that approximates the characteristic function of the complex domain. This allows an easy coupling of the flow equations to a moving solid body.

A first approach in developing a full thermodynamically consistent two-phase flow model with colloids turned out to lead to local straining flows around the interface which, to be resolved, required very small time steps and grid sizes. To eliminate the straining flows, we regularized the elastic forces induced by the colloid interactions in three different ways. First, this was done in 2D by averaging across the interface. Second, we derived an improved elastic force using an energy variation approach with a different approximation of the surface delta function. The latter derivation is valid in 2D and 3D. If restricted to 2D, this leads to the same model as the averaging approach. Third, a sharp interface derivation using an energy variation approach is presented in 2D. We show that the new formulation is the diffuse interface analogue of the sharp interface model.

An adaptive finite element method is used to solve the model numerically. Using a variety of flow configurations in two dimensions, we demonstrated that as colloids jam on the interface and the interface crystallizes, the elastic force may be strong enough to make the interface sufficiently rigid to resist external forces, such as an applied shear flow, as well as surface tension induced coarsening. We

presented examples where the interface is crystallized initially and where crystallization and jamming are induced by attachment of colloids from the bulk. We also presented an example of coarsening-induced colloid jamming resulting in a bicontinuous, interfacially jammed gel (bijel). In this example, the coarsening of a two-dimensional bicontinuous structure under surface tension forces raises the colloid density sufficiently to induce jamming, which abruptly halts the coarsening process.

Finally, we demonstrated an important advantage of our multi-scale model: The possibility of incorporating additional macroscopic effects using the diffuse domain approach[LLRV09]. We modeled a solid ball, driven by gravity, falling through a colloid crystallized surface. Compared to the case without colloids, the stiffness imparted to the interface by the colloids resisted the ball motion. At small to medium colloid elasticity the ball penetrated but did not fall through the interface, as it would if the interface were clean. Interestingly, for higher elasticity the ball may not even penetrate the interface but reaches a steady position right above the interface. This clearly demonstrates the solid like properties of the particle-stabilized bicontinuous gel.

There are many interesting directions to pursue in the future, the first of which should be to process large scale simulations resolving very small values of δ needed to simulate experimental conditions. Currently methods are being developed to upscale the microscopic SPFC model and elastic force to obtain a fully macroscopic system, investigating the rheological properties of simulated bijels and comparing the results with physical systems (e.g., Refs.[CSF03, RMV07]). Another interesting application of the model is the simulation of a crossflow microreactor in which two fluids flow in opposite direction allowing close contact between mutually insoluble reagents across a colloid-stabilized interface in a bijel[SAP+05].

Bibliography

[AGG10]   H. Abels, H. Garcke, and G. Grün. Thermodynamically Consistent Diffuse Interface Models for Incompressible Two-Phase Flows with Different Densities. *preprint U Regensburg*, 2010.

[ALM+12]   S. Aland, C. Landsberg, R. Müller, F. Stenger, M. Bobeth, A. C. Langheinrich, and A. Voigt. Adaptive diffuse domain approach for calculating mechanically induced deformation of trabecular bone. *Comput. Methods Biomech. Biomed. Engin.*, 2012.

[ALV10]   S. Aland, J.S. Lowengrub, and A. Voigt. Two-phase flow in complex geometries: A diffuse domain approach. *CMES-Comput. Model. Eng. Sci.*, pages 77–107, 2010.

[ALV11]   S. Aland, J. Lowengrub, and A. Voigt. A continuum model of colloid-stabilized interfaces. *Physics of Fluids*, 23(6):062103, 2011.

[ALV12]   S. Aland, J. Lowengrub, and A. Voigt. Particles at fluid-fluid interfaces - Model improvement of a Navier Stokes Cahn Hilliard Surface Phase Field Crystal system. *Nonlinearity*, submitted 2012.

[AM04]   A.J. Archer and Rauscher M. Dynamic density functional theory for interacting Brownian particles: Stochastic or deterministic? *J. Phys. A. Math. Gen.*, 37:9325–9333, 2004.

[AMW98]   D.M. Anderson, G.B. McFadden, and A.A. Wheeler. Diffuse interface methods in fluid mechanics. *Ann. Rev. Fluid Mech.*, 30:139–165, 1998.

[Arc09]   A.J. Archer. Dynamical Density functional theory for molecular and colloidal fluids: A microscopic approach to fluid mechanics. *J. Chem. Phys.*, 130:014509, 2009.

[ARRV12]   S. Aland, A. Rätz, M. Röger, and A. Voigt. Buckling instability of viral capsids - a continuum approach. *SIAM MMS*, 2012.

[ART02]   N. Al-Rawahi and G. Tryggvason. Numerical simulation of dendritic solidification with convection: Two-dimensional flow. *J. Comput. Phys.*, 180:471–496, 2002.

[ART04]   N. Al-Rawahi and G. Tryggvason. Numerical simulation of dendritic solidification with convection: Three-dimensional flow. *J. Comput. Phys.*, 194:677–696, 2004.

[AV11]   S. Aland and A. Voigt. Benchmark computations of diffuse interface models for two-dimensional bubble dynamics. *International Journal for Numerical Methods in Fluids*, 2011.

[AV12]   S. Aland and A. Voigt. Simulation of common features and differences of surfactant-based and solid-stabilized emulsions. *Colloids and Surfaces A*, 2012.

[BAA07]   R. Backofen, Ratz A., and Voigt A. Nucleation and growth by a phase field crystal (PFC) model. *Phil. Mag. Lett.*, pages 813–820, 2007.

[Bal04]   E. Balaras. Modeling complex boundaries using an external force on fixed Cartesian grids in large-eddy simulations. *Comput. Fluids*, 33:375–404, 2004.

[Ber98]   A.L. Bertozzi. The mathematics of moving contact lines in thin liquid films. *AMS Notices*, 45:689–697, 1998.

[BGP$^+$11]   R. Backofen, M. Gräf, D. Potts, S. Praetorius, A. Voigt, and T. Witkowski. A continuous approach to discrete ordering on S2. *Multiscale Modeling and Simulation*, 9:314–334, 2011.

[BGS08]   I. Borazjani, L. Ge, and F. Sotiropoulos. Curvilinear immersed boundary method for simulating fluid structure interaction with complex 3D rigid bodies. *J. Comput. Phys.*, 227:7587–7620, 2008.

[BOPG06]   A. Bueno-Orovio and V.M. Perez-Garcia. Spectral smoothed boundary methods: The role of external boundary conditions. *Numer. Meth. Partial Diff. Eqns.*, 22:435–448, 2006.

[BOPGF06] A. Bueno-Orovio, V.M. Perez-Garcia, and F.H. Fenton. Spectral methods for partial differential equations in irregular domains: The spectral smoothed boundary method. *SIAM J. Sci. Comput.*, 28:886–900, 2006.

[Boy02]   F. Boyer. A theoretical and numerical model for the study of incompressible mixture flows. *Computers and Fluids*, pages 41–68, 2002.

[BWV10]   R. Backofen, T. Witkowski, and A. Voigt. Particles on curved surfaces - a dynamic approach by a phase field crystal model. *Phys. Rev. E*, 81:025701 R, 2010.

[BYZ03]   G. Biros, L. Ying, and D. Zorin. A fast solver for the Stokes equations with distributed forces in complex geometries. *J. Comput. Phys.*, 193:317–348, 2003.

[CC08]   M. E. Cates and P. S. Clegg. Bijels: a new class of soft materials. *Soft Matter*, 4:2132–2138, 2008.

[CH58]   J.W. Cahn and J.E. Hilliard. Free energy of a nonuniform system: 1. Interfacial free energy. *J. Chem. Phys.*, 28:258–267, 1958.

[Cho68]   A. J. Chorin. Numerical solution of the Navier-Stokes equations. *Math. Comp.*, 22, 1968.

[CHS⁺08]   P. S. Clegg, E.M. Herzig, A.B. Schofield, S.U. Egelhaaf, T.S. Horozov, B.P. Binks, M.E. Cates, and W.C.K. Poon. Emulsification of partially miscible fluids using colloidal particles: Nonspherical and extended domain structures. *Langmuir*, 23:5984–5994, 2008.

[Chu06]   M.-H. Chung. Cartesian cut cell approach for simulating incompressible flows with rigid bodies of arbitrary shape. *Computers & Fluids*, 35:607–623, 2006.

[Cle08]   P. S. Clegg. Fluid-bicontinuous gels stabilized by interfacial colloids: Low and high molecular weights. *J. Phys. Condens. Matter*, 20:113101, 2008.

[CO02]   P.S. Christopher and D.W. Oxtoby. Density functional model of surfactant mesostructures. *J. Chem. Phys.*, 117:9502–9509, 2002.

[COER07]   J.-I. Choi, R.C. Oberoi, J.R. Edwards, and J.A. Rosati. An immersed boundary method for complex incompressible flows. *J. Comput. Phys.*, 224:757–784, 2007.

[COFC05]   H.J. Chung, K. Ohno, T. Fukuda, and R.J. Composto. Self-regulated structures in nanocomposites by directed nanoparticle assembly. *Nano Lett.*, 5:1878–1882, 2005.

[Cow05]   C. Cowan. The Cahn-Hilliard equation as a gradient flow. *Burnaby B.C. : Simon Fraser University*, 2005.

[CSF03]   P. Cicuta, E.J. Stancik, and G.G. Fuller. Shearing or compressing a soft glass in 2D: Time-concentration superposition. *Phys. Rev. Lett.*, 90:236101, 2003.

[Dav95]   T. Davis. Users' guide for the Unsymmetric-pattern MultiFrontal Package (UMFPACK). , 1995. Tech. rep. TR-95-004. Computer and Information Sciences Department, University of Florida, Gainesville, FL.

[Dav02]   S.H. Davis. Interfacial fluid dynamics. In G.K. Batchelor, H.K. Moffatt, and M.G. Worster, editors, *Perspectives in Fluid Dynamics*. Cambridge University Press, 2002.

[Dav04]   Timothy A. Davis. Algorithm 832: UMFPACK V4.3—an unsymmetric-pattern multifrontal method. *ACM Trans. Math. Softw.*, 30(2):196–199, June 2004.

[DBO00]   C.A. Duarte, I. Babuska, and J.T. Oden. Generalized finite element methods for three-dimensional structural mechanics problems. *Comp. Struct.*, 77:215–232, 2000.

[DDE05]   K. Deckelnick, G. Dziuk, and C. M. Elliott. Computation of geometric partial differential equations and mean curvature flow. *Acta Numerica*, 14:139–232, 2005.

[de 85]   P.G. de Gennes. Wetting: statics and dynamics. *Rev. Mod. Phys.*, 57:827–863, 1985.

[Dic10]   E. Dickinson. Solid-stabilized emulsions. *Curr. Opinion Coll. Int. Sci.*, 15:40–49, 2010.

[DQA09]   Minh Do-Quang and Gustav Amberg. The splash of a solid sphere impacting on a liquid surface: Numerical simulation of the influence of wetting. *Physics of Fluids*, 21, 2009.

[DSR06]   J. Deng, X.-M. Shao, and A.-L. Ren. A new modification of the immersed-boundary method for simulating flows with complex moving boundaries. *Int. J. Num. Meth. Fluids*, 52:1195–1213, 2006.

[DSS07]   H. Ding, P.D.M. Spelt, and C. Shu. Diffuse interface model for incompressible two-phase flows with large density ratios. *J. Comput. Phys.*, pages 2078–2095, 2007.

[dZGW$^+$09] D. de Zelicourt, L. Ge, C. Wang, F. Sotiropoulos, A. Gilmanov, and A. Yoganathan. Flow simulations in arbitrarily complex cardiovascular anatomies– An unstructured Cartesian grid approach. *Computers & Fluids*, 38:1749–1762, 2009.

[EG04]   K.R. Elder and M. Grant. Modeling elastic and plastic deformations in nonequilibrium processing using phase field crystals. *Phys. Rev. E*, 70:051605, 2004.

[EGK08]   C. Eck, H. Garcke, and P. Knabner. *Mathematische Modellierung*. Springer, 2008.

[EKHG02]   K.R. Elder, M. Katakowski, M. Haataja, and M. Grant. Modeling elasticity in crystal growth. *Phys. Rev. Lett.*, 88, 2002.

[Emm08]   H. Emmerich. Advances of and by phase-field modeling in condensed-matter physics. *Adv. Phys.*, 57:1–87, 2008.

[EPB$^+$07] K.R. Elder., N. Provatas, J. Berry, P. Stefanovic, and M. Grant. Phase-field crystal modeling and classical density functional theory of freezing. *Phys. Rev. B*, 75(6):064107, Feb 2007.

[FCKR05]   F.H. Fenton, E.M. Cherry, A. Karma, and W.-J. Rappel. Modeling wave propagation in realistic heart geometries using the phase-field method. *Chaos*, 15:013502, 2005.

[Fen06]   X. Feng. Fully Discrete Finite Element Approximations of the Navier–Stokes–Cahn-Hilliard Diffuse Interface Model for Two-Phase Fluid Flows. *SIAM J. Numer. Anal.*, 44:1049–1072, 2006.

[FMD09]   H. Firoozmand, B.S. Murray, and E. Dickinson. Interfacial structuring in a phase-separating mixed biopolymer solution containing colloidal particles. *Langmuir*, 25:1300–1305, 2009.

[FW05]   Xiaobing Feng and Hai-jun Wu. A Posteriori Error Estimates and an Adaptive Finite Element Method for the Allen-Cahn Equation and the Mean Curvature Flow. *Journal of Scientific Computing*, 24:121–146, 2005. 10.1007/s10915-004-4610-1.

[GA08]   A. Gilmanov and S. Acharya. A hybrid immersed boundary and material point method for simulating 3D fluid-structure interaction problems. *Int. J. Num. Meth. Fluids*, 56:2151–2177, 2008.

[GICM07]   F. Gao, D.M. Ingram, D.M. Causon, and C.G. Mingham. The development of a Cartesian cut cell method for incompressible viscous flows. *Int. J. Num. Meth. Fluids*, 54:1033–1053, 2007.

[GLL08]   Y. Gong, B. Li, and Z. Li. Immersed-interface finite-element method for elliptic interface problems with non-homogeneous jump conditions. *SIAM J. Numer. Anal.*, 26:472–495, 2008.

[GPH$^+$01]   R. Glowinsky, T.W. Pan, T.I. Hesla, D.D. Joseph, and J. Periaux. A fictitious domain approach to the direct numerical simluation of incompessible viscous flow past moving rigid bodies: Application to particulate flow. *J. Comput. Phys*, 169:363–426, 2001.

[GPP06]   R. Glowinksi, T.W. Pan, and J. Periaux. Numerical simulation of a multi-store separation phenomenon: A fictitious domain approach. *Comp. Meth. Appl. Mech. Eng.*, 195:5566–5581, 2006.

[GPSW07]   László Gránásy, Tamás Pusztai, David Saylor, and James A. Warren. Phase Field Theory of Heterogeneous Crystal Nucleation. *Physical Review Letters*, 98(3):035703, 2007.

[GPV96]   M.E. Gurtin, D. Poligone, and J. Vinale. Two-phase fluids and immiscible fluids described by an order parameter. *Math. Models. Methods Appl. Sci.*, 6:815–831, 1996.

[GQ00]   Guermond and Quartapelle. A Projection FEM for Variable Density Incompressible Flows. *J. Comput. Phys.*, 2000.

[GS05]   A. Gilmanov and F. Sotiropoulos. A hybrid Cartesian/immersed boundary method for simulating flows with 3D, geometrically complex, moving bodies. *J. Comput. Phys.*, 207:457–492, 2005.

[Har99]   Erich Hartmann. On the curvature of curves and surfaces defined by normalforms. *Computer Aided Geometric Design*, 16(5):355–376, jun 1999.

[HH77]   P.C. Hohenberg and B.I. Halperin. Theory of dynamic critical phenomena. *Rev. Mod. Phys.*, 49:435–479, 1977.

[HL07]   M.J.A. Hore and M. Laradji. Microphase separation induced by interfacial segregation of isotropic spherical nanoparticles. *J. Chem. Phys.*, 126:244903, 2007.

[HPZ01]   H.H. Hu, N.A. Patankar, and M.Y. Zhu. Direct numerical simulations of fluid-solid systems using the arbitrary Lagrangian-Eulerian technique. *J. Comput. Phys.*, 169:427–462, 2001.

[HTK$^+$09] S. Hysing, S. Turek, D. Kuzmin, N. Parlini, E. Burman, S. Ganesan, and L. Tobiska. Quantitative benchmark computations of two-dimensional bubble dynamics. *Int. J. Numer. Meth. Fluids*, 60:1259–1288, 2009.

[HWS$^+$07] E. M. Herzig, K. A. White, A. B. Schofield, W. C. Poon, and P. S. Clegg. Bicontinuous emulsions stabilized solely by colloidal particles. *Nature materials*, 6(12):966–971, December 2007.

[Jaq99]   D. Jaqmin. Calculation of two-phase Navier-Stokes flows using phase-field modelling. *J. Comput. Phys.*, 155:96–127, 1999.

[JH11]   F. Jansen and J. Harting. From Bijels to Pickering emulsions: a lattice Boltzmann study. *Physical Review E*, 83:046707, 2011.

[JS09]   A.S. Joshi and Y. Sun. Multiphase lattice Boltzmann method for particle suspensions . *Physical Review E*, 79:066703, 2009.

[JTB02]   D. Jamet, D. Torres, and J.U. Brackbill. On the theory and computation of surface tension: The elimination of parasitic currents through energy conservation in the second-gradient method. *J. Comput. Phys.*, pages 262–276, 2002.

[KAK03]   M.P. Kirkpatrick, S.W. Armfield, and J.H. Kent. A representation of curved boundaries for the solution of the Navier-Stokes equations on a staggered three-dimensional Cartesian grid. *J. Comput. Phys.*, 184:1–36, 2003.

[KC94]   S. Kalliadasis and H.-C. Chang. Apparent dynamic contact angle of an advancing gas-liquid meniscus. *Phys. Fluids*, 6:12–23, 1994.

[KLR03]   J. Kockelkoren, H. Levine, and W.-J. Rappel. Computational approach for modeling intra- and extracellular dynamics. *Phys. Rev. E*, 68:037702, 2003.

[Kro99]   M.C. Kropinski. Integral equation methods for particle simulations in creeping flows. *Comp. Math. Appl.*, 38:67–87, 1999.

[KSAC08]   E. Kim, K. Stratford, R. Adhikari, and M.E. Cates. Arrest of fluid demixing by nanoparticles: A computer simulation study. *Langmuir*, 24:6549–6556, 2008.

[KUGS08]   J. Koza, M. Uhlemann, A. Gebert, and L. Schultz. The effect of magnetic fields on electrodeposition of CoFe alloys. *Electrochim. Acta*, 53:5344–5353, 2008.

[KW07]   D. Kay and R. Welford. Efficient Numerical Solution of Cahn-Hilliard-Navier-Stokes Fluids in 2D. *SIAM J. Sci. Comput.*, 29:2241–2257, 2007.

[Lad94a]   A. J. C. Ladd. Numerical Simulations of Particulate Suspensions via a discretized Boltzmann Equation. Part I. Theoretical Foundation . *J. Fluid Mech.*, pages 271–285, 1994.

[Lad94b]   A. J. C. Ladd. Numerical Simulations of Particulate Suspensions via a discretized Boltzmann Equation. Part II. Numerical results . *J. Fluid Mech.*, pages 271–311, 1994.

[LCS08]   F. Leal-Calderon and V. Scmitt. Solid-stabilized emulsions. *Curr. Opinion Coll. Int. Sci.*, 13:217–227, 2008.

[Lin07]   P. Lin. A fixed-grid model for simulation of a moving body in free surface flows. *Computers & Fluids*, 36:549–561, 2007.

[LLRV09]   X. Li, J. Lowengrub, A. Rätz, and A. Voigt. Solving pdes in complex geometries: A diffuse domain approach. *Commun. Math. Sci.*, 7:81–107, 2009.

[LLW03]   Z.L. Li, T. Lin, and X.H. Wu. New Cartesian grid methods for interface problems using the finite element formulation. *Num. Math.*, 96:61–98, 2003.

[LR05]   H. Levine and W.-J. Rappel. Membrane-bound Turing patterns. *Phys. rev. E*, 72:061912, 2005.

[LRV09]   J. Lowengrub, A. Rätz, and A. Voigt. Phase-field modeling of the dynamics of multicomponent vesicles: Spinodal decomposition, coarsening, budding and fission . *Physical Review E*, 79:031926, 2009.

[LT98]   J. Lowengrub and L. Truskinovsky. Quasi-incompressible Cahn-Hilliard fluids and topological changes. *Proc. Roy. Soc. London A*, 454:2617–2654, 1998.

[LV01]   A. J. C. Ladd and R. Verberg. Lattice-Boltzmann simulations of particle-fluid suspensions. *J. Stat. Phys.*, 104:1191–1251, 2001.

[May84]   A. Mayo. The fast solution of Poisson's and the biharmonic equations on irregular regions. *SIAM J. Numer. Anal.*, 21:285–299, 1984.

[MB96]   J.M. Melenk and I. Babuska. The partition of unity finite element method: Basic theory and applications. *Comp. Meth. Appl. Mech. Eng.*, 139:289–314, 1996.

[MDB+07]   R. Mittal, H. Dong, M. Bozkurttas, F.M. Najjar, A. Vargas, and A. von Loebbecke. A versatile sharp interface immersed boundary method for incompressible flows with complex boundaries. *J. Comput. Phys.*, 227:4825–4852, 2007.

[MK06]   M. Muradoglu and A.D. Kayaalp. An auxilliary grid method for computations of multiphase flows in complex geometries. *J. Comput. Phys.*, 214:858–877, 2006.

[MS05]   M. Muradoglu and H. A. Stone. Mixing in a drop moving through a serpentine channel: A computational study. *Physics of Fluids*, 17(7), July 2005.

[MT99]   U.M.B. Marconi and P. Tarazona. Dynamical Density functional theory of liquids. *J. Chem. Phys.*, 110:8032–8044, 1999.

[MW11]   Paul C. Millett and Yu U. Wang. Diffuse-interface field approach to modeling arbitrarily-shaped particles at fluid–fluid interfaces. *Journal of Colloid and Interface Science*, 353:46–51, 2011.

[MYG+05]   W.L. Ma, C.Y. Yang, X. Gong, K. Lee, and A.J. Heeger. Thermally stable, efficient polymer solar cells with nanoscale control of the interpenetrating network morphology. *Adv. Functional Mater.*, 15:1617–1622, 2005.

[NLS00]   I. Napari, A. Laaksonen, and R. Strey. Density-functional studies of amphiphilic binary mixtures. *J. Chem. Phys.*, 113:4476–4487, 2000.

[ODB97]   A. Oron, S.H. Davis, and S.G. Bankoff. Long-scale evolution of thin liquid films. *Rev. Mod. Phys.*, 69:931–980, 1997.

[ODZ98]   J.T. Oden, C.A. Duarte, and O.C. Zienkiewicz. A new cloud-based hp finite element method. *Comp. Meth. Appl. Mech. Eng.*, 153:117–126, 1998.

[PDA+07] N. Provatas, J.A. Dantzig, B. Athreya, P. Chan, P. Stefanovic, N. Goldenfeld, and K. Elder. Using the phase-field crystal method in the multiscale modeling of microstructure evolution. *JOM*, 59:83–90, 2007.

[PE10] N. Provatas and K. Elder. *Phase-field methods in Materials Science and Engineering*. Wiley-VCH, 2010.

[Peg89] R. L. Pego. Front Migration in the Nonlinear Cahn-Hilliard Equation. *Proceedings of the Royal Society of London*, 422(1863):261–278, 1989.

[Pic07] S. Pickering. Emulsions. *J. Chem Soc.*, 91:2001–2021, 1907.

[PPGJ09] J. Pao, T.W. Pan, R. Glowinski, and D.D. Joseph. A fictitious domain/distributed Lagrange multiplier method for the particulate flow for Oldroyd-B fluids: A positive definiteness preserving approach. *J. Non-Newtonian Fluid Mech.*, 156:95–111, 2009.

[RMV07] S. Reynaert, P. Moldenaers, and J. Vermant. Interfacial rheology of stable and weakly aggregated two-dimensional suspensions. *Phys. Chem. Chem. Phys.*, 9:6463–6475, 2007.

[RV06] A. Rätz and A. Voigt. PDE's on surfaces - a diffuse interface approach. *Comm. Math. Sci.*, 4:575–590, 2006.

[RV07] Andreas Rätz and A Voigt. A diffuse-interface approximation for surface diffusion including adatoms. *Nonlinearity*, 20(1):177–192, jan 2007.

[SAMS05] A.B. Subramaniam, M. Abkarian, L. Mahadevan, and H.A. Stone. Non-spherical bubbles. *Nature*, 438:930–930, 2005.

[SAP+05] K Stratford, R Adhikari, I Pagonabarraga, J C Desplat, and M E Cates. Colloidal Jamming at Interfaces: a Route to Fluid-bicontinuous Gels. *Science*, 309:2198–2201, Oct 2005.

[SGV09] A.F. Shinn, M.A. Goodwin, and S.P. Vanka. Immersed boundary computations of shear- and buoyancy-driven flows in complex enclosures. *Int. J. Heat Mass Transfer*, 52:4082–4089, 2009.

[SH77] J. Swift and P.C. Hohenberg. Hydrodynamic fluctuations at convective instability. *Phys. Rev. A*, 15:319–328, 1977.

[SLS08] I. Singer-Loginova and H. Singer. The phase field technique for modeling multiphase materials. *Rep. Prog. Phys.*, 71:106501, 2008.

[STL+10] J. S. Sohn, Y.-H. Tseng, Sh. Li, A. Voigt, and J.S. Lowengrub. Dynamics of multicomponent vesicles in a viscous fluid. *J. Comput. Phys.*, 229:119–144, 2010.

[SWCC09] E. Sanz, K.A. White, P.S. Clegg, and M.E. Cates. Colloidal gels assembled via a temporary interfacial scaffold. *Phys. Rev. Lett.*, 103:255502, 2009.

[SY10]   Shen and Yang. A phase-field model and its numerical approximation for two-phase incompressible flows with different densities and viscosities. *SIAM J. Sci. Comput.*, 2010.

[TBE$^+$01]   G. Tryggvason, B. Buner, A. Esmaeeli, D. Juric, N. Al-Rawahi, W. Tauber, J. Han, S. Nas, and Y.-J. Jan. A front-tracking method for the computation of multiphase flow. *J. Comput. Phys.*, 169:708–759, 2001.

[TF03]   Y.-H. Tseng and J.H. Ferziger. A ghost-cell immersed boundary method for flow in complex geometry. *J. Comput. Phys.*, 192:593–623, 2003.

[TLL$^+$09]   K.E. Teigen, X. Li, J. Lowengrub, F. Wang, and A. Voigt. A diffuse-interface approach for modeling transport, diffusion and adsorption/desorption of material quantities on a deformable interface. *Comm. Math. Sci.*, 7:1009–1037, 2009.

[TSC11]   J. H. J. Thijssen, A. B. Schofield, and P. Clegg. How do (fluorescent) surfactants affect particle-stabilized emulsions? . *Soft Matter*, pages 7965–7968, 2011.

[TSLV10]   K.E. Teigen, P. Song, J. Lowengrub, and A. Voigt. A diffuse interface method for two-phase flows with soluble surfactants. *J. Comput. Phys.*, 230:375–393, 2010.

[UKSTST97] H.S. Udaykumar, H.-C. Kan, W. Shyy, and R. Tran-Son-Tay. Multiphase dynamics in arbitrary geometries on fixed Cartesian grids. *J. Comput. Phys.*, 137:366–405, 1997.

[Ulb06]   M. Ulbricht. Advanced functional polymer membranes. *Polymer*, 47:2217–2262, 2006.

[UMRK01]   H.S. Udaykumar, R. Mittal, P. Rampunggoon, and A. Khanna. A sharp interface Cartesian grid method for simulating flows with complex moving boundaries. *J. Comput. Phys.*, 174:345–380, 2001.

[USS09]   E. Uzgoren, J. Sim, and W. Shyy. Marker-based, 3-D adaptive Cartesian grid method for multiphase flows around irregular geometries. *Commun. Comput. Phys.*, 5:1–41, 2009.

[VA06]   W. Villanueva and G. Amberg. Some generic capillary-driven flows. *Int. J. Multiphase Flow*, 32(9):1072–1086, September 2006.

[Ver96]   R. Verfürth. *A review of a posteriori error estimation and adaptive mesh-refinement techniques*. Wiley-Teubner Series Advances in Numerical Mathematics. Chichester: John Wiley & Sons. Stuttgart: B. G. Teubner. vi, 127 p., 1996.

[vTBVL09]   S. van Teeffelen, R. Backofen, A. Voigt, and H. Löwen. Derivation of the phase-field-crystal model for colloidal solidification. *Phys. Rev. E*, 79(5):051404, May 2009.

[VV07]   S. Vey and A. Voigt. AMDiS: adaptive multidimensional simulations. *Computing and Visualization in Science*, 10(1):57–67, March 2007.

[VWed]   A. Voigt and T. Witkowski. AMDiS - A user friendly adaptive finite element toolbox for HPC. *ACM Trans. Math. Soft.*, 2012, submitted.

[WK07]   K.A. Wu and A. Karma. Phase-field crystal modeling of equilibrium bcc-liquid inter-faces. *Phys. Rev. B*, 76, 2007.

[WV09]   K.-A. Wu and P.W. Voorhees. Stress-induced morphological instabilities at the nanoscale examined using the phase field crystal approach. *Phys. Rev. B*, 80:125408, 2009.

[XW06]   S. Xu and Z.J. Wang. An immersed interface method for simulating the interaction of a fluid with moving boundaries. *J. Comput. Phys.*, 216:454–493, 2006.

[YS07]   Z.S. Yu and X.M. Shao. A direct-forcing fictitious domain method for particulate forces. *J. Comput. Phys.*, 227:292–314, 2007.

[YTPFT02]   Z.S. Yu, N. Thien-Phan, Y. Fan, and R.I. Tanner. Viscoelastic mobility problem of a system of particles. *J. Non-Newtonian Fluid Mech.*, 104:87–124, 2002.

[ZBD06]   C. Zeng, H. Bissig, and A.D. Dinsmore. Particles on droplets: From fundamental physics to novel materials. *Solid State Comm.*, 139:547–556, 2006.

[ZMOW98]   H.-K. Zhao, B. Merriman, S. Osher, and L. Wang. Capturing the behavior of bubbles and drops using the variational level set approach. *J. Comput. Phys.*, 143:495–418, 1998.

[ZYF+10]   C. Zhou, P. Yue, J.J. Feng, C.F. Ollivier-Gooch, and H.H. Hu. 3D phase-field simulations of interfacial dynamics in Newtonian and viscoelastic fluids. *J. Comput. Phys.*, 229:498–511, 2010.

Appendix A

Benchmark results

ϵ	c_{min}	$t\|_{c=c_{min}}$	$V_{c,max}$	$t\|_{V_c=V_{c,max}}$	$y_c(t=3)$
0.040	0.9322	1.936	0.2359	1.016	1.0692
0.020	0.9154	2.040	0.2380	1.040	1.0739
0.010	0.9062	1.996	0.2394	0.954	1.0768
0.005	0.9041	1.924	0.2402	0.929	1.0786
ref	0.9013	1.900	0.2417	0.924	1.0799

Table A.1: Model 1: Minimum circularity and maximum rise velocity, with corresponding incidence times and final position of the center of mass for test case 1. The line 'ref' gives a reference value from group 3 in [HTK$^+$09].

ϵ	c_{min}	$t\|_{c=c_{min}}$	$V_{c,max}$	$t\|_{V_c=V_{c,max}}$	$y_c(t=3)$
0.040	0.9111	1.800	0.2530	0.960	1.1101
0.020	0.8924	1.792	0.2464	0.876	1.0862
0.010	0.8910	1.830	0.2439	0.904	1.0785
0.005	0.8946	1.843	0.2434	0.914	1.0779
ref	0.9013	1.900	0.2417	0.924	1.0799

Table A.2: Model 2: Minimum circularity and maximum rise velocity, with corresponding incidence times and final position of the center of mass for test case 1. The line 'ref' gives a reference value from group 3 in [HTK$^+$09].

ϵ	c_{min}	$t\|_{c=c_{min}}$	$V_{c,max}$	$t\|_{V_c=V_{c,max}}$	$y_c(t=3)$
0.040	0.9334	1.9440	0.2350	1.0160	1.0682
0.020	0.9159	2.0040	0.2375	1.0400	1.0733
0.010	0.9066	1.9910	0.2393	0.9530	1.0767
0.005	0.9045	1.9460	0.2401	0.9460	1.0785
ref	0.9013	1.9000	0.2417	0.9239	1.0817

Table A.3: Model 3: Minimum circularity and maximum rise velocity, with corresponding incidence times and final position of the center of mass for test case 1. The line 'ref' gives a reference value from group 3 in [HTK$^+$09].
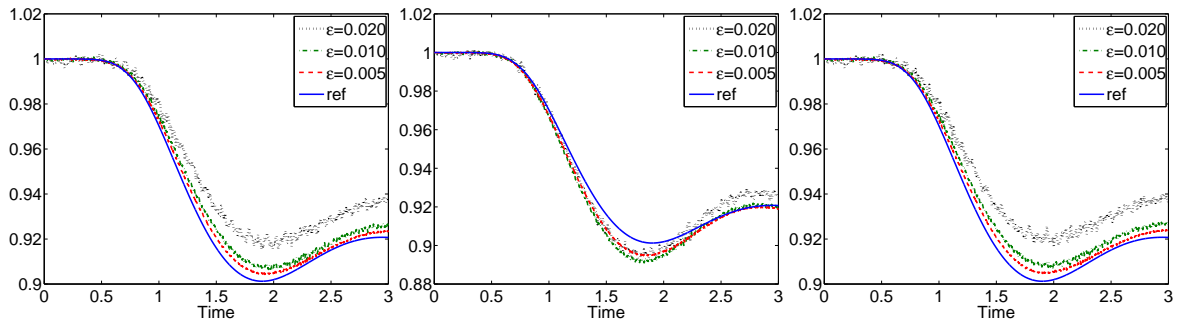
Figure A.1: Circularity versus time for test case 1 and model 1 - 3 (from left to right). Color online.
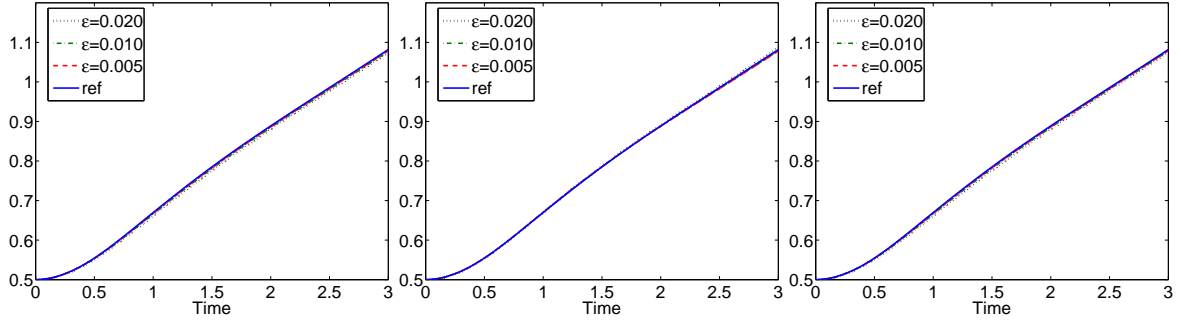
Figure A.2: Center of mass versus time for test case 1 and model 1 - 3 (from left to right). Color online.
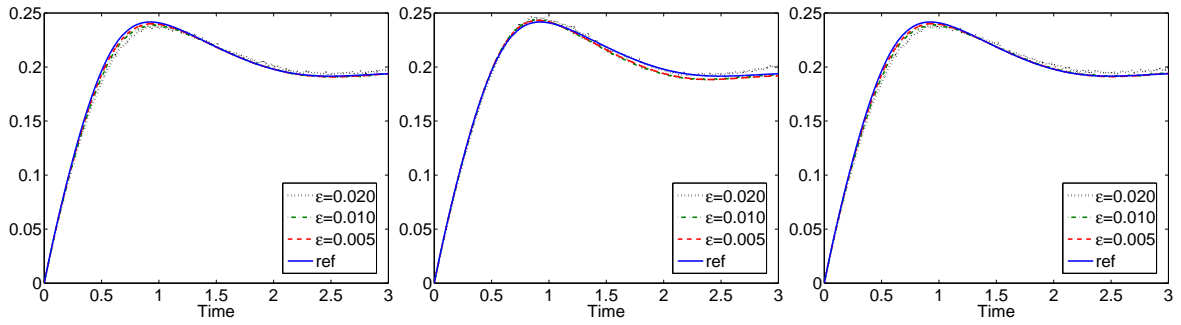
Figure A.3: Rise velocity versus time for test case 1 and model 1 - 3 (from left to right). Color online.

ϵ	$\|e\|_1$	ROC_1	$\|e\|_2$	ROC_2	$\|e\|_\infty$	ROC_∞
Center of mass						
0.040	0.0193		0.0205		0.0236	
0.020	0.0086	1.1619	0.0091	1.1738	0.0094	1.3280
0.010	0.0045	0.9483	0.0047	0.9512	0.0046	1.0249
0.005	0.0026	0.7746	0.0028	0.7601	0.0030	0.6405
Rise velocity						
0.040	0.0588		0.0632		0.0968	
0.020	0.0188	1.6421	0.0233	1.4365	0.0479	1.0148
0.010	0.0086	1.1298	0.0127	0.8800	0.0263	0.8649
0.005	0.0049	0.7979	0.0071	0.8386	0.0147	0.8397
Circularity						
0.040	0.0280		0.0329		0.0596	
0.020	0.0118	1.2469	0.0138	1.2566	0.0227	1.3932
0.010	0.0042	1.4797	0.0051	1.4403	0.0093	1.2879
0.005	0.0021	0.9860	0.0027	0.9238	0.0049	0.9290

Table A.4: Model 1: Relative error norms and convergence orders for test case 1.

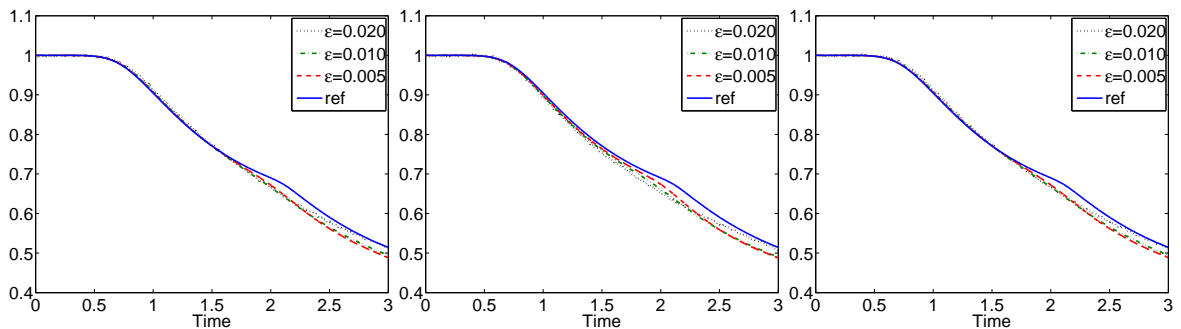**Figure A.4:** Circularity versus time for test case 2 and model 1 - 3 (from left to right). Color online.

ϵ	$||e||_1$	ROC$_1$	$||e||_2$	ROC$_2$	$||e||_\infty$	ROC$_\infty$
Center of mass						
0.040	0.0117		0.0154		0.0302	
0.020	0.0021	2.4942	0.0025	2.6478	0.0047	2.7000
0.010	0.0013	0.6538	0.0017	0.5712	0.0030	0.6115
0.005	0.0015	-0.1534	0.0020	-0.2711	0.0036	-0.2228
Rise velocity						
0.040	0.0879		0.0977		0.1625	
0.020	0.0106	3.0468	0.0130	2.9105	0.0327	2.3125
0.010	0.0117	-0.1403	0.0134	-0.0411	0.0214	0.6113
0.005	0.0104	0.1791	0.0119	0.1649	0.0170	0.3354
Circularity						
0.040	0.0181		0.0209		0.0354	
0.020	0.0041	2.1593	0.0050	2.0667	0.0115	1.6236
0.010	0.0040	0.0061	0.0058	-0.2260	0.0122	-0.0898
0.005	0.0030	0.4082	0.0042	0.4697	0.0081	0.5850

Table A.5: Model 2: Relative error norms and convergence orders for test case 1.

ϵ	$||e||_1$	ROC$_1$	$||e||_2$	ROC$_2$	$||e||_\infty$	ROC$_\infty$
Center of mass						
0.040	0.0205		0.0218		0.0238	
0.020	0.0090	1.1801	0.0096	1.1901	0.0098	1.2764
0.010	0.0045	0.9920	0.0048	0.9962	0.0047	1.0623
0.005	0.0026	0.7835	0.0028	0.7695	0.0030	0.6484
Rise velocity						
0.040	0.0570		0.0617		0.0978	
0.020	0.0188	1.6024	0.0236	1.3860	0.0486	1.0072
0.010	0.0087	1.1134	0.0129	0.8724	0.0266	0.8731
0.005	0.0050	0.8020	0.0071	0.8504	0.0148	0.8392
Circularity						
0.040	0.0286		0.0336		0.0605	
0.020	0.0123	1.2192	0.0143	1.2282	0.0238	1.3463
0.010	0.0045	1.4422	0.0054	1.4163	0.0094	1.3451
0.005	0.0022	1.0083	0.0028	0.9516	0.0050	0.9170

Table A.6: Model 3: Relative error norms and convergence orders for test case 1.

ϵ	model 1		model2		model3	
	$||e||_1$	ROC$_1$	$||e||_1$	ROC$_1$	$||e||_1$	ROC$_1$
Center of mass						
0.040	0.0167		0.0131		0.0172	
0.020	0.0060	1.4721	0.0032	2.0262	0.0057	1.5942
0.010	0.0019	1.6927	0.0005	2.8251	0.0016	1.8237
Rise velocity						
0.040	0.0559		0.0979		0.0551	
0.020	0.0157	1.8352	0.0172	2.5124	0.0174	1.6613
0.010	0.0041	1.9310	0.0030	2.5366	0.0046	1.9214
Circularity						
0.040	0.0259		0.0212		0.0255	
0.020	0.0097	1.4184	0.0030	2.8293	0.0102	1.3193
0.010	0.0021	2.1842	0.0014	1.0595	0.0025	2.0423

Table A.7: Relative error norms and convergence orders for test case 1 assuming the finest grid solution as exact solution.

ϵ	c_{min}	$t|_{c=c_{min}}$	$V_{c,max}$	$t|_{V_c=V_{c,max}}$	$y_c(t=3)$
0.040	0.6779	2.0000	0.2527	0.7360	0.8891
0.020	0.6669	2.0000	0.2520	0.7960	0.8998
0.010	0.6663	2.0000	0.2491	0.7100	0.9060
0.005	0.6718	2.0000	0.2491	0.7380	0.9099
ref	0.6901	2.0000	0.2502	0.7300	0.9154

Table A.8: Model 1: Minimum circularity and maximum rise velocity, with corresponding incidence times and final position of the center of mass for test case 2.

ϵ	c_{min}	$t|_{c=c_{min}}$	$V_{c,max}$	$t|_{V_c=V_{c,max}}$	$y_c(t=3)$
0.040	0.6817	1.9840	0.2483	0.8480	0.8932
0.020	0.6527	2.0000	0.2502	0.7320	0.9058
0.010	0.6614	2.0000	0.2500	0.6980	0.9115
0.005	0.6741	2.0000	0.2503	0.7180	0.9125
ref	0.6901	2.0000	0.2502	0.7300	0.9154

Table A.9: Model 2: Minimum circularity and maximum rise velocity, with corresponding incidence times and final position of the center of mass for test case 2.

ϵ	c_{min}	$t|_{c=c_{min}}$	$V_{c,max}$	$t|_{V_c=V_{c,max}}$	$y_c(t=3)$
0.040	0.6770	2.0000	0.2500	0.7680	0.8880
0.020	0.6684	1.9760	0.2503	0.7960	0.8994
0.010	0.6670	2.0000	0.2488	0.7100	0.9060
0.005	0.6722	2.0000	0.2490	0.7540	0.9098
ref	0.6901	2.0000	0.2502	0.7300	0.9154

Table A.10: Model 3: Minimum circularity and maximum rise velocity, with corresponding incidence times and final position of the center of mass for test case 2.
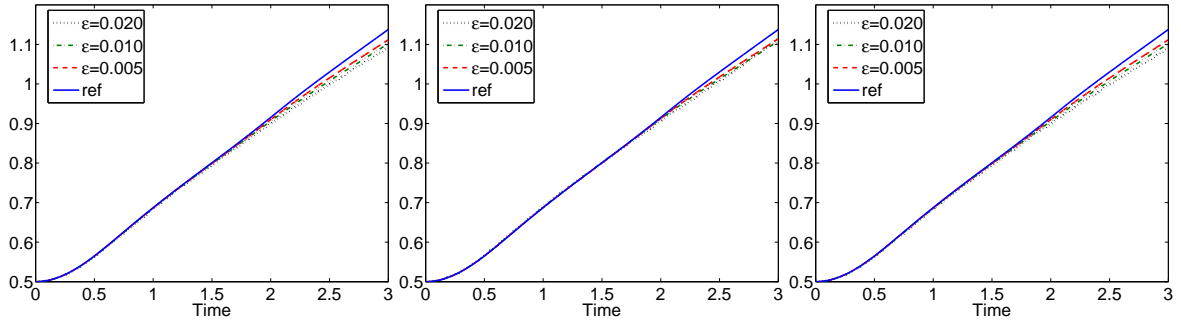

Figure A.5: Center of mass versus time for test case 2 and model 1 - 3 (from left to right). Color online.
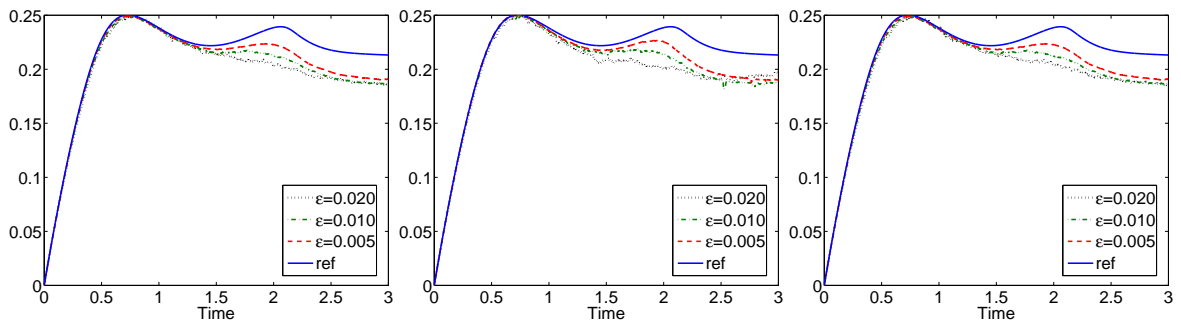

Figure A.6: Rise velocity versus time for test case 2 and model 1 - 3 (from left to right). Color online.

ϵ	$||e||_1$	ROC_1	$||e||_2$	ROC_2	$||e||_\infty$	ROC_∞
Center of mass						
0.040	0.0121		0.0145		0.0288	
0.020	0.0061	0.9803	0.0079	0.8785	0.0170	0.7597
0.010	0.0031	0.9645	0.0043	0.8845	0.0102	0.7370
0.005	0.0020	0.6843	0.0026	0.7107	0.0061	0.7535
Rise velocity						
0.040	0.0555		0.0819		0.1922	
0.020	0.0364	0.6105	0.0529	0.6320	0.1376	0.4818
0.010	0.0252	0.5271	0.0366	0.5324	0.1049	0.3914
0.005	0.0146	0.7913	0.0214	0.7744	0.0623	0.7511
Circularity						
0.040	0.0151		0.0193		0.0374	
0.020	0.0065	1.2135	0.0087	1.1482	0.0241	0.6322
0.010	0.0040	0.6915	0.0069	0.3417	0.0240	0.0075
0.005	0.0024	0.7601	0.0046	0.5802	0.0183	0.3918

Table A.11: Model 1: Relative error norms and convergence orders for test case 2.

ϵ	$||e||_1$	ROC_1	$||e||_2$	ROC_2	$||e||_\infty$	ROC_∞
Center of mass						
0.040	0.0050		0.0083		0.0242	
0.020	0.0028	0.8123	0.0038	1.1038	0.0105	1.2034
0.010	0.0014	1.0722	0.0017	1.2159	0.0042	1.3190
0.005	0.0009	0.6176	0.0012	0.4429	0.0031	0.4484
Rise velocity						
0.040	0.0661		0.0881		0.1886	
0.020	0.0449	0.5581	0.0618	0.5103	0.1512	0.3191
0.010	0.0236	0.9300	0.0347	0.8357	0.0987	0.6151
0.005	0.0132	0.8379	0.0182	0.9310	0.0526	0.9087
Circularity						
0.040	0.0057		0.0071		0.0164	
0.020	0.0121	-1.0891	0.0165	-1.2222	0.0374	-1.1886
0.010	0.0081	0.5745	0.0110	0.5851	0.0290	0.3641
0.005	0.0053	0.6070	0.0068	0.6870	0.0162	0.8407

Table A.12: Model 2: Relative error norms and convergence orders for test case 2.

ϵ	$\|e\|_1$	ROC_1	$\|e\|_2$	ROC_2	$\|e\|_\infty$	ROC_∞
Center of mass						
0.040	0.0130		0.0155		0.0299	
0.020	0.0064	1.0193	0.0082	0.9165	0.0175	0.7732
0.010	0.0033	0.9712	0.0044	0.8916	0.0106	0.7252
0.005	0.0020	0.7031	0.0027	0.7267	0.0061	0.7833
Rise velocity						
0.040	0.0584		0.0838		0.1920	
0.020	0.0374	0.6437	0.0534	0.6505	0.1395	0.4608
0.010	0.0259	0.5292	0.0369	0.5313	0.1055	0.4035
0.005	0.0150	0.7878	0.0216	0.7733	0.0627	0.7502
Circularity						
0.040	0.0151		0.0189		0.0352	
0.020	0.0063	1.2513	0.0085	1.1626	0.0247	0.5076
0.010	0.0039	0.6850	0.0066	0.3515	0.0232	0.0921
0.005	0.0023	0.7611	0.0045	0.5647	0.0179	0.3730

Table A.13: Model 3: Relative error norms and convergence orders for test case 2.

	model 1		model2		model3	
ϵ	$\|e\|_1$	ROC_1	$\|e\|_1$	ROC_1	$\|e\|_1$	ROC_1
Center of mass						
0.040	0.0102		0.0045		0.0110	
0.020	0.0042	1.2777	0.0022	1.0671	0.0044	1.3172
0.010	0.0012	1.8075	0.0010	1.1181	0.0013	1.7958
Rise velocity						
0.040	0.0446		0.0555		0.0464	
0.020	0.0234	0.9335	0.0327	0.7613	0.0237	0.9712
0.010	0.0109	1.1022	0.0112	1.5453	0.0111	1.0893
Circularity						
0.040	0.0151		0.0091		0.0151	
0.020	0.0042	1.8309	0.0069	0.3992	0.0041	1.8742
0.010	0.0017	1.3092	0.0029	1.2728	0.0017	1.2947

Table A.14: Relative error norms and convergence orders for test case 2 assuming the finest grid solution as exact solution.

Acknowledgement

I gratefully acknowledge the funding of this work by the projects DFG Vo-899/6-2, SFB 609 TP C10 and DFG SPP-1506 (Vo-899/II-I). But besides that, there are a bunch of people to whom I would like to express my sincere thanks for having followed and supported me throughout this work. Without them this thesis would simply not have been possible. Among others, I owe my deepest gratitude

- to Prof. Axel Voigt who introduced me in the topics of this thesis and provided an inspiring and liberal environment for my research,

- to Prof. John Lowengrub for teaching me about two-phase flow, for carefully commenting on my work and for always having a good answer to any questions,

- to Thomas Witkowski who did a great job in implementing new features for me in our finite element toolbox AMDiS,

- to Simon Praetorius for inspiring discussions and for helping me to get along with the pitfalls of C++,

- to Rainer Backofen who introduced me into the PFC model,

- to Jade Mackay for proofreading this thesis,

- to our grid master Florian Stenger

- and to my roommate Roland Gärtner.

Furthermore, I thank Julia Aland who motivated me in weary hours and always generously supported my work and all of my travelling. At last, let me give thanks to my parents for material and non-material support of my studies and let us hope that finally, I will be able to convince them that a PhD in mathematics is something you can make a living with.

Selbstständigkeitserklärung

Die am heutigen Tag eingereichte Dissertation zum Thema

Modelling of two-phase flow with surface active particles

wurde am Institut für wissenschaftliches Rechnen der TU Dresden unter Betreuung durch Prof. Dr. rer. nat. Axel Voigt angefertigt. Hiermit versichere ich, dass ich die vorliegende Dissertation ohne unzulässige Hilfe Dritter und ohne Benutzung anderer als der angegebenen Hilfsmittel angefertigt habe; die aus fremden Quellen direkt oder indirekt übernommenen Gedanken sind als solche kenntlich gemacht. Die Arbeit wurde bisher weder im Inland noch im Ausland in gleicher oder ähnlicher Form einer anderen Prüfungsbehörde vorgelegt.

Dresden, den 15. Mai 2012

Dipl. Math. Sebastian Aland